Joint PhD Programme in Molecular Biology (JuMBO)

“ IDENTIFICATION OF NOVEL FACTORS MODULATING CANCER CELL INVASION AND ANGIOGENESIS ”

PhD student
Ambra Cappelletto

International Centre for Genetic Engineering & Biotechnology
(ICGEB)
Trieste, Italy

Director of studies: Prof. Serena Zacchigna

TABLE OF CONTENTS

LIST OF FIGURES **1**

LIST OF TABLES **2**

ABSTRACT **3**

ACKNOWLEDGEMENTS **4**

1. INTRODUCTION **5**

1.1 The need for novel therapies for cancer 5

1.1.1 The clinical impact of cancer and metastasis 5

1.1.2 Incidence and mortality 6

1.1.3 Preferential sites of metastasis 7

1.2 Mechanisms of cancer invasion and dissemination 10

1.2.1 Local invasion and ECM degradation 10

1.2.2 Epithelial to Mesenchymal Transition 11

1.2.3 Intravasation and survival in the circulation 11

1.2.4 Colonization at a distant site 12

1.3 Establishment of the metastatic niche 13

1.3.1 The role of cancer-associated fibroblasts 14

1.3.2 The ECM evolves to sustain the tumor growth 15

1.3.3 The importance of angiogenesis for normal and tumor tissues 18

1.4 Why is it so hard to destroy metastatic foci? 24

1.5 Innovative therapies for cancer 25

1.5.1 Biotherapeutics 25

1.5.2 Monoclonal Antibodies for cancer treatment 26

1.5.3 Antibody-drug conjugates 29

1.5.4 Gene therapy and AAV vectors 30

1.5.5 Current gene therapy applications and clinical trials 30

1.5.6 *In vivo* Functional Selection (FunSel) for discovery of anti-invasive factors 32

2. MATERIAL AND METHODS **34**

2.1 Secretome library and AAV production 34

2.2 Screening of the library *in vivo* 34

2.3 Cell culture 35

2.3.1 Primary cell isolation 35

2.3.2 Transfection of HEK-293T and production of enriched supernatant 36

2.3.3 Migration assays 36

2.3.4 Tube formation assay 37
2.3.5 Production of the extracellular matrix 37
2.3.6 Activation of α-SMA-RFP/COLL-EGFP fibroblasts 38
2.3.7 Proliferation assay 38
2.4 Animal experimentation 38
2.4.1 Evaluation of angiogenesis *in vivo* 39
2.4.2 Skeletal muscle tumors 39
2.4.3 Lung metastasis 39
2.5 Molecular biology 40
2.5.1 Recombinant proteins 40
2.5.2 Western blot 40
2.5.3 Immunostaining 41
2.5.4 Immunohistochemistry 42
2.5.5 Receptor tyrosine kinase (RTK) assay 42
2.6 Rheology 42
2.7 Image acquisition and analysis 43
2.8 Statistical analysis 43
3. RESULTS 44
3.1 Set up of FunSel for the selection of anti-invasive factors 44
3.1.1 Choosing the appropriate cancer cell type to exert an efficient selective pressure 44
3.1.2 A powerful selection requires a specific timing 44
3.2 FunSel provided a selection of secreted factors 48
3.2.1 Validation of the 10 top hits inhibiting cell migration 53
3.2.2 EMID2 was the best factor inhibiting cancer cell growth *in vivo* 55
3.3 Direct effect of the recombinant EMID2 on cell migration 57
3.3.1 Recombinant EMID2 blocked tumor cell migration *in vitro* 57
3.4 EMID2 modulates angiogenesis 60
3.4.1 Tumors were less vascularized in presence of EMID2 60
3.4.2 EMID2 inhibited angiogenesis *in vivo* 61
3.4.3 EMID2 inhibited angiogenesis *in vitro* 63
3.5 EMID2 affects the tumor matrix 67
3.5.1 The tumor contained less α-SMA when EMID2 was expressed 67
3.5.2 Myofibroblast activation was inhibited by EMID2 69
3.5.3 EMID2 modified the structure and composition of the ECM *in vivo* and *in vitro* 73
3.5.4 EMID2 modified the strain/stiffness properties of the matrix 74

3.6 EMID2 inhibits TGFβ maturation 77
3.6.1 Inhibition of TGFβ maturation by EMID2 contributed to its anti-angiogenic function 77
3.7 EMID2 expression in the lung protected from metastatic invasion 80
3.8 The "lost" factors can support the tumor growth and invasiveness 83
3.8.1 BD33 enhanced the migration of different cell types *in vitro* 83
3.8.2 BD33 stimulated tumor growth and proliferation both *in vitro* and *in vivo* .. 86
3.8.3 BD33 activated the EGFR pathway in HUVECs 87
3.8.4 BD33 promoted angiogenesis 89
4. DISCUSSION 92
4.1.1 FunSel successfully selected secreted factors with anti-invasive and anti-angiogenic properties 92
4.1.2 EMID2 is a novel potential biotherapeutic for cancer therapy 94
4.1.3 The double power of FunSel: identifying novel proteins with pro-tumor function 100
5. REFERENCES 102
WEBSITE REFERENCES 115
6. APPENDIX 116

LIST OF FIGURES

Figure 1. Incidence of most common cancers in United States, from 1975 to 2015.

Figure 2. Metastatic spread of the most common tumors.

Figure 3. The ECM is remodelled during cancer initiation and invasion.

Figure 4. Tumor vessels display abnormal properties.

Figure 5. Tumor vessel normalization is a novel strategy for cancer treatment.

Figure 6. FunSel strategy.

Figure 7. Optimization of the FunSel strategy for the selection of anti-invasive factors.

Figure 8. FunSel for the selection of anti-invasive factors.

Figure 9. Screened single pools.

Figure 10. The final ranking of the secreted factors after FunSel.

Figure 11. FunSel identified anti-invasive secreted factors.

Figure 12. EMID2 reduced tumor growth *in vivo*.

Figure 13. Structure of EMID2 protein.

Figure 14. Recombinant EMID2 inhibited cell migration in the wound healing assay.

Figure 15. Tumors overexpressing EMID2 were less vascularized.

Figure 16. EMID2 inhibited angiogenesis *in vivo*.

Figure 17. EMID2 inhibited tube formation of HUVEC *in vitro*.

Figure 18. EMID2 inhibited tube formation by primary endothelial cells.

Figure 19. α-SMA was less abundant in the tumors when EMID2 was expressed.

Figure 20. EMID2 expression in the tumor reduced the presence of CAFs.

Figure 21. EMID2 reduced the activation of myofibroblast *in vitro*.

Figure 22. EMID2 modified matrix composition and structure.

Figure 23. TGFβ was inhibited by EMID2 and rescued its anti-angiogenic effect *in vitro*.

Figure 24. Expression of EMID2 in the lung protected from colonization by cancer cells.

Figure 25. BD33 increased cell migration.

Figure 26. BD33 stimulated the directional movement and pro-migratory phenotype of fibroblasts.

Figure 27. BD33 stimulated the proliferation of different cell types and sustained tumor growth *in vivo*.

Figure 28. BD33 had a pro-angiogenic effect *in vitro* and in tumors *in vivo*.

LIST OF TABLES

Table 1. Summary of the monoclonal antibodies approved by the FDA for the treatment of solid tumors.

Table 2. Summary of the clinical trials based on gene therapy for monogenic diseases in phase III/IV.

Table 3. Primers for the two-step PCR amplification of barcodes.

Table 4. Recombinant proteins.

Table 5. Antibodies used for immunostaining.

Table 6. Relative enrichment of factors in the pilot pool of AAV9 at 2 or 10 days after LLC cell injection.

ABSTRACT

Metastasis is the main cause of cancer related death, largely dependent on the formation of new blood vessels (angiogenesis), that sustains the growth and the invasiveness of cancer cells. Existing therapies targeting either tumor-associated angiogenesis or metastatic dissemination are limited and poorly effective. Here we exploit an innovative strategy, named FunSel, for the *in vivo* functional selection of secreted factors able to contrast cancer cell invasiveness. The top ten identified factors were first tested *in vitro* for their capacity to block cell migration, and the most potent ones were further validated *in vivo* for their capacity to inhibit cancer growth. The AAV-mediated overexpression of a top hit, EMI Domain Containing 2 (EMID2), induced a 30% reduction of the tumor volume, paralleled by a marked inhibition of tumor angiogenesis. We showed that EMID2 modified the tumor microenvironment by inhibiting the activation of cancer-associated fibroblasts and altering the composition and mechanical properties of the extracellular matrix. Finally, its expression in lungs was able to prevent the formation of metastasis.

The same strategy allowed us to identify factors promoting the invasion of cancer cells. Among them, we identified BD33 as a novel factor that promotes cancer cell growth, migration and angiogenesis both *in vitro* and *in vivo*.

In conclusion, the FunSel approach led to the identification of a novel series of secreted factors as the most potent ones to modulate the growth and invasiveness of cancer cells *in vivo*, paving the way for the development of innovative therapeutic opportunities to control tumor progression and modulate angiogenesis.

ACKNOWLEDGEMENTS

I am profoundly grateful to my supervisor Serena Zacchigna for supporting this research work in her lab, and for setting an example in both science and life.

Heartfelt thanks go to the “old” and “newer” Cardiovascular Biology group members for their support, patience and, definitely, for representing my second family.

My project would have been impossible without the aid and support of all the components of the Molecular Medicine group, in particular Francesca Bortolotti and Giulia Ruozi. Thanks for turning all my doubts into self-awareness.

I also would like to thank Eduard Ayuso and Massimo Santoro for their supervision on my PhD thesis.

Last but not least, thanks to my family and my friends. Using scientific-like words, no statistics can represent the contribution of all of them to my life.

1. INTRODUCTION

1.1 The need for novel therapies for cancer

1.1.1 The clinical impact of cancer and metastasis

Cancer is the leading cause of disability and death worldwide (*https://www.who.int/cancer/en/*). The so-called 'omic' technologies applied to cancer tissue specimens and body fluids have revealed specific molecular signatures of cancer (Saintigny et al., 2011), significantly contributing to our understanding of the molecular mechanisms responsible for malignant transformation and cancer progression and thus to the development of targeted therapies. In parallel, prevention campaigns and progresses in both detection and treatment methods have significantly reduced the incidence and mortality of almost all tumor types. A paradigmatic example is the increased survival (from 31% to 63%) registered for patients affected by chronic myeloid leukemia over the last 20 years, thanks to the use of BCR-ABL tyrosine kinase inhibitors, such as the monoclonal antibody imatinib (Ferdinand et al., 2012).

Metastatic events are responsible for about 90% of cancer deaths (Chaffer and Weinberg, 2011). The term metastasis describes the spread of cancer cells from the primary tumor to surrounding tissues and distant organs. Tumor cells detach from primary tumors to disseminate through the blood and form new metastatic foci (Aya-Bonilla et al., 2017). Their presence in the blood renders them a potential biomarker for the early diagnosis and monitoring of primary tumor biology, clinical status and response to therapy (Lv et al., 2016). However, the isolation and detection of circulating tumor cells (CTCs) still remains a technical challenge, due to their rarity in the blood (i.e. 1-10 cells per 8 mL of blood in melanoma patients), high phenotypic heterogeneity and the lack of accurate markers for their identification (Lv et al., 2016). Several methods for CTC detection have been proposed so far, and the Food and Drug Administration (FDA) in the United States has recently approved a platform called CellSearch® (Janssen Diagnostics LLC) for CTC quantification (Khoo et al., 2014). Recently, spiral microfluidic devices have been developed to recover CTCs at high efficiency in breast, lung and melanoma cancer and could be useful in preventing metastasis (Aya-Bonilla et al., 2017; Warkiani et al., 2014). In parallel, a deeper understanding of the molecular mechanisms enabling metastasis will aid the development of cancer treatments.

1.1.2 Incidence and mortality

Cancer has a strong impact on society across the world (Chaffer and Weinberg, 2011). The increasing incidence of cancer is linked to several factors, including ageing of the population and increase in risk factors following economic and social development. In 2018, 18,1 million new cases of cancer were diagnosed worldwide causing 9.6 million deaths, and meaning that cancer is experienced by 1 in 5 men and 1 in 6 women during their lifetime (World Health Organization, *https://www.who.int*).

In both Europe and the Americas, the incidence of cancer is higher than its mortality (23.4% and 21% of cancer cases and 20.3% and 14.4% of cancer deaths, respectively). In contrast, Asia and Africa experience a higher proportion of death rates (57.3% and 7.3%, respectively) compared to the proportion of cancer incidence (48.4% and 5.8%, respectively), reflecting the higher occurrence of more aggressive cancer types in the latter continents and a more limited access to early diagnosis and treatment (World Health Organization, *https://www.who.int*).

It is estimated that nearly 1,8 million new cases of cancer will be diagnosed in the United States alone in 2019, as well as over 600,000 cancer deaths (Siegel et al., 2019). The most common cancers expected to be diagnosed in 2019 are lung, bronchus, colorectal, prostate and breast cancers. In particular, breast cancer accounts for 30% of all new cases in women.

The modifications in life style and environment that occurred in the last century have dramatically increased the occurrence of cancer incidence and prevalence, particularly for some tumor types. For instance, melanoma, liver, thyroid, uterus and pancreas cancers are becoming more and more frequent as a consequence of life habits that are easily identifiable as major risk factors, including excessive alcohol consumption, cigarette smoking and obesity. The incidence of colorectal cancer also increased by 1.8% per year from 1992 to 2012 in patients younger than 50 years, who are not subjected to prevention screening, and it has continued to increase since then, despite improved diagnostic procedures (i.e. colonoscopy) (Janitz et al., 2016). In contrast, the incidence of lung cancer massively decreased in the mid-1980s in men and twenty years later in women as a result of reduction of smoking (Siegel et al., 2019).

The overall incidence of cancer has been frightfully increasing by 0.7% per year also in children and adolescents since 1975, although death rates continue to decline (Siegel et al., 2019). Over 11,000 new cases of cancer in children are estimated to be diagnosed in 2019, with leukemia accounting for 28% of cases. Adolescents, in contrast, are mostly diagnosed with thyroid carcinoma and skin melanoma.

The incidence and outcomes of cancer are considerably variable between races and ethnicities, partially due to genetic variability and predisposition, but largely due to inequalities in access to health systems and exposure to risk factors. Although the racial gap in mortality is narrowing, socioeconomic differences are widening, resulting in notable consequences at least for the most

preventable cancers. From 2012 to 2016, the poorest American countries displayed a 2-fold increase in mortality for cervical cancer and 40% higher mortality for liver and lung cancers in male, compared to the richest areas (Siegel et al., 2019). Moreover, in the United States, cancer mortality in 2016 showed a black-white disparity of 16% (183.6 vs 160.7 per 100,000 population), which was, however, decreased from the 33% registered in 1993 (Siegel et al., 2019).

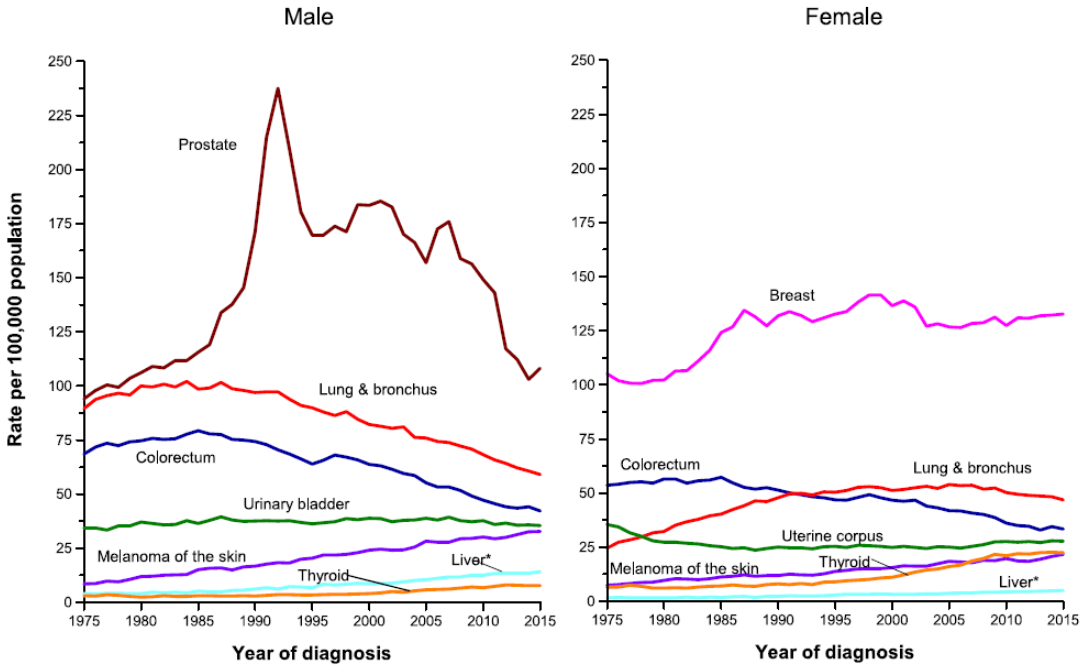

Figure 1. Incidence of most common cancers in United States, from 1975 to 2015*. Prostate and breast cancers are the most common types of cancer diagnosed in men and women, respectively. (Siegel et al., 2019)*

1.1.3 Preferential sites of metastasis

Over the last century, various studies have investigated whether the process of tumor invasion was merely a passive movement of cancer cells into the vascular tree rather a fine-tuned mechanism of invasion guided by a specific crosstalk between cancer cells and the vasculature to colonize specific tissues. The vascular pattern and anatomy of each organ certainly influence the metastatic spread of cancer, but this does not completely explain the organ-specific invasion of certain cancer types. The major hypothesis is that individual cancers have a specific tropism for certain tissues, where they tend to metastasize. Paget was the first to analyse 735 cases of breast cancer and to conclude that the blood flow could not be the only explanation for the preferable metastatic tropism to certain organs, such as the liver (Paget, 1889). A century after this first evidence, Findler confirmed the “seed and soil” theory, conclusively demonstrating

that even though the cancer cells can reach all organs through the vasculature, metastases preferentially occur in selected organs (Fidler and Kripke, 1977).

A few organs besides lymph nodes, namely liver, lung, brain and bone, represent preferential targets for metastatic cells, also depending on the nature and the tissue of origin of the primary cancer (Figure 2). Melanoma and breast cancers usually metastasize to the skin, ovarian metastases generally occur in breast, and the spleen is often metastasized by melanoma (Budczies et al., 2015). Bone metastases are a common consequence of 60-85% of patients with metastatic breast and prostate cancer. One of the reasons underlying the high frequency of metastasis in both liver and bone is the presence in these organs of fenestrated and highly permeable capillaries, called sinusoids. In addition, osteoblasts within the bone matrix are known to secrete chemoattracting factors for cancer cells (e.g. CXCL12, RANKL, BMPs). In the osteolytic lesions, osteoclasts are activated and produce collagenases and other proteases that degrade the extracellular matrix (ECM) and demineralize the bone matrix (Weilbaecher et al., 2011). Brain metastases have a particularly poor prognosis, with high morbidity and mortality and a median survival of patients in the order of only some months (Eichler et al., 2011). In this case, the cancer cells usually derive from lung adenocarcinoma, breast cancer or melanoma, and reach the brain parenchyma and the leptomeninges through the micro-capillary walls constituting the blood-brain barrier. Some of the molecules that mediate metastasis into the brain have been identified, including the sialyltransferase ST6GalNac5, cyclooxygenase 2 (COX2), heparin-binding EGF-like growth factor (HB-EGF), the matrix metalloproteinase 2 (MMP2), the microRNA miR-105, and cathepsin S (Bos et al., 2009; Zhou et al., 2014).

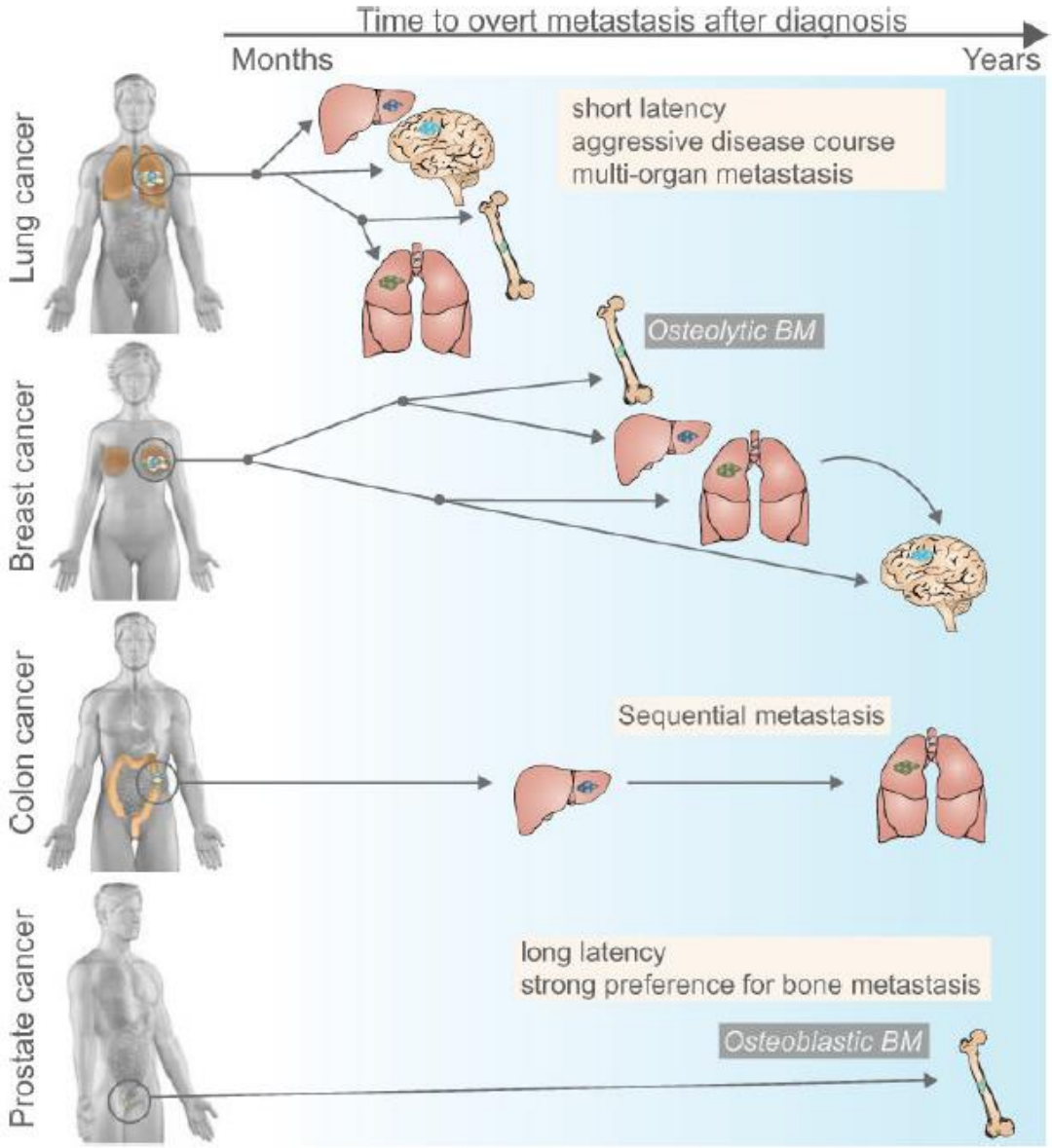

Figure 2. Metastatic spread of the most common tumors. *The metastatic process has specific features in different tumors, including different lengths of the latency period and a variety of specifically targeted organs. Reprinted from (Obenauf and Massague, 2015).*

1.2 Mechanisms of cancer invasion and dissemination

1.2.1 Local invasion and ECM degradation

To start the metastatic process, a subset of cancer cells belonging to a primary tumor invades the surrounding tumor-associated stroma and the adjacent parenchyma of the normal tissue. The first barrier to break is the basement membrane, which is a specialized ECM structure that divides the epithelial cells from the stromal compartment and plays a fundamental role in epithelial tissue organization and signal transduction. In the mammary gland, myoepithelial cells are the major producers of the basement membrane, the integrity of which inhibits cancer cell invasion, as shown by the fact that the co-injection of myoepithelial cells decreases the invasiveness of breast carcinoma xenografts (Hu et al., 2008).

Matrix degradation is central to tumor development and several ECM remodelling enzymes are often deregulated in cancer. Heparanases, sulfatases and, most notably, metalloproteinases (MMPs) are overexpressed in most tumors (Kessenbrock et al., 2010). Various MMPs (especially MMP-2 and MMP-9) are best known for their ability to degrade components of the ECM, although they can also cleave other proteinases, proteinase inhibitors, growth factors, chemotactic molecules, growth factor binding proteins, cell surface receptors and cell-cell adhesion molecules (Sternlicht and Werb, 2001). MMPs control the release and bioavailability of transforming growth factor β (TGFβ) and vascular endothelial growth factor (VEGF), which are fundamental to foster tumor growth and to create the new tumor vasculature (Kessenbrock et al., 2010).

The major role of MMP activity in tumor development has set the basis for the development of various strategies to block these enzymes for cancer therapy. Their function is mainly controlled at the level of transcription and activity. At the transcriptional level, MMP inhibition can be achieved by interfering with transcription factors, such as NF-kB or AP-1 (Folgueras et al., 2004). They are secreted as inactive zymogens and inhibited by natural tissue inhibitors of MMPs, called TIMPs (Cui et al., 2017). In addition, a few synthetic inhibitors (MMPI) have been generated and progressed to clinical trials for different cancers, including the peptidomimetic MMPI Batimastat (BB-94), which has been recently replaced by Marimastat (BB-2516) to overcome the problem of low water solubility. However, Marimastat displayed negative side effects, such as musculoskeletal pain (Gialeli et al., 2011; Yan et al., 2009). Prinomastat (AG-3340), Tanomastat (BAY12–9566), and MMI 270 B (CGS 27023 A) are newer MMPIs, designed according to the 3D conformation of the MMP active site, and showing higher specificity. Metastat (COL-3, CMT-3) is a chemically modified tetracyclin, which shows poor systemic toxicity and is currently in phase II for Kaposi's sarcoma and brain tumors. Belonging to the same category, Doxycycline is the only MMPI approved by the FDA for the

prevention of periodontitis (Sapadin and Fleischmajer, 2006). Finally, bisphosphonates have been shown to influence the expression of various MMPs and TIMPs in breast cancer (Coxon et al., 2006).

1.2.2 Epithelial to Mesenchymal Transition

Tumor cells can adopt various strategies of invasion, acting as cohesive multi-cellular units ("collective invasion") or independently as single cells through a process called "mesenchymal invasion" or "amoeboid invasion" (Friedl and Wolf, 2003).

For transformed epithelial cells, the main intrinsic obstacle to cell invasion is the E-cadherin-mediated intercellular junctions that keep them tight together. Cancer cells of epithelial origin often overcome this limitation undergoing a deep reprogramming called epithelial to mesenchymal transition (EMT), a phenomenon naturally occurring during embryonic morphogenesis (Kalluri and Weinberg, 2009).

The expression of specific transcription factors (EMT-TFs) such as Slug, Snail, Zeb and Twist, together with a range of miRNAs and post-transcriptional regulators modify the adhesion molecules normally expressed by the cell allowing it to adopt new properties of migration and invasiveness. As an example, a loop of negative feedback among the members of the miR-200 family and ZEB1 and ZEB2 EMT-TFs, regulates the expression of either epithelial or mesenchymal markers (Thiery, 2009). Cancer cells cannot be considered to be either epithelial or mesenchymal origin, but rather they exist in a spectrum of intermediary states, often undergoing partial EMT re-programming (Nieto et al., 2016).

Once the basement membrane is lost, cancer cells can enter into the stroma that becomes "reactive", acquiring an inflammatory phenotype, where they come in contact with a series of cell types, including fibroblasts, myofibroblasts, endothelial cells, adipocytes, macrophages and immune cells (Joyce and Pollard, 2009). The aggressiveness of carcinoma cells is enhanced by the stromal cells through various types of heterotypic signalling. For example, in breast cancer, adipocytes secrete interleukin-6 (IL-6) and IL-4, which in turn stimulate cathepsin proteolytic activity and therefore breast cancer invasiveness (Dirat et al., 2011; Gocheva et al., 2010).

1.2.3 Intravasation and survival in the circulation

Dissemination of cancer cells through the bloodstream represents the main mechanism of metastasis. During tumor growth, cancer cells acquire the capacity to enter into blood vessel (intravasation), overcoming the barrier created by pericytes and endothelial cells. Among the most known players involved in this process, TGFβ has been demonstrated to stimulate the penetration of mammary carcinoma cells into the microvascular wall (Giampieri et al., 2009).

Other molecules, such as the transcriptional modulator amino-terminal enhancer of split (AES), impair trans-endothelial invasion through the Notch pathway, resulting in the inhibition of intravasation by colon carcinoma cells (Sonoshita et al., 2011).

Tumor cells secrete VEGF to induce the formation of a new vascular network inside the tumor mass, in a process called neoangiogenesis. The new vasculature generated by the tumor presents specific characteristics typical of immature vessels, which are tortuous, fenestrated, prone to leakiness and in a state of continuous reconfiguration (Carmeliet and Jain, 2011b). It has been reported that the collective expression of the epidermal growth factor receptor (EGFR), COX2, MMP1 and MMP2 by breast cancer cells is able to stimulate metastasis by promoting the formation of leaky blood vessels (Gupta et al., 2007).

Once cancer cells enter the circulation, they must survive a series of stresses in order to reach and colonize distant organs. First, they must escape anoikis, the programmed cell death induced upon cell detachment from the ECM. Anoikis starts with the activation of caspases and culminates with the activation of endonucleases, DNA fragmentation and cell death, acting as a fundamental defence mechanism of the organism to prevent the re-adhesion of detached cells to new sites at incorrect locations (Chiarugi and Giannoni, 2008). Anoikis resistance of cancer cells is associated with the altered expression of proteoglycans, such as syndecan 4, and the inhibition of cell death pathways, together with the activation of pro-survival signalling pathways, such as the Ras/ERK, PI3K/Akt, NF-kB and Rho-GTPase pathways (de Sousa Mesquita et al., 2017).

Secondly, cancer cells which successfully enter blood vessels are stressed by hemodynamic shear forces and can be killed by circulating immune cells (specifically natural killer cells). Cancer cells often evolve mechanisms to evade these threats, for instance by interacting with blood platelets and hiding themselves inside large emboli, a process mediated by the expression of Tissue Factor (TF) and/or L- and P-selectins (Joyce and Pollard, 2009).

1.2.4 Colonization at a distant site

As mentioned above, the Paget's "seed and soil" theory posed the basis to investigate an active role of cancer cells in the colonization of the second tumor site of growth. According to this theory, primary tumors release molecular signals to upregulate fibronectin by resident fibroblasts, which in turn express the lysyl oxidase (LOX) enzyme, responsible for major ECM remodelling events and promoting metastasis (Xiao and Ge, 2012). In response to released soluble factors, such as inflammatory chemokines, both haematopoietic progenitor cells and macrophages are mobilized from the bone marrow to the pre-metastatic niche. The recruitment of immune cells leads to an immunosuppressive, anti-inflammatory environment, which prevents the detection and killing of the tumor by the immune system (Yang and Moses, 2008).

Hiratsuka et al. analysed a pre-metastatic lung in mice injected in the flank with syngenic Lewis Lung Carcinoma (LLC) or B16-F10 melanoma cells, known to preferentially metastasize to the lung, and reported that TGFβ, VEGF-A and TNFα from the primary tumor induced the expression of inflammatory proteins in the lung parenchyma but not in the other organs (Hiratsuka et al., 2006).

Activation of MMPs is also observed in the niche. In particular, MMP9 expression is up-regulated in endothelial cells and myeloid cells in the pre-metastatic lung, facilitating tumor cell invasion (Hiratsuka et al., 2002).

Specific genes that control the movement of metastatic cells towards specific organs have been identified for breast cancer. The pattern of gene expression is different when cancer cells from breast cancer metastasize to the bone, the lung or the brain (Bos et al., 2009; Kang et al., 2003; Minn et al., 2005). For example, osteolytic bone metastasis has been demonstrated to be promoted by the cytokine IL-11 produced by breast cancer cells or facilitated by the Notch ligand Jagged 1 that drives the secretion of IL-6, and in this way increases the deposition of growth factors normally sequestered in the bone matrix (McCoy et al., 2013; Sethi et al., 2011).

The fact that many changes occur prior to the arrival of tumor cells suggests that the induction of a pre-metastatic niche within target organs is vital and a permissive step for metastasis. Therefore, targeting the metastatic niche stands as a promising strategy to contrast cancer growth.

1.3 Establishment of the metastatic niche

The microenvironment of a developing tumor mainly consists of proliferating cancer cells housed in a permissive stroma irrigated by blood and lymphatic vessels, and containing infiltrating inflammatory cells and a variety of cell types that support tumor growth (Walker et al., 2018).

Increasing attention has been focused on the tumor microenvironment over the last year, as numerous studies have proven its fundamental role in tumor development and progression. A healthy tissue microenvironment has been shown to be protective against tumorigenesis and invasion. By contrast, the microenvironment modified by cancer cells becomes dysfunctional and supports the progression of the malignancy (Dupont et al., 2011; Riching et al., 2014). Understanding the interplay between the multiple components of the tumor microenvironment and interfering with more than one mechanisms supporting tumor aggressiveness is expected to lead to novel and efficient therapeutic results.

1.3.1 The role of cancer-associated fibroblasts

Fibroblasts which are activated by cancer cells are known as cancer-associated fibroblasts (CAFs) or myofibroblasts. In tumors, fibroblasts can be re-programmed into pro-tumorigenic myofibroblasts by multiple mechanisms, including local hypoxia and oxidative stress, and the activation of TGFβ, PDGF and IL-6 signaling pathways (Giannoni et al., 2011; Pietras et al., 2008; Quante et al., 2011). A similar activation of fibroblast also occurs during any tissue lesion by either growth factors and direct cell-cell communication. When myoblasts remain perpetually activated, they may cooperate with other molecular pathways to boost neoplasm initiation (Chen and Song, 2019).

CAFs are very abundant in the tumor microenvironment and, although they are a heterogeneous population, they are generally recognized as spindle-shaped cells that express Alpha Smooth Muscle Actin (α-SMA) and vimentin (Su et al., 2018). They are highly contractile and motile and display increased secretion of ECM components, particularly collagen I, hyaluronan and fibronectin (Chen and Song, 2019). Indeed, the most distinctive feature of CAFs is their role in ECM synthesis and remodelling during desmoplasia, which is a dynamic stromal alteration leading to mechanical stiffening of the tissues and fibrosis. This increased tissue tension may lead to cancer progression and it is associated with poor outcomes in patients affected by breast, colorectal and pancreatic cancers (Calvo et al., 2013; Laklai et al., 2016; Tsujino et al., 2007). Simultaneously, CAFs produce ECM-degrading proteases, such as MMPs, creating a continuous loop of ECM secretion and remodelling that actively contribute to sustain tumor progression, angiogenesis and invasion (Chen and Song, 2019).

Targeting CAFs for cancer therapy

CAFs represent promising therapeutic targets for cancer therapy. Depletion of CAFs has been attempted by targeting either Fibroblast Activation Protein Alpha (FAP)-positive myofibroblasts or α-SMA$^+$ myofibroblasts. FAP is a serine protease that modulates the differentiation and proliferation of CAFs and a cell surface marker that specifically recognizes myofibroblasts in most of human cancers (Huber et al., 2003). Further, both FAP-targeting monoclonal antibodies and immunotoxins have been developed (e.g. FAP5-DM1, αFAP-PE38, F19 or sibrotuzumab) (Fang et al., 2016; Ostermann et al., 2008; Scott et al., 2003). The importance of α-SMA was shown in experiments utilizing double transgenic mice obtained by crossing double transgenic mice obtained by crossing mice that develop pancreatic ductal adenocarcinoma with α-SMA-thymidine kinase (TK) transgenic mice. Importantly, the depletion of α-SMA$^+$ CAFs resulted in suppressed tumor angiogenesis but led to increased infiltration that worsened tumor progression (Ozdemir et al., 2014). Although both FAP and α-

SMA are useful molecular targets, neither is uniquely expressed by fibroblasts, which potently affects the precision of CAF-targeting therapies.

Another strategy targets crucial signals and effectors to block the activation or function of CAFs, such as growth factors and chemokine pathways. Furthermore, some molecules have been developed to normalize CAFs into inactive cells, such as all-trans retinoic acid (ATRA) or calcipotriol (Froeling et al., 2011; Sherman et al., 2014)

1.3.2 The ECM evolves to sustain the tumor growth

The ECM is defined as the non-cellular milieu of the tissue that provides structural and biochemical support to the cells. It is normally composed by water, minerals, proteoglycans and fibrous proteins, and shows a composition that is unique for each organ, assigning specific properties including elasticity and resistance to the strength (Walker et al., 2018). The ECM is a very dynamic structure, constantly undergoing remodelling and protein degradation. While for many years the ECM was considered an inert scaffold for cell support, its role in regulating cell proliferation, migration and apoptosis has progressively become clear. Indeed, in addition to providing anchorage and structural integrity, the ECM mediates the release of growth factors and the transmission of mechanical signals. Excessive ECM deposition and rigidity affects the mechanotransduction, that is the process of conversion of mechanical stimuli into intracellular chemical signals (Uhler and Shivashankar, 2017).

Collagen is the primary component of the ECM. Among the 28 unique subtypes discovered so far, collagen I is the most abundant and is essential in organ development and wound repair (Mouw et al., 2014). Fibrillary collagens are produced as precursors and processed during or after secretion in the ECM. Larger collagen fibers are established by the action of small leucine rich proteoglycans (SLRPs, i.e. decorin and biglycan), containing collagen-binding motifs and determining fiber structure and morphology (Mouw et al., 2014). Fibril-associated collagens with interrupted helices (FACIT) are another subfamily of collagen that are associated with the collagen microfibrils (Ricard-Blum, 2011). They bind to SLRPs and proteoglycans to create high-order structure. Further stabilization of the network is mediated by the LOX enzyme, providing collagen with a remarkable tensile strength (Levental et al., 2009). In the basal lamina, together with ECM proteins such as laminin, perlecan and nidogen, there are also network forming collagens, including type IV, VIII and X (Mouw et al., 2014).

In addition to collagen, other important molecules compose the ECM. Fibronectin is organized in a fibrillary network in the ECM and it interacts with the other components of the ECM to connect cells to the matrix (Laklai et al., 2016).

Proteoglycans can be found in the membrane (i.e. syndecans), in the pericellular space (i.e. perlecan) or in the extracellular space (i.e. hyalectans and SLRPs). They are covalently bonded

to negatively-charged glycosaminoglycans (GAGs), that attract water and cations and provide lubrification and space-filling properties (Walker et al., 2018). Finally, laminins are glycoproteins organized in trimers of various size (400-800 kDa). Their main function is to bridge the interaction between the ECM and the cells through their binding with integrins, thus strongly affecting cell phenotype, adhesion, migration, differentiation and survival to apoptosis (Walker et al., 2018).

The abnormal composition, structure and remodelling of the ECM play a critical role in cancer. Activated fibroblasts secrete increased amounts of ECM, mainly composed of fibronectin and collagen I, that augments the stiffness of the tissue and alters mechanotransduction (Walker et al., 2018). A deep re-organization of the ECM follows the elevated secretion of collagens and collagen-remodelling enzymes that occurs in the tumor microenvironment. Indeed, collagen fibrils become linearized and compacted to thick collagen bundles, that serve as highways for cancer cell migration (Riching et al., 2014). The density and the extent of crosslinking of collagen fibers have been suggested to determine the rigidity of tumors (Acerbi et al., 2015). However, the exact mechanism that links the abnormal ECM deposition with an increased stiffness in cancer progression is not well described. Some studies associated the up-regulation of LOX with increased elastin and collagen cross-linking. This causes matrix stiffness and the activation of integrins and Rho, that promote cell motility (Levental et al., 2009; Xiao and Ge, 2012). Increased collagen crosslinking and parallelization have been identified in human colorectal carcinomas, where an increased overall collagen content and fibers organized in parallel orientation were associated with tumor progression and cancer cell invasion (Acerbi et al., 2015).

Targeting the ECM for cancer therapy

Losartan is an FDA approved angiotensin II receptor agonist that inhibits the TGFβ pathway and reduces the secretion of collagen I. This results in a consequent decreased desmoplasia and the improved delivery of chemotherapeutic agents to the tumor (Diop-Frimpong et al., 2011). The heparanase inhibitor Ronespartat showed promising results for the treatment of multiple myeloma, when used in combination with other agents targeting the tumor microenviroment (Cassinelli et al., 2013).

Despite the theoretical advantages of stromal depletion to ameliorate cancer drug delivery, this approach may increase the risk of depleting vital components of the ECM, thus further exacerbating cancer progression (Ozdemir et al., 2014; Sherman et al., 2014). Therefore, the preferential strategy would be combining targeted therapeutics with agents able to reprogram the pro-tumor microenvironment into a tumor-suppressive milieu (Roma-Rodrigues et al., 2019).

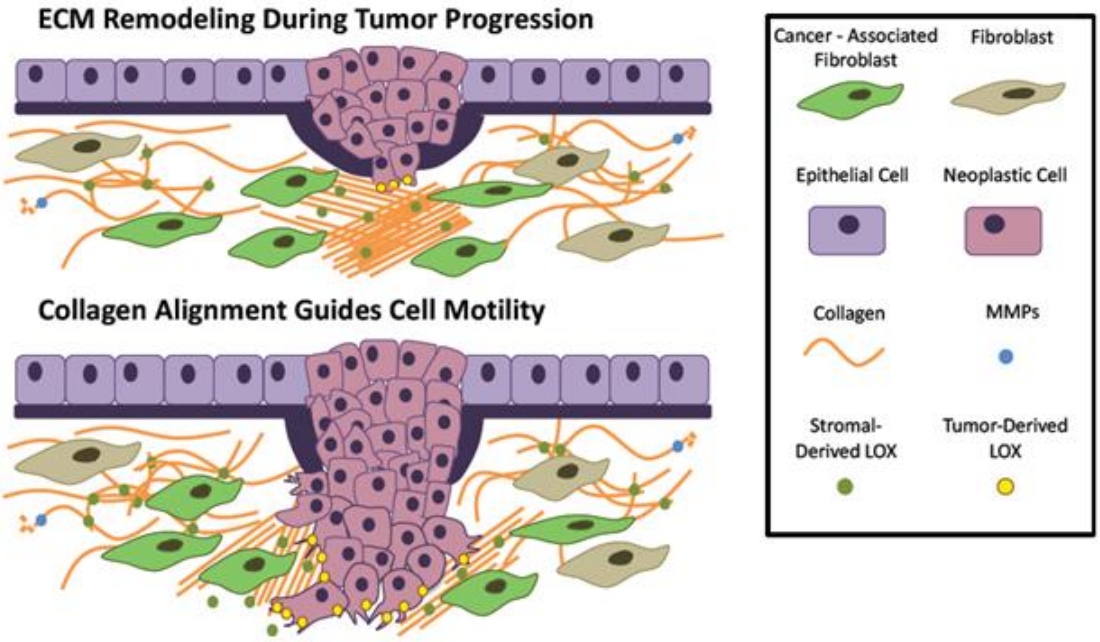

Figure 3. The ECM is remodelled during cancer initiation and invasion. *Cancer cells push the basement membrane to invade the tissue stroma. Adjacent-CAFs secrete ECM proteins and growth factors to sustain tumor cell invasion. Collagen fibers are aligned by LOX enzymes and guide neoplastic cell migration. Adapted from (Lu et al., 2011).*

1.3.3 The importance of angiogenesis for normal and tumor tissues

Angiogenesis

In the mammalian embryo, vasculogenesis occurs when endothelial cells differentiated from angioblasts and assemble to form a vascular tree. Then, distinct signals specify the arterial or venous fate, such as the Ephrin-B2/EPHB4 axis. During vessel development, arteries are Ephrin-$B2^+$ while venous areas show EPHB4 positivity (Swift and Weinstein, 2009). Angiogenesis is the formation of new vessels from pre-existing vessels. This occurs either by sprouting and elongation, referred as sprouting angiogenesis, or by intussusception, a mechanism by which existing vessels are split and remodelled (Carmeliet and Jain, 2011a). In cancer, tumor cells can sequester the existing vasculature (co-option) or cover it by replacing endothelial cells (vascular mimicry). Moreover, cancer stem-like cells can themselves form tumor endothelial cells (Carmeliet and Jain, 2011a).

Adult endothelial cells are quiescent, characterized by a long half-life and protected against insults by maintenance signals belonging to VEGF, NOTCH, angiopoietin 1 (ANG1) and fibroblast growth factor (FGF) pathways. Moreover, endothelial cells present oxygen sensors like prolyl hydroxylase domain-containing protein (PHD) 1, 2 and 3, that are able to regulate members of the hypoxia-inducible factors (HIF) family and respond to hypoxic stimuli from the blood (Bruick, 2003).

Pericytes detach from the vessel wall when angiogenic signals like VEGF, ANG2, FGFs or chemokines are released by inflammatory or tumor cells. After proteolytic membrane degradation by MMPs, the permeability of endothelial cells increases and the nascent vessel starts growing (Carmeliet and Jain, 2011a).

The angiogenic process is very complex, requiring the coordinated action of several molecules. VEGF-A is a crucial factor in angiogenesis, because it drives the embryonic vascular development and regulates already existing and newly formed vessels in the adult organism (Giacca, 2010). VEGF-A can be spliced into different isoforms, among which VEGF-A_{165} is the most abundant and biologically active in mediating endothelial cell proliferation and migration by binding to its receptors VEGFR1 (or FLT1) and VEGFR2 (or FLK1). The non-tyrosine kinase receptor Neuropilin 1 (NRP1) is an important VEGF-A_{165} co-receptor, able to significantly enhance the affinity of $VEGFA_{165}$ to VEGFR2 (Jia et al., 2006). NRP1 has been originally described as the receptor of semaphorin 3A (Sema3A), a member of the semaphorin family that is able to guide cell migration of many cell types and block angiogenesis *in vivo* (Gioelli et al., 2018; Zacchigna et al., 2008). NRP1 has been shown to recruit myeloid cells of bone marrow origin to the sites of neoangiogenesis after specific interaction with VEGF-A_{165}, thereby stimulating vessel maturation by attracting resident smooth muscle cells (Zacchigna et al., 2008).

VEGF drives angiogenesis when it binds to VEGFR2 on endothelial cells. The current model of vessel sprouting involves the existence of a subpopulation of endothelial cells called tip cells, placed at the edge of the sprout and able to sense the angiogenic stimulus by expressing the highest levels of VEGFR2 on their membrane (Vandekeere et al., 2015). Tip cells protrude filopodia to scan the surrounding environment in search of angiogenic cues. The expression of NOTCH ligand DLL4 in the tip cell activates NOTCH receptors in neighbouring cells. This leads to the nuclear translocation of NICD and the downregulation of VEGFR2, thereby causing neighbouring endothelial cells to become stalk cells (Carmeliet and Jain, 2011a). The specialisation into either tip cell or stalk cell is not fixed, but rather dynamically interchangeable (Jakobsson et al., 2010). When a connection is formed between tip cells of different branches, all endothelial cells become quiescent to form the final vessel network (Carmeliet, 2000).

Lymphangiogenesis

After vasculogenesis and primary sprouting of venous blood endothelial cells, lymphatic endothelial cells (LECs) develop from venous progenitors, characterized by the expression of high levels of Prox1. Prox1 is an essential regulator of lymphatic cell specification both during embryonic development and postnatally (Wigle et al., 2002). The newly formed lymphatic cells migrate away from the veins when their cell surface receptor VEGFR3 (or FLT4) interacts with VEGF-C, as demonstrated by VEGF-C knockout mice, in which LECs express identity markers but do not migrate (Karkkainen et al., 2004).

Different subtypes of LECs, characterized by the expression of differential markers, are responsible for lymphatic vessel heterogeneity. Some LECs contribute to the formation of superficial lymphatic vessels and are characterized by a high expression of Neuropilin 2 (NRP2) and low levels of LYVE-1, while larger lymphatic trunks are associated with low levels of NRP2 and high expression of LYVE-1 (Bautch and Caron, 2015).

As the lymphatic system is responsible for draining fluids and provides a route of transport for inflammatory cells, it undergoes several changes after injury. For example, lymphangiogenesis has been detected in hearts displaying arrhythmias, atherosclerosis and myocardial infarction, likely as an attempt to resolve the increased interstitial fluid pressure and clear the inflammatory infiltrate after cardiac insult. (Klotz et al., 2015; Lupinski, 2009). In cancer patients enhanced lymphangiogenesis is correlated with early metastasis. Patients with breast cancer treated with hormonal or anti-angiogenic therapies often fall back into secondary tumors in their lymph nodes (Kerbel, 2011). A few drugs, such as Tivantinib, Onartuzumab, Rilotumumab, Trebananib, and IMC-3C5 have been developed to target mostly the VEGF-C/VEGFR3 signalling axis and are currently being tested in clinical trials (Dieterich and Detmar, 2016; Saif et al., 2016). Another compound of natural origin called AD0157 has been recently

demonstrated to have anti-angiogenic and anti-lymphangiogenic action, efficiently reducing tumor growth and lymph node metastasis in mice with human breast cancer xenografts (Garcia-Caballero et al., 2017).

Tumor vessels and angiogenesis

Tumor vessels are tortuous, irregularly branching and present random connections in a chaotic network. The tumor shows a spectrum of vessel subtypes, from big vessels to capillaries, and sometimes presents vascular malformations and glomeruli (Carmeliet and Jain, 2011a). The diameter and the spatial density of vessels is highly variable among tumors and also inside the same tumor mass, due to the vessel compression by cancer and stromal cells (Carmeliet and Jain, 2011b).

While the endothelium in normal vessels is formed by a quiescent and polarized monolayer of endothelial cells, tumor endothelial cells often lose their polarity, detach from the basement membrane and pile up on top of each other. Endothelial cells are leaky, and present wide junctions with multiple fenestrations, leading to haemorrhage and increased interstitial fluid pressure, which limits perfusion (Carmeliet and Jain, 2011b).

In tumors, endothelial cells sometimes switch their phenotype to acquire abnormal functions. For example, sinusoidal endothelial cells in a healthy liver have characteristics that facilitate perfusion and the exchange of metabolites, like fenestrations, wide junctions and the lack of a basement membrane. In contrast, endothelial cells in hepatocellular carcinoma become capillarized, less fenestrated, present more junctions and a large perivascular matrix, reducing both perfusion and oxygen transport (Yang and Poon, 2008).

Finally, in contrast to healthy vessels which transmit upstream signals via gap junctions to prevent shunting, anti-shunt strategies in tumor vessels are absent, resulting in aberrant and heterogeneous flow distribution (Pries et al., 2010).

Besides endothelial cell alterations, the entire vessel wall is abnormal in cancer. Stellate-shaped pericytes normally provide mechanical stability to the fragile endothelium, forming umbrella-like structures that tighten endothelial cells and regulate barrier function. Pericytes act as endothelial safeguards, suppressing endothelial cell growth and releasing low levels of VEGF. They also regulate microvascular flow and permeability (Diaz-Flores et al., 2009).

In most cancers, pericytes loosely connect with endothelial cells and their processes extend deeply inside the stroma. The abnormal shape of the cancerous pericytes is associated with the expression of markers of immature cells and the resulting hyper-variable coverage of vessels impairs efficient blood flow.

The normal function of the basement membrane is to provide structural stability to the associated pericytes and endothelial cells, controlling selective filtration of solutes and cells and

storing angiogenic factors. In most tumors, the basement membrane loses its strong association with the endothelium and has an abnormal thickness, often disrupted by holes. Moreover, its composition is altered, and wide extensions are projected deeply into the perivascular interstitium. In this way, vasodilation, perfusion and nutrient exchange are inhibited (Yang and Poon, 2008).

The continuous formation of abnormal vessels is induced by the pro-angiogenic factors produced by the tumor, that stimulate a non-productive form of angiogenesis, characterized by increased density of the vasculature and decreased tissue perfusion (Carmeliet and Jain, 2011a).

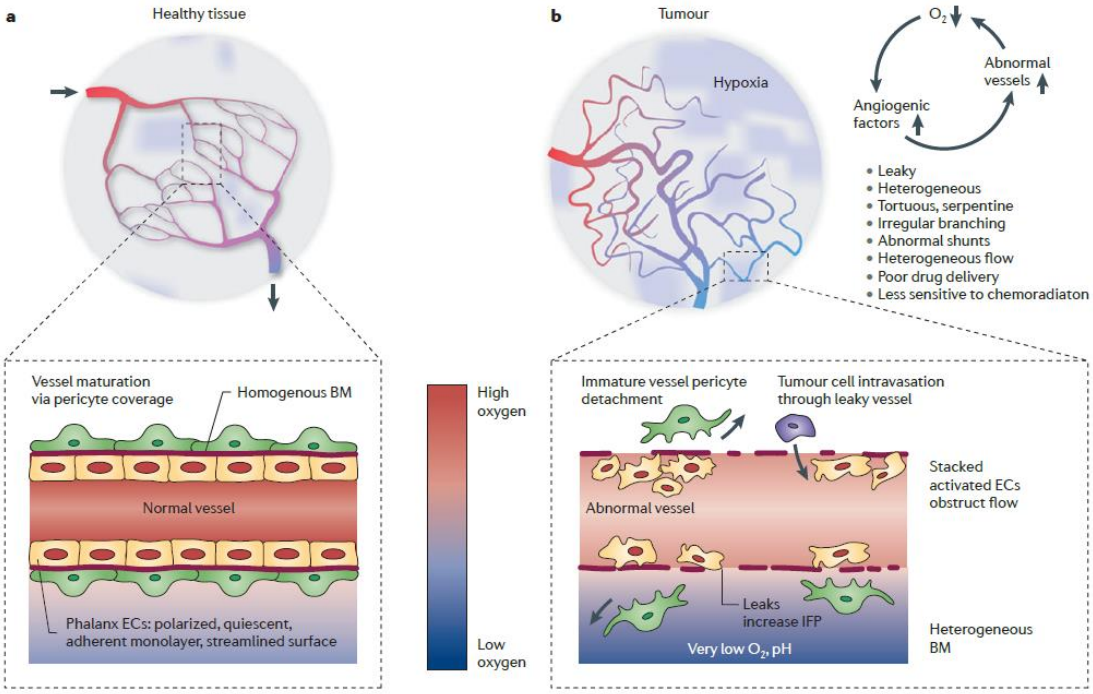

Figure 4. Tumor vessels display abnormal properties. *(A) In healthy condition, a normal vessel network with stable endothelium is formed. (B) Tumor vasculature exhibits vessel abnormalities, promoting cell motility and severe hypoxia. Reprinted from (Carmeliet and Jain, 2011b).*

Targeting the tumor vasculature for cancer therapy

As described above, tumor vessels present abnormal features in their structure and function. The acidic pH, the high interstitial fluid pressure and the hypoxia in the tumor microenvironment play a role in inducing the production of pro-angiogenic factors by cancer and stromal cells and aggravating vessel disorganization (Carmeliet and Jain, 2011b).

Traditionally, the main strategy to contrast cancer growth attempts to block access to nutrients, either by destroying existing vessels inside the tumor and/or suppressing new vessel formation by targeting VEGF. By inhibiting VEGF, ANG1 is upregulated and promotes endothelial cell tightening and recruitment of pericytes (Winkler et al., 2004). Moreover, VEGF blockage activates metalloproteinases that remodel the cell matrix (Vosseler et al., 2005). Several studies have demonstrated that after VEGF blockage the tumor mass experiences reduced interstitial fluid pressure, increased oxygenation and perfusion, with subsequent increased drug delivery and sensitivity to radiotherapy (Vosseler et al., 2005). However, some concerns about therapies that aim at blocking VEGF signalling have recently emerged, as they are not as efficient as expected.

A newer, promising strategy involves the normalization of the tumor vasculature, aiming at repairing vessel abnormalities thus leading to improved tumor oxygenation and decreased interstitial fluid pressure (Jain, 2001). According to this strategy, low doses of pharmacological VEGF inhibitors stimulate transient vessel normalization by reducing vessel size and tortuosity and increasing maturation of the basement membrane. The normalization of tumor vessels has been shown to reduce intravasation and metastasis and improve the delivery of chemotherapic agents (Mazzone et al., 2009).

The ANG-TIE receptor axis is a major player in vessel normalization. The binding of ANG2 to its receptor TIE2 induces vascular leakiness, whereas pericyte-released ANG1 leads to normal vessels (Stoeltzing et al., 2003). Blocking ANG1 or overexpressing ANG2 combined with VEGFR2-targeted therapy impairs pericyte coverage and vascular normalization in glioblastomas (Chae et al., 2010). In contrast, vessel normalization is improved when both VEGF and ANG2 are inhibited (Koh et al., 2010).

Another strategy to normalize tumor vessels targets PHD2, which plays an important role in determining vessel disorganization in cancer. When blood vessels supply enough oxygen, PHD2 hydroxylates HIF, causing it to be degraded. In contrast, under hypoxic conditions, active HIF induces angiogenesis and increases tissue oxygen levels. Experimentally, it was shown that PHD2 haplodeficient endothelial cells switch cancer cell metabolism toward aerobic glycolysis and form more mature vessels. This results in the upregulation of vascular endothelial cadherin CDH5, which tightens endothelial cell connections, and leads to upregulation of the soluble

form VEGFR1, which in turn traps the pro-angiogenic signal of VEGF (Ambati et al., 2006; Mazzone et al., 2009).

The inhibition of 6-Phosphofructo-2-Kinase/Fructose-2,6-Biphosphatase 3 (PFKFB3) in endothelial cells has also been shown to improve vessel stability by increasing VE-cadherin protein levels, resulting in tightening of the endothelial cell monolayer, better perfusion and oxygenation (Cantelmo et al., 2016).

Furthermore, the level of nitric oxide (NO), a strong stimulator of angiogenesis, is disturbed in tumors. Neuronal NO synthase (nNOS) in glioblastoma, and inducible (iNOS) in breast cancer have been recognized to alter the NO gradient. Their silencing in tumor cells restores the gradient of NO around blood vessels resulting in vessel normalization (Heller, 2009).

Platelet derived growth factor (PDGF) is a strong mitogen and chemoattractant for mesenchymal and glial cells. Strategies of vessel normalization involve the modulation of the PDGF/PDGFR axis, frequently upregulated in pancreatic, colon, and ovarian cancer patients with poor outcome. (Weissmueller et al., 2014). Another study reported that blocking PDGFRB improves drug delivery and sensitivity to chemotherapy (Klosowska-Wardega et al., 2009).

Finally, inhibition of the regulator of G-protein signalling 5 (RGS5) leads to vessel maturation and normalization. This molecule is produced by tumor pericytes and hypoxic endothelial cells. When blocked, the vascular density is increased and more regular, as demonstrated in a model of pancreatic islet cancer in RGS5-deficient mice (Hamzah et al., 2008).

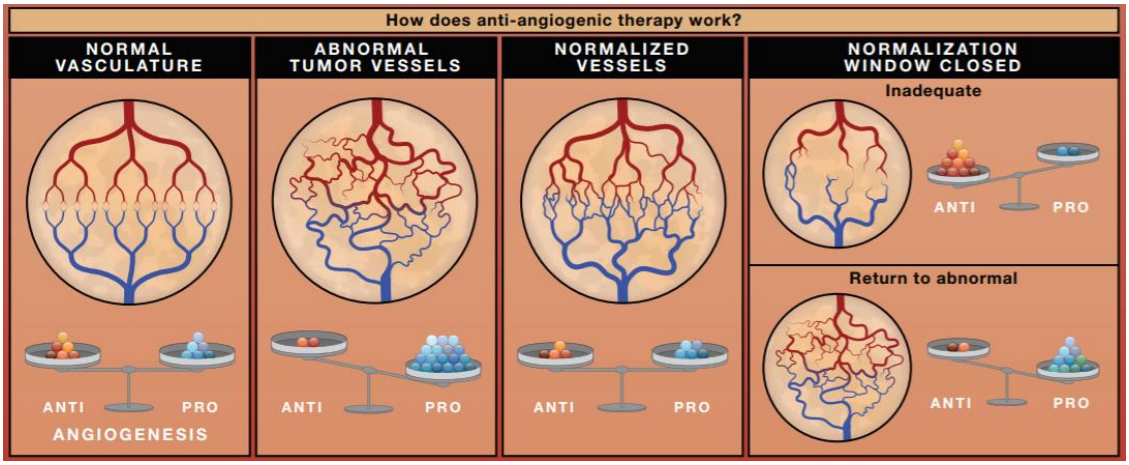

Figure 5. Tumor vessel normalization is a novel strategy for cancer treatment. *Abnormal tumor angiogenesis is sustained by an imbalanced level of pro-angiogenic factors. Normalization aims at restoring the balance between pro- and anti-angiogenic factors, resulting in a more organized vasculature. Reprinted from (Jain and Carmeliet, 2012).*

1.4 Why is it so hard to destroy metastatic foci?

A key point in the progress of efficient anti-metastatic agents is the development of strategies able to block both the escape of the tumor cells from the primary tumor and the survival of disseminated cancer cells (Valastyan and Weinberg, 2011). Indeed, many agents failed to improve cancer patient survival because they targeted initial dissemination events, including the above mentioned MMPIs, the small molecule R428 (which blocks the receptor tyrosine kinase Axl), miR-10b antagonists and the natural inhibitor of microbial origin Migrastatin and its analogues (Holland et al., 2010; Lecomte et al., 2011).

The existing therapies, designed to destroy primary tumors, often showed limited action against metastatic lesions (Steeg, 2006). This could be due to either the poor efficiency of drug delivery and poor vascularization of metastatic foci or the spatial location of target organs, sometimes protected by physical barriers (such as the blood-brain barrier). Indeed, a homogenous delivery of drugs at metastatic sites is often impaired by unnatural pressure gradients and non-uniform blood flow patterns, caused by continuous vessel remodelling and vessel abnormalities (Carmeliet and Jain, 2011a).

It is also probable that cytotoxic agents are not able to destroy growing metastases because they principally target cells with an active cell cycle, whereas cancer cells often are in dormant state (Aguirre-Ghiso, 2007). Furthermore, tumor cells are extremely elastic and quickly adapt to contrast both the physiological responses and any treatments. Thus, the molecular identity of a metastatic nodule can be highly different compared to the original primary tumor or another metastasis, requiring a more specific therapeutic strategy. Furthermore, cancer cell evasion from the immune system occurs both through the activation of novel pathways and by the protection established by the niche, that is also chemoprotective. Thus, it is now clear that any therapy targeting cancer cells at the primary site is bound to fail if it disregards the tumor microenvironment and the frequent dissemination into other organs. Indeed, some attempts at targeting the tumor niche have already shown promising results for future cancer therapy, involving the modulation of tumor angiogenesis, hypoxia and ECM composition (Kaplan et al., 2005; Ye et al., 2014). Furthermore, cancer diagnosis would also be advantaged by a deep investigation of the tumor niche, as immuno-histological analysis could help to determine the specific propensity of a tissue to be metastasized by cancer cells compared to others and could thus be addressed more effectively when developing the treatment approach.

However, the combination of conventional cancer treatments with innovative therapeutic strategies such as targeting the tumor microenvironment seems to be the smartest perspective to contrast metastasis. Furthermore, the “seed and soil” theory suggests that a preventive or simultaneous treatment of the metastatic microenvironment would be beneficial for patients undergoing therapy for primary tumors.

1.5 Innovative therapies for cancer

1.5.1 Biotherapeutics

Starting from the FDA approval of the first biotherapeutic product, namely recombinant human insulin (Humulin) in 1982, the worldwide pharmaceutical market has been dominated by protein therapeutics reaching a profit of over $140 billion. Among the top-20 of the most expensive products in 2013, the majority treat inflammatory and autoimmune conditions, particularly targeting TNF, with a cumulative sale of $41 billion. The class of insulins represents the second most lucrative category, counting $21.5 billion in the same year (Walsh, 2014).

Typical biological therapeutics, which have been successfully introduced into clinical practice, include blood coagulation factors (such as Factor VIII and Factor IX) thrombolytic agents (tissue plasminogen activator), hormones (insulin, glucagon, growth hormone, gonadotropins), vaccines (hepatitis B surface antigen and human papilloma virus L1 capsid antigen), monoclonal antibodies, growth factors and nucleic acid-based products.

Monoclonal antibody (mAb) therapy approval rate has doubled since April 2010 and is still increasing nowadays (Chiavenna et al., 2017). Interestingly, from 2006 to 2008 biotherapeutics have received the largest approval compared to any other category, often representing modifications of already existing approved compounds to optimize delivery, pharmacokinetics or pharmacodynamics.

Several growth factors and cytokines are now widely used in a variety of clinical applications. Erythropoietin is used to treat anaemia in chronic kidney failure and myelosuppression. Interferons (IFN) are used for many purposes: IFNα is used in the treatment of chronic hepatitis B virus (HBV) and hepatitis C virus (HCV) infections and some types of cancer; IFNβ is indicated for multiple sclerosis; IFNγ has been approved in chronic granulomatous disease (Friedman, 2008). Granulocyte colony-stimulating factor (G-CSF) and granulocyte/macrophage colony-stimulating factor (GM-CSF) are recommended for patients receiving myelosuppressive chemotherapy with a high risk of febrile neutropenia, and the latter is also used to mobilize $CD34^+$ stem cells prior to bone marrow transplantation (Mehta et al., 2015). In addition, IGF1 and IGFBP3 are administrated in cases of growth failure in children (Cohen et al., 2014).

More recently, nucleic-acid based therapeutics have emerged as a promising therapeutic option. Oligonucleotides, short RNA and DNA molecules with catalytic function, short RNA with regulatory function (siRNA and microRNA), decoy RNA and DNA molecules and aptamers have been considered in several preclinical models and ongoing clinical trials. Pegaptinib (Macugen®) is an FDA-approved RNA-based drug that binds to VEGF, indicated for the treatment of age-related macular degeneration. Similarly, an siRNA targeting VEGFR-1 has

been developed and recently optimized to treat choroidal neovascularization in age-related macular degeneration (Lee et al., 2016). Interestingly, Imetelstat (originally known as GRN163L) is an oligonucleotide currently in phase II for cancer treatment, due to its efficacy in inhibiting telomerase activity and tumor cell growth (Frink et al., 2016).

1.5.2 Monoclonal Antibodies for cancer treatment

Monoclonal Antibodies (mAbs) targeting tumor-associated antigens involved in oncogenic pathways are the base of immunotherapies aiming at contrasting carcinogenesis by several mechanisms, such as blocking tumor angiogenesis and cell growth, modulating immune response or killing cancer cells (Chiavenna et al., 2017). A list of the most used mAbs is provided in Table 1.

One of the major targets of mAb-based therapies is EGFR, which includes a group of cell surface receptors involved in the growth of epidermal cells. The downstream signalling pathway can be altered by either the activation of the ligand or the increased expression levels of co-receptors (Marmor et al., 2004). Several tumors of epidermal origin show overexpression of EGFR, with consequent abnormal activation or dysregulation of its downstream pathway. In 2004, the FDA approved a recombinant, human/mouse chimeric mAb called Cetuximab (Erbitux®) for the treatment of metastatic colorectal cancer. By specifically inhibiting EGFR activation, tumor cell growth slows down, matrix metalloproteinases and VEGF production decrease and cell apoptosis is induced (*https://www.accessdata.fda.gov/drugsatfda_docs/label/2012/125084s0228lbl.pdf*). Two years later, in 2006, human mAb Panitumumab (Vectibix®) was also approved by FDA and is currently indicated for the treatment of some types of EGFR-expressing metastatic colorectal cancers (*https://www.accessdata.fda.gov/drugsatfda_docs/label/2009/125147s080lbl.pdf*). Finally, in 2015, the FDA approved a recombinant human IgG1 mAb called Necitumumab (Portrazza®) mostly for the treatment of metastatic squamous non-small cell lung cancer in association with gemcitabine and cisplatin treatment (Fala, 2016).

HER2 (also known as erbb2) is another tyrosine receptor, which can be activated by binding to any ligand-activated member of the EGFR family. Its overexpression –associated with bad prognosis in breast, gastric and oesophageal cancer- results in the activation of Ras-Raf-MAPK and PI3K-AKT signalling pathways, which in turn inhibit apoptosis and promote proliferation (Marmor et al., 2004). Trastuzumab (Herceptin®) is a humanized IgG1 kappa mAb approved by the FDA in 1998 targeting HER2 with an incompletely described mechanism of action. It is indicated for the treatment of HER2-overexpressing node positive, node negative and metastatic breast cancers, gastric and gastro-oesophageal junction adenocarcinoma (*https://www.accessdata.fda.gov/drugsatfda_docs/label/2010/103792s5250lbl.pdf).* A

complementary action is provided by Pertuzumab (Perjeta®, 2012), a recombinant humanized mAb that represents a novel therapeutic class called dimerization inhibitors. Indeed, it targets a different epitope compared to trastuzumab, functioning as an inhibitor of HER2 heterodimerization with any other member of the EGFR family (*https://www.accessdata.fda.gov/drugsatfda_docs/label/2013/125409s051lbl.pdf*).

Approved in 2015, the human-murine mAb Dinutuximab (Unituxin®) targets tumor-associated gangliosides, which are glycosylated lipids overexpressed on the surface of neuroblastoma cells, but not by normal brain cells. GD2 is the predominant molecule of the category, shown to activate the focal adhesion kinase (FAK) and the Lyn kinase, thereby promoting tumor invasion and malignancy (Gholamin et al., 2017). Dinutuximab is indicated for the treatment of neuroblastoma in paediatric patients (McGinty and Kolesar, 2017) (*https://www.accessdata.fda.gov/drugsatfda_docs/label/2015/125516s000lbl.pdf*).

Recently, Olaratumab (Lartruvo®) has been approved by the FDA to be used in patients with soft tissue sarcoma. This recombinant human IgG1 mAb targets platelet-derived growth factor receptor alpha (PDGFR-α), a tyrosine kinase receptor, the activation of which is required for the maintenance of a pro-tumorigenic microenvironment in several cancers (*https://www.accessdata.fda.gov/drugsatfda_docs/label/2016/761038lbl.pdf*).

Besides oncogenic pathways, mAbs can target other features of the tumor, including angiogenesis. Bevacizumab (Avastin®) is a recombinant humanized IgG1 mAb able to bind to all isoforms of VEGF-A, blocking the interaction and the activation of the receptors. This results in the normalization of tumor vasculature and inhibition of further neoangiogenesis. Bevacizumab received the first approval from the FDA in 2004 and nowadays it is indicated for the first line treatment of many metastatic conditions, like colorectal, ovarian and breast cancer, advanced non-small cell lung cancer (NSCLC) and glioblastoma (*https://www.accessdata.fda.gov/drugsatfda_docs/label/2009/125085s0169lbl.pdf*).

Ramucirumab (Ciramza®) blocks VEGFR2 receptor by binding to its extracellular domain and inducing conformational changes. It was approved in 2014 and is used to treat advanced or metastatic gastric or gastro-oesophageal junction adenocarcinoma (*https://www.accessdata.fda.gov/drugsatfda_docs/label/2014/125477lbl.pdf).*

Another strategy exploited by monoclonal antibody treatment is the targeting of immune checkpoints to enhance the effectiveness of the therapy. Indeed, tumor cells have been shown to activate immune response but also to be able to escape from recognition (Burnet, 1970; Dunn et al., 2004).

Ipilimumab (Yervoy®, 2011) increases T-cell activation and proliferation resulting in an enhanced immune responsiveness, by binding to CTLA-4, a negative regulator of T cells (*https://www.accessdata.fda.gov/drugsatfda_docs/label/2015/125377s073lbl.pdf*). It is used for the treatment of some forms of melanoma, with even higher improvement if administrated

in combination with Nivolumab (Opdivo®, 2014), used to block the programmed cell death protein 1 (PD-1), which in turn is a regulator of functionality of almost all immune cells (*https://www.accessdata.fda.gov/drugsatfda_docs/label/2014/125554lbl.pdf*).

PD-1 is also the target of Pembrolizumab (Keytruda®), a humanized mAb approved by FDA in 2014 and indicated for the treatment of metastatic NSCLC and metastatic head and neck squamous cell carcinoma (HNSCC) (*https://www.accessdata.fda.gov/drugsatfda_docs/label/2016/125514s012lbl.pdf*). Finally, Atezolizumab (Tecentriq®) has recently been approved for the treatment of metastatic urothelial carcinoma by blocking PD-1/PD-L1 (*https://www.accessdata.fda.gov/drugsatfda_docs/label/2016/761034s000lbl.pdf).*

Bone metastasis often relies on the binding of the receptor activator of NF-kB ligand (RANKL) with its receptor RANK, expressed on the osteoclast surface and leading to the activation of the host cell. Activated osteoclasts resorb bone, resulting in bone destruction. Denosumab (Xgeva®, Prolia®) is a human IgG2 mAb with high affinity and specificity for human RANKL, approved in 2013 (Xgeva®) for contrasting the rise of deleterious events in patients affected by bone metastasis. Prolia® has been approved in 2010 and it is currently indicated to increase bone mass in high-risk patients under androgen deprivation therapy for non-metastatic prostate cancer or adjuvant aromatase inhibitor therapy following breast cancer (*https://www.accessdata.fda.gov/drugsatfda_docs/label/2010/125320s0000lbl.pdf*).

mAB	Name	Type	Target	FDA approved[a]
Trastuzumab	Herceptin®	Humanized	HER2	HER2-positive metastatic/non-metastatic breast cancer HER2-positive metastatic gastric or gastroesophageal junction adenocarcinoma
Pertuzumab	Perjeta®	Humanized	HER2	HER2-positive metastatic breast cancer HER2-positive, locally advanced, inflammatory, or early stage breast cancer
Cetuximab	Erbitux®	Chimeric	EGFR	Metastatic CRC HNSCC
Panitumumab	Vectibix®	Human	EGFR	Metastatic CRC
Necitumumab	Portrazza™	Human	EGFR	Metastatic squamous NSCLC
Dinutuximab	Unituxin™	Chimeric	GD2	Pediatric high risk neuroblastoma
Bevacizumab	Avastin®	Humanized	VEGF-A	Metastatic CRC Recurrent or metastatic non-squamous NSCLC HER2-negative metastatic breast cancer (revoked in 2011) Metastatic renal cell carcinoma Persistent, recurrent or metastatic cervical cancer Glioblastoma Recurrent epithelial ovarian, fallopian tube, or primary peritoneal cancer
Ramucirumab	Ciramza®	Human	VEGFR-2	Advanced or metastatic gastric or gastroesophageal junction adenocarcinoma Metastatic NSCLC Metastatic CRC
Olaratumab	Lartruvo®	Human	PDGFR-α	Soft tissue sarcoma
Ipilimumab	Yervoy®	Human	CTLA-4	Unresectable or metastatic melanoma Cutaneous melanoma
Nivolumab	Opdivo®	Human	PD-1	Unresectable or metastatic melanoma Metastatic squamous NSCLC Metastatic NSCLC Advanced RCC Recurrent or metastatic HNSCC
Pembrolizumab	Keytruda®	Humanized	PD-1	Unresectable or metastatic melanoma Metastatic NSCLC Recurrent or metastatic HNSCC
Atezolizumab	Tecentriq™	Humanized	PD-L1	Locally advanced or metastatic urothelial carcinoma Metastatic NSCLC
Ado-trastuzumab emtansine[b]	Kadcyla®	Humanized	HER2	HER2-positive metastatic breast cancer
Denosumab	Xgeva®	Human	RANKL	Bone metastases from solid tumors

CRC colorectal cancer, *HNSCC* head & neck squamous cell carcinoma, *NSCLC* non-small cell lung cancer, *RCC* renal cell carcinoma
[a]See the text for further details
[b]Trastuzumab covalently linked to emtansine (DM1)

Table 1. Summary of the monoclonal antibodies approved by the FDA for the treatment of solid tumors. *Reprinted from (Chiavenna et al., 2017).*

1.5.3 Antibody-drug conjugates

Antibody-drug conjugates (ADCs) are combinations of cytotoxic drugs with mAbs physically connected by a chemical linker. Once the ADC is inside the cell, the linker is cleaved, releasing the toxic moiety. More than 40 ADCs have entered in clinical trial targeting both solid and blood cancers (Mathur and Weiner, 2013). An example of this class of compounds is ado-trastuzumab emtansine (Kadcyla®) formed by the humanized mAb trastuzumab combined with the microtubule inhibitory drug DM1. Its action is related not only to HER2 pathway inhibition, but also to the inhibition of the tubulin polymerization on HER2-overexpressing cells. Ado-trastuzumab emtansine has been approved by the FDA in 2013 and is indicated for the treatment of HER2-positive metastatic breast cancer (*https://www.accessdata.fda.gov/drugsatfda_docs/label/2013/125427lbl.pdf*).

1.5.4 Gene therapy and AAV vectors

Gene transfer is a potential strategy to define novel targets and treat at least some types of cancer. The biggest problem encountered by most gene therapy applications is related to the difficulty of polyanions, such as DNA and RNA, to cross cell membranes, which are made up of nonpolar, hydrophobic phospholipids. The idea of using viral vectors to deliver genetic information has dramatically changed the efficiency of gene therapy. Over the last year, our laboratory and others have gained valuable experience in the delivery of various VEGF family members for various therapeutic application, such as the induction of therapeutic angiogenesis in the skeletal muscle and in the heart (Arsic et al., 2004; Ferrarini et al., 2006), the promotion of muscle regeneration in muscular dystrophies (Messina et al., 2007) and the protection from motor neuron loss in amyotrophic lateral sclerosis (Azzouz et al., 2004).

In the mid-1980s, Adeno-Associated Viruses (AAV) emerged as the most promising viruses easily genetically modified to obtain safe and efficient vectors for gene therapy. AAV is a small (25-nm) non-enveloped, parvovirus with an icosahedral capsid architecture, the infection ability of which depends on a separate helper virus. Its genome (≈4.7 kb) consists of two open reading frames (ORFs) encoding for rep and cap proteins, for replication and capsid assembling, which are flanked by inverted terminal repeats (ITRs, ~145 bp) (Xiao et al., 1997).

Recombinant AAV (rAAV) vectors show efficient transduction of both dividing and non-dividing cells, and particularly high tropism for post-mitotic tissues like brain, heart and skeletal muscle (Asokan et al., 2012). More than hundred AAV serotypes have been identified so far, but only 12 have been vectorized. Some of them are able to cross the endothelial barrier, allowing a widespread transduction of the body, particularly skeletal muscle and heart, if injected intramuscularly or intraperitoneally (Zhang et al., 2011). Differing from adenoviral vectors, AAVs are safe and do not trigger any inflammatory response. They predominantly persist as stable circular episomes, minimizing the risk of insertional mutagenesis and allowing for long-term gene expression in tissues (Zacchigna et al., 2014).

1.5.5 Current gene therapy applications and clinical trials

A few gene therapy products have been marketed in Europe. For example, Alipogene tiparvovec (GlyberaR®) is a recombinant AAV for the treatment of lipoprotein lipase deficiency and Strimvelis® is a lentiviral vector for the therapy of severe combined immune deficiency. Other gene therapies are under review in the United States, such as an rAAV2 product for a congenital form of blindness, while many more are in clinical trials (Keeler et al., 2017).

Retroviral and lentiviral vectors are becoming the vectors of choice for the treatment of haematopoietic diseases. A promising therapy for the treatment of B-cell lymphomas and leukemia is the use of chimeric antigen receptor T (CAR-T) cells against the B-cell surface

antigen CD19, produced by *ex vivo* transduction of T cells with lentiviral or retroviral vectors and re-injected into the patient. To date, Kymriah and Yescarta are the only two CD19-specific CAR-T agents approved by both the FDA and the European Medicines Agency, for the treatment of Acute lymphoblastic leukemia and Non-Hodgkins lymphoma, respectively. Moreover, the use of both drugs is indicated to treat the diffuse large B-cell lymphoma (https://nucleusbiologics.com/resources/kymriah-vs-yescarta/).

Adenoviruses induce robust transduction but also a strong immune response. Most people have antibodies against the most common serotype 5. As a consequence, clinical trials using adenoviral vector are finding their niche of application when used as oncolytic viruses in cancer therapy. In this context, the triggered robust immune response is beneficial for the therapeutic outcome. Other oncolytic vectors rely on herpesviruses, such as Talimogene Laherparepvec (Imlygic®), expressing human GM-CST and approved for the treatment of melanoma (Rehman et al., 2016).

Recombinant AAV vectors have been tested in hundreds of clinical trials for recessive monogenic disorders. Clinical efficacy of AAV vector-based gene therapy has so far demonstrated in clinical trials for the therapy of haemophilia B (rAAV carrying human factor IX), alpha-1-antitrypsin deficiency and Leber congenital amaurosis (rAAV2 carrying the human retinal pigment epithelium gene RPE65). Other rAAV vectors that have reached phase II/III clinical studies are listed in Table 2. Extensive capsid engineering has expanded the repertoire of AAV vectors available for gene delivery, to selectively target cells or organs, and reduce transgene expression in off-target organs, thereby increasing the therapeutic effect (Zacchigna et al., 2014).

Disease	**Vector**	**Outcomes**	**Location of the Trial**
Lipoprotein lipase deficiency (LPLD)	AAV-Glybera	Improved lipid profile and decreased pancreatitis	USA
X-linked adrenoleukodystrophy	Lentivirus	Improved neurologic development	France
Thalassemia major	Lentivirus	Decreased transfusion need	USA
X-linked/choroidemia rentinal disease (REP1)	AAV2	Improved vision	USA – multiple countries
Leber congenital amaurosis type 2 (LCA)	AAV2	Improved low-light vision	USA
Leber hereditary optic neuropathy	AAV2	Improved vision	France – multiple countries

Table 2. Summary of the clinical trials based on gene therapy for monogenic diseases in phase III/IV. *Adapted from (Keeler et al., 2017).*

1.5.6 *In vivo* Functional Selection (FunSel) for discovery of anti-invasive factors

The screening of genetic libraries *in vitro* has always been a powerful tool for the identification of novel factors. However, it presents a major limitation, namely, it cannot predict the relevance of the candidate molecules *in vivo*. Therefore, the unbiased screening of genetic libraries directly *in vivo*, with compounds selected according to their exerted function rather than *a priori* information, represents a novel and promising tool for the identification of therapeutic factors. AAV vectors stand as the optimal tool for the achievement of this ambitious objective.

The Molecular Medicine Laboratory at ICGEB developed a strategy called FunSel, which aims at selecting novel factors by screening a library of secreted proteins *in vivo*, using selection pressure by applying a specific stimulus or stress. The screening is performed using vectors coding for secreted proteins, as this makes it possible to select factors which can later be therapeutically administered as a recombinant protein or synthetic peptide, rather than by viral vectors. A library of sequence-verified AAV plasmids was produced, codifying for 1200 secreted factors of different categories (such as cytokines, hormones, secreted enzymes, ECM proteins, and proteins with unknown function). The library was divided into pools of 50 factors each, depending not on category but by grouping similarly sized coding sequencies. Each cDNA is under the control of an immediate–early cytomegalovirus (CMV IE) promoter in AAV plasmids that were subsequently produced with an AAV capsid of serotype 2 in order to efficiently transduce the heart, as described in Ruozi et al. (Ruozi et al., 2015).

The FunSel strategy was first applied for the selection of therapeutic molecules for acute myocardial infarction (MI) and limb ischemia. Viral DNA was recovered from the ischemic muscle after both the transduction with the pool of AAV vectors and the selective stimulus (descendant coronary artery ligation). Recovered DNA was re-cloned into AAV vectors to repeat the cycle of selection *in vivo* and allow the enrichment of transgenes exerting a protective role for the muscle (Figure 6A). Finally, having screened 100 factors belonging to the murine secretome under the selection insult induced by an acute ischemia in the muscle, the hormone ghrelin was selected as the top enriched transgene. Ghrelin was then characterized and was demonstrated to inhibit apoptosis through the induction of autophagy, resulting in a potent protection of the tissue after insult (Ruozi et al., 2015).

In the most recent applications, the FunSel strategy has been improved by the introduction of 10 base-pair (bp) sequences of nucleotides (barcodes) uniquely identifying each transgene of the library, thus allowing for the usage of Next Generation Sequencing (NGS) to analyse the enrichment of the factors. A schematic representation of the AAV plasmid encoding for the secreted factors of the library is shown in Figure 6B. The barcode has been placed immediately after the cDNA and a primer binding site, enabling the specific amplification by two sequential amplifications by polymerase chain reaction (PCR). The first primer pair amplifies the barcode

by binding to regions of the AAV plasmid, whereas the second primer pair includes Illumina adapters to allow the sequencing by Illumina NGS. This method has been validated by Bortolotti et al. and was exploited to select for factors that positively enhance engraftment of mesenchymal stromal cells (Bortolotti et al., 2017). Mesenchymal stromal cells have been transduced *ex vivo* with AAV2 encoding for gene pools belonging to the murine secretome library and transplanted into either the normal heart or the ischemic heart (Bortolotti et al., 2017). The experiment resulted in the enrichment of a pro-hypertrophic cytokine belonging to the IL6 family, namely Cardiotrophin 1 (Ctf1), which significantly preserved cardiac function and reduced infarct size, promoting cell engraftment and offering a useful strategy to improve cell therapy for MI (Bortolotti et al., 2017).

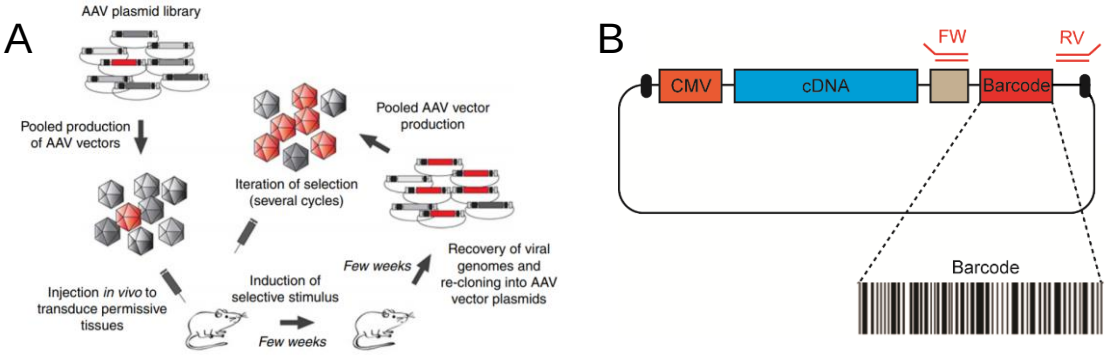

Figure 6. FunSel strategy. *(A) The scheme refers to the first application of FunSel, when the AAV library was screened in vivo in a model of myocardial infarction. The DNA was extracted and amplified by PCR. The enriched transgenes, evaluated by NGS, were subjected to another cycle of selection in vivo. (B) Each transgene of the secretome library is inserted in AAV plasmids containing the ITRs (in black), a CMV promoter (in orange), the coding sequence (in blue) and a unique 10 bp-long barcode (in red). The forward (FW) primers for the two-step PCRs bind to the primer binding site between the cDNA and the barcode and the reverse (RV) primers bind to the common region of the plasmid after the barcode.*

2. MATERIAL AND METHODS

2.1 Secretome library and AAV production

A library of 1200 secreted factors has been created by the Molecular Medicine lab at the ICGEB and divided into 24 pools of 50 transgenes each, grouped into similarly sized coding sequences (Ruozi et al., 2015). Each coding sequence was cloned into a modified pZac2.1 vectors (called pGi) under the control of the CMV IE promoter. At the 3' of each cDNA, a specific 10 bp sequence, called barcode, was inserted and uniquely identifies each transgene. This method was validated in a recently published work (Bortolotti et al., 2017). Recombinant AAV vectors were prepared by the AAV Vector Unit at ICGEB in Trieste (*https://www.icgeb.org/avu-core-facility/*). Serotype 9 was used to transduce the skeletal muscle (Zacchigna et al., 2014) and serotype 6 to transduce the lung (Halbert et al., 2001). Viral preparations had titers between 10^{12} and 10^{13} viral genomes (vg) per 1 mL. An empty vector (AAV-CTR) was used as control.

2.2 Screening of the library *in vivo*

Each pool of the library of AAV9 was injected bilaterally in the *tibialis anterior* muscle of adult C57BL/6 mice (3 x 10^{10} viral genomes per muscle, 5 animals per pool). One week later 50,000 LLC cells were injected in the same muscles of 3 mice. After 10 days, mice were sacrificed and the total DNA was extracted from muscles using the DNeasy Blood & Tissue Kit (Qiagen, #69504), following manufacturer instructions. Barcodes were amplified by two subsequent cycles of PCR, using the primers listed in Table 3 and validated in (Bortolotti et al., 2017). The first primer pair anneals to a common region on the plasmid vector (pGi-FW and pGi-RV) whereas the second PCR exploits a common forward primer (FW-Illumina) and 48 reverse primers that include Illumina adapters (RV-Illumina 1-48). Amplicons were sequenced using HiSeq 2000 Illumina by IGA Technology Services in Udine.

Target	Primer name	Sequence
pGi plasmid	pGi-FW	5′- CTAGCAAAATAGGCTGTCCC-3′
	pGi-RV	5′- TGGTTTGTCCAAACTCATC-3′
Illumina seq	FW-Illumina	5′-AATGA-oligo-TCTCTAGCAAAATAGGCTGTCCC-3′
	RV-Illumina 1-48	5′-CAAGC-oligo-TCTTGGTTTGTCCAAACTCATCAA-3′

Table 3. Primers for the two-step PCR amplification of barcodes. *Adapted from (Bortolotti et al., 2017)*

2.3 Cell culture

Cancer cells from the lung, namely LG1233 lung cancer cells derived from $Kras^{G12D/+;}Trp53^{-/-}$ mice (LG) and LLC, from melanoma (B16-F10), NIH-3T3 immortalized fibroblasts and human embryonic kidney 293T (HEK-293T) cells were grown in Dulbecco's Modified Eagle Medium (DMEM, Sigma) supplemented with 10% fetal bovine serum (FBS) and antibiotics (penicillin/streptomycin, 100 µg/mL).

Human umbilical vein endothelial cells (HUVECs) were cultured in EGM-2 medium (Lonza, #CC-3162). The plates were coated with a mixture of gelatin (Sigma #G9391, final concentration 0.2 mg/mL) and fibronectin (Invitrogen #33010-018, final concentration 1 mg/mL).

Immortalized mouse aortic endothelial cells (iMAEC) were cultured in DMEM supplemented with endothelial cell growth supplement (ECGS, 25 µg/ml), 1% minimum essential media non-essential amino acids solution (MNEAA, Gibco), 10% FBS, and antibiotics. The plates were pre-coated with 0.1% gelatin.

2.3.1 Primary cell isolation

Primary endothelial cells and fibroblasts were isolated from adult liver of C57BL/6 mice. The organs were extracted, cut in small pieces and rinsed with calcium- and bicarbonate-free Hank's solution with HEPES (CBFHH). The tissue was digested incubating with an enzyme mix following the manufacturer's instructions (Skeletal muscle dissociation kit, Miltenyi Biotec; #130-098-305), for 1 hour at 37°C in agitation. The solution was filtered using a 70 µm-pore size cell strainer (Falcon) and centrifuged at 400 x g for 10 minutes.

For fibroblast isolation, the pellet was resuspended in DMEM supplemented with 10% FBS and antibiotics and plated in a 10 cm-dish to allow for fibroblast attachment. After 2-3 hours, the supernatant was removed, the plate was washed with phosphate-buffered saline (PBS) and fibroblasts were grown in DMEM/10% FBS and antibiotics.

For endothelial cell isolation, the pellet was resuspended in a solution containing PBS/0.5% Bovine Serum Albumin (BSA, Sigma) and 0.5 M EDTA and incubated with 1:100 anti-CD31 magnetic MicroBeads (Miltenyi Biotec, #130-097-418) for 15 minutes in the dark. The $CD31^{+}$ cells were selected and washed through an LS column (Miltenyi Biotec, #130-042-401) and subsequently placed in the magnetic field separator. Primary endothelial cells were grown on plates coated with a mixture of gelatin and fibronectin as reported above in EGM-2 culture medium.

To isolate skin fibroblasts, the abdominal skin portion was collected, washed and cut into small pieces. In order to separate the epidermis from the underlying layers, the tissue was digested

with 5 mg/mL dispase-2 dissolved in CBFHH buffer for 18-20 hours at 4°C. Subsequently, the epidermis was further digested in an enzymatic mixture composed of 1 mg/mL type-1 collagenase (Worthington Biochemical Corporation), 0.4 mg/mL DNase-2 (Sigma), penicillin-streptomycin and dissolved in CBFHH buffer and mechanically blended through rotation performed for 1 hour at 37°C, using a magnetic stirrer. DMEM supplemented with 20% FBS was added to stop the enzymatic reaction and the cell suspension was filtered using a 70 µm-pore size cell strainer. After centrifuging the digested tissue at 400 x g for 10 minutes, the pellet was re-suspended in DMEM/10% FBS and plated in a 10 cm-dish. After 2-3 hours, the supernatant was removed, the plate was washed with PBS and fibroblasts were grown in DMEM/10% FBS and antibiotics.

2.3.2 Transfection of HEK-293T and production of enriched supernatant

HEK-293T cells were cultured until 70% of confluence and transfected as follows. A mixture of DNA (10 µg in a 60 mm-dish), 60 µL of 2M $CaCl_2$, and water was added drop-wise to 500 µl of 2X HEPES Buffered Saline (HBS) in agitation. After 10 minutes of incubation at RT, the transfection mix was added drop-wise to the cells in antibiotic-free cell culture medium with 10% FBS. Transfection using a plasmid encoding for EGFP was used as a positive control to check transfection efficiency (consistently higher than 90%). One day after transfection, the cell culture medium was replaced with DMEM supplemented with 10% FBS and antibiotics and kept for one day to allow cells to recover. Then, the cell medium was substituted with FBS-free DMEM supplemented with antibiotics. The enriched supernatant was recovered 24 hours later, centrifuged at 300 x g for 5 minutes to remove cell debris and stored at -80°C.

2.3.3 Migration assays

Transwell Permeable Supports (Corning, #3421) were used to test cell migration. The cells (5 x 10^4 iMAEC or 10^5 LLC cells) were seeded in the upper part of the membrane in FBS-free medium, and 600 µL of serum-free supernatant from HEK-293T cells was added in the bottom of the well. The supernatant collected from HEK-293T cells transfected with an empty pGi plasmid served as negative control for cell migration. The transwell migration assay was also performed after addition of 10% FBS to the supernatants.

For wound healing, cells were starved for 6 hours and seeded at confluence in the two chambers of the support (IBIDI, #80209), and placed in a 24-well plate. After attachment, the cells were carefully washed with PBS to remove detached cells and debris and incubated with the HEK-293T supernatants or the recombinant proteins at 37°C. Images were acquired immediately (T=0) and at later timing to assess cell migration.

2.3.4 Tube formation assay

The experiment was performed using the µ-slides from IBIDI (#81506), coated with growth factor reduced Matrigel (Corning, #356230). HUVECs were starved O/N in medium M199 with 0,1% FBS and then seeded on Matrigel (2000 cells per well) in Medium 199 (Sigma Life Science, #M4530) supplemented with epidermal growth factor (EGF, 10 ng/mL), basic FGF (bFGF, 20 ng/mL) and hydrochortisone (1 µg/mL).

The recombinant EMID2 was added either in the culture medium or into the Matrigel prior to polymerization at different concentrations. Mouse recombinant BD33 was added to the culture medium at different concentrations. Human recombinant TGFβ1 (hereafter referred to as TGFβ) was added at a concentration of 1 ng/mL into the medium. See Recombinant Proteins section below for the details on recombinant proteins that have been used.

Images were acquired 2-4 hours after cell seeding and the tubular structures were analysed considering commonly used parameters, namely the number of tubes, meshes and nodes and the percentage of coverage, measured using the ImageJ software (Fiji).

Tube formation assay was also performed with primary liver endothelial cells seeded on 5% Matrigel containing the recombinant EMID2 or normal diluted Matrigel. Recombinant $VEGF_{165}$ (here referred as VEGF) or BD33 were added into the culture medium. Cells were fixed with 4% PFA at 48 hours and stained for CD31 and DAPI. The quantification of the length of protrusions and the number of elongating cells was performed using the ImageJ software (Fiji).

2.3.5 Production of the extracellular matrix

The protocol that was followed for matrix production from fibroblasts was published by Franco-Barraza (Franco-Barraza et al., 2016).

The plates were pre-treated to stabilize anchoring of the matrix to the culture surface, then pre-coated with 0.2% gelatin for 1 hour at RT. After washing with PBS, 1% glutaraldehyde (dissolved in PBS) was added for 30 minutes at RT and then washed with PBS. The plates were incubated with 1 M ethanolamine (dissolved in water) for 30 minutes at RT and washed carefully with PBS.

Fibroblasts were cultured for 9 days in DMEM supplemented by 10% FBS, antibiotics, and 50 µg/ml of ascorbic acid. The medium was replaced every 48 hours.

To decellularize the matrix, the culture medium was carefully removed and rinsed twice with PBS, then incubated with a buffer composed of 0.5% Triton X-100, 20 mM NH_4OH in PBS for a few minutes at 37°C. Then, the extraction buffer was diluted with some millilitres of PBS and incubated overnight. The day after, the matrix was washed several times and NIH-3T3 cells were seeded on top of it.

To fix the plates, 1% glutaraldehyde was added for 30 minutes at RT and then washed with PBS. The plates were incubated with 1 M ethanolamine for 30 minutes at RT, washed with PBS and replaced by PBS for further immunostaining.

2.3.6 Activation of α-SMA-RFP/COLL-EGFP fibroblasts

Transgenic α-SMA-RFP/COLL-EGFP mice express the red fluorescent protein (RFP) under the control of the α-SMA promoter and the enhanced green fluorescent protein (EGFP) under the control of the collagen-1α1 promoter (Magness et al., 2004). Fibroblasts from the skin of α-SMA-RFP/COLL-EGFP adult mice were isolated and cultured in DMEM supplemented with 1% FBS and antibiotics. Cells were transduced with the AAV-CTR or AAV-EMID2 (MOI of 10^6 vg) for 24 hours to observe differential activation. In another condition, recombinant EMID2 was added into the culture medium at a concentration of 1 μg/mL and the medium was changed every day until the end of the experiment. The appearance of the red signal was checked daily at the microscope and the fibroblast culture was fixed after 3 days.

2.3.7 Proliferation assay

LLC and iMAEC cells were seeded at 60-70% confluence and incubated for 4 hours at 37°C with serum-free supernatant collected from HEK-293T cells transfected with pGi-BD33 or empty pGi. Alternatively, HUVECs were incubated with 100 ng/mL of the recombinant BD33 for 4 hours at 37°C. One hour before fixation, 10 mM 5-ethynyl2'-deoxyuridine (EdU) was added to the cell medium, to mark proliferating cells. Cells were fixed with 4% PFA for 10 minutes and then stained for DAPI and EdU, using the Click-it EdU Cell Proliferation Kit (Thermo Fisher, #C10338) following manufacturer instructions.

2.4 Animal experimentation

All animal experiments were conducted in compliance with the European guidelines and international laws and policies (*ECC Council Directive 86/609, OJL 348, 12 December 1987*), with the approval of ICGEB Animal Welfare Board, Ethical Committee, and Italian Minister of Health. Adult C57BL/6 and α-SMA-RFP/COLL-EGFP mice were used for animal experiments. We used experimental groups of animals composed by both males and females. They were housed under optimal environmental conditions.

2.4.1 Evaluation of angiogenesis *in vivo*

Adult C57BL/6 mice received intraperitoneal injections of 20 µL of AAV9-EMID2 (2 x 10^{10} vg per mouse) or the empty vector AAV9-CTR (2 x 10^{10} vg per mouse) at P0 and were sacrificed after 1 month. Alternatively, C57BL/6 mice were injected intraperitoneally with 20 µL of AAV9-EMID2 or AAV9-CTR (2x 10^{10} vg per mouse) and also with AAV2-VEGF (3 x 10^{10} vg per mouse) in the *tibialis anterior* muscles at 2 weeks. They were sacrificed after 2 additional weeks. Muscles were isolated and snap-frozen for immunostaining.

2.4.2 Skeletal muscle tumors

To select the best factor able to reduce tumor size *in vivo*, C57BL/6 3-month-old mice received intramuscular injection of 50,000 LLC cells together with 1.5 x 10^{10} vg of AAV9-PTH, AAV9-FGF3, AAV9-EMID2, AAV9-LCN12, AAV9-BD33 or AAV9-CTR. To characterize the function of EMID2, C57BL/6 or α-SMA-RFP/COLL-EGFP 3-month-old mice received intramuscular injection of 50,000 LG cells together with AAV9-EMID2 or AAV9-CTR (1.5 x 10^{10} vg per muscle). In an alternative experiment, 3 x 10^{10} vg of AAV9-EMID2 or AAV9-CTR were administered one week before the intramuscular injection of 50,000 LG. All the animals were sacrificed 10 days after cancer cell injection. Muscles from C57BL/6 mice were isolated and snap frozen for immunostaining whereas muscles from α-SMA-RFP/COLL-EGFP mice were fixed in 4% PFA and sucrose to preserve the endogenous fluorescence.

2.4.3 Lung metastasis

Adult C57BL/6 mice received intra-parenchymal injection of 20 µL of AAV6-EMID2 or AAV6-CTR (2 x 10^{10} vg per mouse) in the left lung. After 2 weeks, the same mice received intravenous injection of 10^5 LG or B16-F10 cells. Ten days after cancer cell injection, the animals were perfused with PBS from the right ventricle and lungs were fixed with 10% neutral buffered formalin overnight and then 50% ethanol until paraffin embedding.

2.5 Molecular biology

2.5.1 Recombinant proteins

The recombinant proteins that have been used for the experiments are listed in Table 3.

Species	Protein	Company and code	Expression Host
Mouse	EMID2	Tema Ricerca #CSB-BP820987MO	Baculovirus
Mouse	BD33	MyBioSource # MBS1345509	*E.coli*
Human	$VEGF_{165}$	R&D #293-VE	Baculovirus
Human	TGFβ1	Peprotech #100-21	HEK293 cells

Table 4. Recombinant proteins.

2.5.2 Western blot

The protein lysates were prepared in RIPA buffer (40 mM tris-HCl pH 7.5, 2 mM EDTA, 300 mM NaCl, 2% NP40, 1% Sodium desoxycholate) supplemented with protease inhibitors (Roche, Complete Mini #11836153001) and 20% SDS in H_2O. The tissue was disrupted in tubes containing ceramic beads (MP BioMedicals, #6913100) using a tissue homogenizer. The protein concentration was determined by spectrophotometer with Bradford quantification. Protein samples were separated in 10% polyacrylamide gel, prepared with Protogel (PolyMed, #EC890), 357 mM Bis-Tris HCl pH 6.8, APS and TEMED (Sigma). Chloroform was also added to the gel solution (0.5% v/v), to allow protein visualization (stain-free gel). To compare proteins in the supernatants, an equal volume of sample was mixed with Laemmli buffer and normalized with the stain-free image acquired before transfer. MOPS/SDS running buffer was composed by 1M MOPS, 1M Tris Base, 69.3 mM SDS and 20.5 mM free acid EDTA. Transfer buffer was prepared with 25mM Tris, 192 mM glycine and 20% MtOH. Proteins were transferred to a PVDF membrane (GE Healthcare, #10600015) and incubated with 5% BSA in 1X TBST (20 mM Tris pH 7.5, 150mM NaCl, 0.1% Tween-20) for 1 hour at RT. Membranes were then incubated with anti-EMID2 (1:1000; Santa Cruz, #TA340271) or anti-TGFβ (1:1000; Abcam, #AB92486) andibodies overnight at 4°C or anti-tubulin (1:2000; Sigma, #T5168) for 1 hour at RT, followed by 1 hour incubation at RT with secondary antibodies, polyclonal goat anti-mouse IgG (H+L) horseradish peroxidase (HRP) (1:2000; Dako #P0447) or polyclonal goat anti-rabbit IgG (H+L) HRP (1:2000; Invitrogen, #31460). Western blots were developed

using SuperSignal West Dura kit (Thermoscientific, #34577). Images were acquired using Biorad ChemiDoc Touch and quantified with the ImageJ software.

2.5.3 Immunostaining

The samples were cut at 5 μm thickness for staining. Frozen slides were first fixed with zinc solution for 15 minutes. All the slides were permeabilized by incubating with 0.5% Triton in PBS at RT for 20 minutes and were then blocked with 10% horse serum in PBS containing 0.5% Triton at RT for 1 hour. Then, the slides were incubated with the primary antibody in blocking solution overnight. After washing in PBS, the slides were incubated with the secondary antibody diluted 1:500 in blocking solution at RT for 1 hour. The primary and secondary antibodies that were used are listed in Table 4. Finally, the slides were incubated for 30 minutes at RT with Hoechst solution (Invitrogen, #33342) diluted 1:5000 in PBS, and then mounted with Moviol solution.

PRIMARY ANTIBODIES (target)	COMPANY AND CODE
CD31	R&D, #af3628
COLLAGEN I	Abcam, #ab21286
ERG	Abcam, #ab92513
FIBRONECTIN	Abcam, #ab2413
Ki67	Invitrogen, #9129
LAMININ	Sigma, #L9393
F-ACTIN (Phalloidin 488)	ThermoFisher, #A12379
LECTIN (Fluorescein Lycopersicon Esculentum)	VectorLAb, #FL-1171
α-SMA-Cy3	Sigma, #C6198
SECONDARY ANTIBODIES	**COMPANY AND CODE**
Alexa Fluor™ 488 Donkey anti goat IgG (H+L)	Invitrogen, #A-11055
Alexa Fluor™ 647 Donkey anti goat IgG (H+L)	Invitrogen, #A-21447
Alexa Fluor™ 488 Donkey anti rabbit IgG (H+L)	Invitrogen, #A-21206
Alexa Fluor™ 647 Donkey anti rabbit IgG (H+L)	Invitrogen, #A-31576

Table 5. Antibodies used for immunostaining.

2.5.4 Immunohistochemistry

Hematoxylin and Eosin (H&E) staining was performed using reagents from BioOptica. Briefly, paraffin sections were deparaffinised incubating them overnight at 56 °C and then 30 minutes in xylene. Then, slides were put in X-free solvent (#21-A1305) for 5 minutes and then a scale of ethanol dilutions was applied (100%, 90%, 75% and 50%). After some minutes of washing in tap water, slides were incubated in Mayer's hematoxylin (#21-A06002) for 3 minutes, then rinsed in tap water. The tissue was then incubated with Eosin (#21-A10002) for 6 minutes and washed with tap water for some minutes. Finally, slides were subjected to 1 minute of incubation with 95% ethanol, followed by 1 minute in 100% ethanol, 3 minutes in X-free solvent and then mounted with Moviol.

2.5.5 Receptor tyrosine kinase (RTK) assay

The mouse phospho-RTK array kit (R&D, #ARY014) was used to explore tyrosine phosphorylation of mouse RTKs in HUVECs induced by BD33. HUVECs were starved for 6 hours in serum-free M199 medium supplemented with EGF, bFGF and hydrochortisone and then incubated with 200 ng/mL of mouse recombinant BD33 in M199 medium for 30 minutes at 37°C. HUVECs for the control condition were incubated with M199 alone. Then, the supernatant was removed, the cells were washed with PBS three times and the cells were lysed with Lysis Buffer 17 (provided by the kit) supplemented with 10 μg/mL aprotinin, 10 μg/mL leupeptin and 10 μg/mL pepstatin. The array membrane was blocked with Array Buffer 1 (provided by the kit) and incubated overnight with 200 μg of HUVEC lysates at 4°C on a rocking platform shaker. The day after, the membrane was washed well and incubated with 1:5000 Anti-Phospho-Tyrosine-HRP Detection Antibody in Array Buffer 2 (both provided by the kit) for 2 hours at RT shaking. Finally, membranes were washed, incubated with SuperSignal West Dura kit (Thermoscientific, #34577), and visualized using Biorad ChemiDoc Touch. Quantification was performed using the ImageJ software.

2.6 Rheology

We performed rheological analysis to test whether the recombinant EMID2, added to the Matrigel, modified the mechanical properties of the matrix. An equal amount of PBS was added to the Matrigel as control condition.

Rheological experiments were conducted on the controlled stress rheometer Haake Mars III equipped with Peltier temperature control system and using the plate–plate geometry PP20 (diameter 20 mm, gap in the interval 0.75-1.0 mm). The experiments were conducted in oscillatory mode at a fixed frequency of 1.0 Hz with controlled strain amplitude of 0.01 γ. In

all cases, 400 µL of Matrigel were applied to the measuring stage, pre-warmed and maintained at 37 °C in a humid chamber. The measurement of gelation kinetics started immediately after the application of the sample on the stage and lasted 30 minutes. For strain-stiffening measurements, a series of strains were performed and the elastic modulus (G') and the loss modulus (G'') were measured as indications of elasticity and viscosity, reciprocally, of the material. The first individual strain was performed by applying a strain from $\gamma = 0.01–1.0$. Then, 2 subsequent strains were applied from $\gamma = 0.01–10.0$ to reach network weakening and breakage.

2.7 Image acquisition and analysis

Images were acquired using 3 different microscopes and respective softwares:

- Leica fluorescence microscopy (Leica Microsystem) using LAS V4.4 software
- Nikon A1 Plus Microscope equipped with DC-152Q-C00-FI using NIS 4.30 software (Nikon).
- ZEISS LSM 880 with Airyscan

Images were analysed using the ImageJ software (Fiji).

2.8 Statistical analysis

GraphPad Prism software was used to calculate the statistical significance of the presented datas. The reported results are expressed as mean value ± standard error mean (SEM) and the number of experiments is indicated for each analysis. One-way ANOVA statistics followed by Dunnett multiple comparison test was used for multiple datasets whereas the unpaired Student's t-test was used to compare 2 groups of data. Only significant values are indicated by the asterisks above the graphs (*$p < 0.05$, **$p < 0.01$, ***$p < 0.001$, ****$p<0.0001$).

3. RESULTS

3.1 Set up of FunSel for the selection of anti-invasive factors

The FunSel approach was initially based on factor identification through multiple rounds of iterative selection (Ruozi et al., 2015) and was later modified by constructing a library of secreted factors each one specifically identified by a barcode (Bortolotti et al., 2017). The barcodes are 10 bp-long nucleotide sequences uniquely identifying each vector and determined by NGS. In this way, factor enrichment and loss following the application of a selective pressure can be determined by comparing the relative barcode frequency in the different samples.
In this project, the FunSel strategy was applied with the aim of identifying secreted proteins able to inhibit cancer cell invasion.

3.1.1 Choosing the appropriate cancer cell type to exert an efficient selective pressure

In order to establish the most appropriate model of cancer cell invasion *in vivo*, we compared the pattern of growth and expansion of four commonly used cancer cell lines injected intramuscularly into syngenic mice. We injected 50,000 B16-F10 melanoma, LLC or LG cells into the *tibialis anterior* muscle of C57BL/6 mice, and the same number of 4T1 breast cancer cells into Balb/c mice. While most of the cell types expanded forming a single tumor mass, squishing but not disrupting the surrounding muscle fibers, LLC cells exhibited an infiltrative pattern of growth, resulting in the invasion and progressive replacement of muscle fibers (Figure 7). Thus, we chose LLC cells to perform the FunSel screening with the aim of identifying secreted proteins able to inhibit the invasion of muscle fibers by these cells.

3.1.2 A powerful selection requires a specific timing

To prove the feasibility of FunSel strategy to select anti-invasive factors, a pilot experiment was performed to evaluate the time necessary for an efficient selection of the secreted factors *in vivo*.
To perform this pilot experiment, we created a pool composed by 50 randomly chosen, but similar in size, secreted proteins, including Sema3A as a positive control. Sema3A is known to inhibit cell migration of many cell types, including cancer cells, and to block angiogenesis *in vivo*, resulting in tumor growth inhibition (Gioelli et al., 2018; Zacchigna et al., 2008) A group of 8 C57BL/6 mice received bilateral intramuscular injection of the AAV pool (3×10^{10} vg per muscle) and one week later 4 mice received injection of 50,000 LLC cells in the same muscles.

Half of the animals, 2 that received both the pool and the cancer cells and 2 injected only with the pool, were sacrificed 2 days after tumor implantation whereas the other 4 mice were sacrificed at 10 days. In this way, all the groups were n=4 muscles. After DNA extraction from muscle tissues, the barcode sequences were amplified by PCR and quantified by NGS. We evaluated the enrichment of each factor after cancer cell injection as an indication of its anti-invasive activity. To compare the enrichment frequencies of transgenes, we considered the ratio between the logarithm of the relative enrichment of each muscle subjected to the selection by cancer cells and the mean of the logarithms of the relative enrichment of control muscles. The numeric values are reported in Table 3. For a factor that did not undergo any selection, meaning that it was neither positive nor negative in influencing cell invasion, the expected value was 0. The graph in Figure 7I reports the log value of the relative frequency of transgenes after 2 days of selection, whereas the graph in Figure 7J shows the enrichment at 10 days. The flatness of the frequency curve at 2 days reflects its standard deviation (SD), definitely narrower compared to the one detected at 10 days (0.07 and 0.19, respectively). At 2 days, 9 factors had a recovered frequency >1SD, with a maximal enrichment of 0.20. At 10 days, when cancer cells had invaded a higher portion of the muscles, 5 factors resulted enriched over the same threshold, also including the positive control Sema3A, which showed a log enrichment of 0.41 (Figure 7I-K). Thus, we decided to perform the FunSel selection over a period of 10 days.

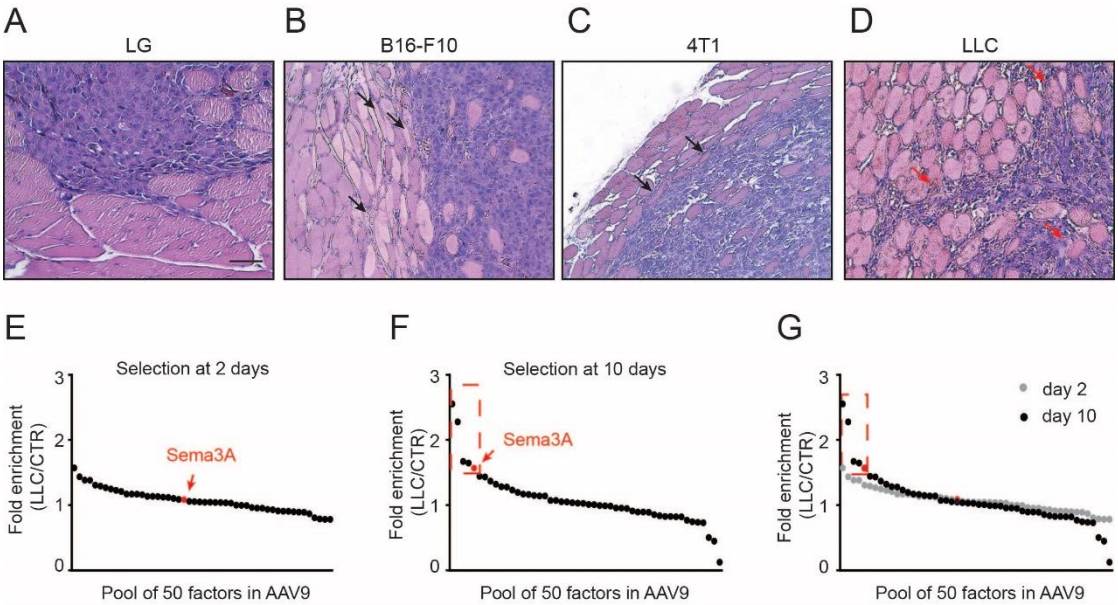

Figure 7. Optimization of the FunSel strategy for the selection of anti-invasive factors. *Hematoxilin and Eosin staining showing the pattern of invasion of the tibialis anterior muscle injected with different cancer cell types, namely LG (A), B16-F10 (B), 4T1 (C), and LLC cells (D). Black arrows indicate squeezed muscle fibers; red arrows indicate muscle fiber invasion by LLC cells. Scale bar is 100 μm. (I-K) Graphs reporting the relative enrichment of each transgene of the pilot pool of 50 AAV9 used to determine the best time for an efficient selection of anti-invasive factors. We compared mice injected intramuscularly only with the pool (CTR) or with both the pool and LLC cells (LLC) and sacrificed at 2 (I) or 10 (J) days after cancer cell injection. Sema3A (red dot in I, J and K) was inserted as a positive control and resulted enriched, together with other factors, at 10 but not at 2 days after tumor cell injection.*

Table 6. Relative enrichment of factors in the pilot pool of AAV9 at 2 or 10 days after LLC cell injection. *In red, the factors that resulted enriched at 10 days.*

Pilot Pool 50 AAV9	LOG (LLC/CTR)	
Transgene	**Day2**	**Day 10**
Cp	0.14	0.41
Olfml2b	0.11	0.36
Emilin2	-0.11	0.22
Man2b2	0.02	0.22
Sema3a	0.04	0.20
Spink5	-0.10	0.16
AK053037	-0.11	0.16
Morc2a	0.05	0.14
Furin	0.08	0.12
Adamts16	0.10	0.11
Itih1	0.07	0.11
Loxl3	-0.04	0.09
Adamtsl2	0.02	0.08
Hhipl1	0.02	0.07
Lepr	0.10	0.07
Eln	0.07	0.06
C2	0.16	0.06
Cfb	-0.02	0.06
Ace2	0.05	0.03
Bcan	0.04	0.03
St14	0.06	0.02
Heg1	0.09	0.02
Comp	-0.06	0.02
Cpxm2	-0.02	0.01
Sema3f	0.02	0.01
Postn	0.00	0.00
Pcsk1	-0.04	0.00
Plg	-0.04	0.00
Emilin1	-0.09	0.00
Dpp4	0.02	-0.01
Sema3c	0.00	-0.02
Fstl5	0.07	-0.02
C6	0.14	-0.02
Spon1	0.02	-0.04
Matn2	-0.03	-0.05
Adamts15	0.20	-0.05
BC046331	0.02	-0.05
Qsox1	0.00	-0.07
Lepre1	-0.05	-0.08
Vwa5a	-0.02	-0.08
Gsn	-0.05	-0.08
Itih3	0.04	-0.09
Svs1	-0.03	-0.09
Prss12	-0.05	-0.11
Adamts4	0.02	-0.13
Nell2	0.05	-0.13
Dag1	0.12	-0.14
Thbs3	0.07	-0.30
Ephb6	0.01	-0.35
Egflam	0.05	-0.90

3.2 FunSel provided a selection of secreted factors

After having obtained a proof of feasibility with the pilot pool, we injected all 24 pools of AAV9 vectors, each one containing an equimolar amount of 50 different secreted transgenes, bilaterally into the *tibialis anterior* muscle of 3 month-old C57BL/6 mice (3 x 10^{10} viral genomes per muscle, 5 animals per pool). After 7 days, a time sufficient to drive robust transgene expression by AAV vectors, 3 animals per pool were injected into the same muscles with 50,000 LLC cells and sacrificed after additional 10 days. All the treated muscles were harvested for DNA extraction and viral genome amplification. Each transgene was identified by a specific 10 bp-barcode that was amplified by a validated two-step PCR protocol (Bortolotti et al., 2017). The amplicons were finally analyzed by NGS using an Illumina Hiseq platform to identify the relative abundance of each barcode in the different experimental conditions and thus of each transgene. A schematic of the experimental flow chart and rationale of the approach is shown in Figure 8A.

To verify that all the AAV vector plasmids underwent an efficient packaging and were present in an equimolar amount in the final AAV vector pool, we first sequenced the input viral lysate of each pool and compared the recovered reads with the barcode reads recovered from transduced muscles. In this way, we could distinguish the factors that were lost after cancer cell selection from factors that were not detected due to unsuccessful packaging, and exclude the latter from the analysis. In parallel, the comparison between the barcode frequencies of the input viral lysate with the transduced muscles allowed us to evaluate the level of selection occurring upon muscle cell transduction in the absence of cancer cell injection (Figure 8B).

Then, to ensure the reliability of the barcode frequencies recovered by sequencing, we analyzed the percentage of reads identifying the barcodes over the total reads obtained after sequencing of each sample (Figure 8C). As reported in Figure 8B for a representative pool, the purity of the barcode reads recovered from each transduced muscle was always higher than 90%. When this was not the case, the sample was excluded from the analysis and its amplification and sequencing was repeated (an example is shown in Figure 8C, in red). In total, 3 out of 24 pools had to be excluded from the final ranking due to excessive variability in the results, namely pools 3, 16 and 24.

In this experimental system, cancer cells are expected to invade and progressively eliminate the surrounding muscle fibers, each one containing a few AAV genomes. If one of the transgenes inhibits the invasion by cancer cells, the producing muscle fiber should be protected and have a higher chance to survive compared to a fiber producing factors that either enhance or do not change the invasiveness of cancer cells. Thus, the AAV genomes within the muscle fibers that resist cancer cell invasion are expected to be enriched for transgenes encoding for protective proteins. To detect the factors carrying possible anti-invasive properties, we compared the

relative abundance of transgenes detected in the transduced muscle in presence of cancer cells with the one of muscles that received only the pool of AAV vectors.

As for the pilot pool, we compared the frequency of transgenes expressed as the ratio between the logarithm of the relative transgene abundance in the muscles subjected to the selection by cancer cells and the mean of the logarithms of the relative enrichment of the transgenes in control transduced muscles. Factors that do not influence cell invasion are expected to present a log value around 0 (grey zone in Figure 8D), whereas an enrichment >1SD is considered significant, possibly indicating anti-invasive function of the corresponding protein (red zone in Figure 8D).

Figure 9 shows the results of the screening of 21 pools, overall containing 1051 factors. We excluded 22 factors, reported in orange, due to non-detectable number of reads both in the treated muscles and in the viral lysate, suggesting a poor encapsidation of the corresponding plasmid. Furthermore, a few factors (reported in blue and identified by blue arrows in Figure 9) were not detected in some samples, but they were however kept as we had at least 3 replicates. In total, 1029 factors have been used to build the final ranking, considering the logarithmic fold enrichment of each transgene (Figure 10). The average logarithmic value of the ranked factors was -0.15±0.40 and identified 60 enriched proteins with an enrichment higher than 1SD.

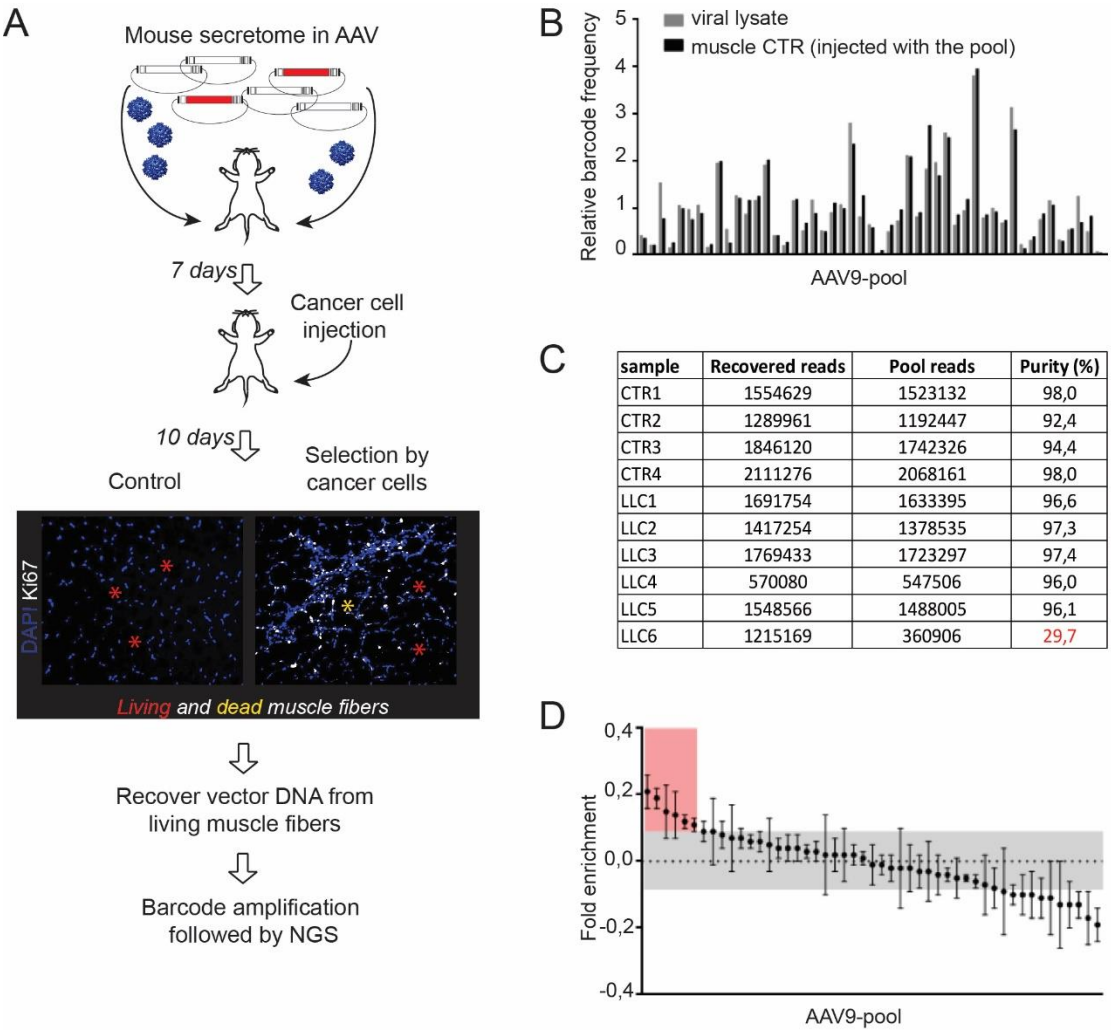

sample	Recovered reads	Pool reads	Purity (%)
CTR1	1554629	1523132	98,0
CTR2	1289961	1192447	92,4
CTR3	1846120	1742326	94,4
CTR4	2111276	2068161	98,0
LLC1	1691754	1633395	96,6
LLC2	1417254	1378535	97,3
LLC3	1769433	1723297	97,4
LLC4	570080	547506	96,0
LLC5	1548566	1488005	96,1
LLC6	1215169	360906	29,7

Figure 8. FunSel for the selection of anti-invasive factors. *(A) Schematic flow chart of the screening. The secretome library was injected in the tibialis anterior of adult C57BL/6 mice as pools of AAV9 carrying transgenes uniquely recognized by barcodes. After 7 days 50,000 LLC cells were administered to the same muscles to drive the selection of transgenes with anti-invasive properties, expected to be enriched in the surviving muscle fibers. The DNA was isolated from muscles after 10 additional days and the barcodes were amplified by a 2-step PCR. NGS was used to quantify transgene abundance in all samples. (B) The amount of barcodes recovered from the muscle injected with the pool was compared with the barcode abundancy in the input viral lysate. (C) The percentage of barcode recovery over the total reads was used to exclude inappropriate samples (in red. as an example). (D) Example of the analysis of single pools. The frequency of transgenes was expressed as the ratio between the log of each transgene in the muscles injected by cancer cells and the mean of the log values of transgenes in control muscles. Factors contained in the pool are listed in x-axis; the fold enrichment is shown in y-axis. The red area corresponds to factors that had a barcode frequency >1SD.*

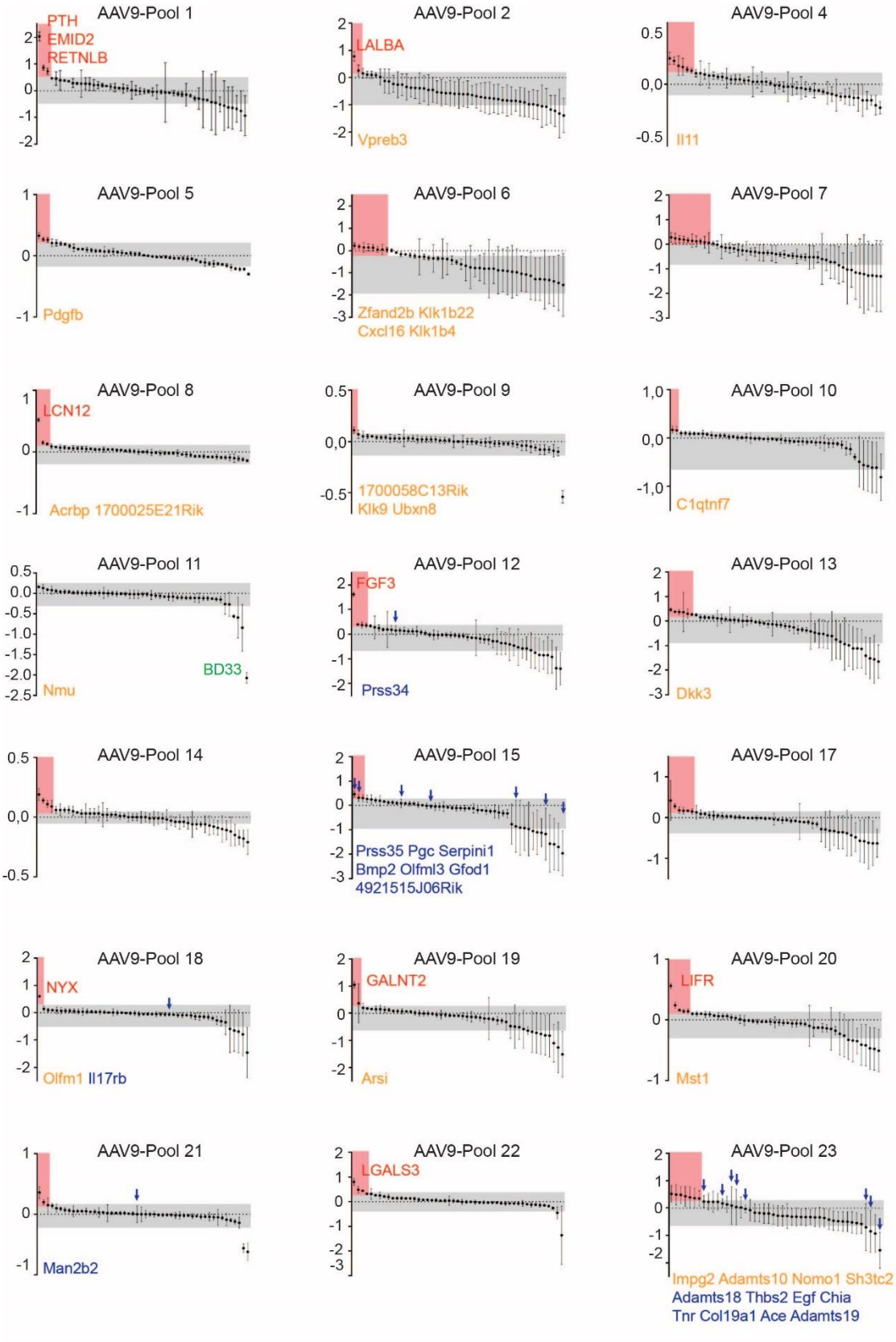
AAV9-Pool 1
PTH
EMID2
RETNLB
AAV9-Pool 2
LALBA
Vpreb3
AAV9-Pool 4
Il11
AAV9-Pool 5
Pdgfb
AAV9-Pool 6
Zfand2b Klk1b22
Cxcl16 Klk1b4
AAV9-Pool 7
AAV9-Pool 8
LCN12
Acrbp 1700025E21Rik
AAV9-Pool 9
1700058C13Rik
Klk9 Ubxn8
AAV9-Pool 10
C1qtnf7
AAV9-Pool 11
BD33
Nmu
AAV9-Pool 12
FGF3
Prss34
AAV9-Pool 13
Dkk3
AAV9-Pool 14
AAV9-Pool 15
Prss35 Pgc Serpini1
Bmp2 Olfml3 Gfod1
4921515J06Rik
AAV9-Pool 17
AAV9-Pool 18
NYX
Olfm1 Il17rb
AAV9-Pool 19
GALNT2
Arsi
AAV9-Pool 20
LIFR
Mst1
AAV9-Pool 21
Man2b2
AAV9-Pool 22
LGALS3
AAV9-Pool 23
Impg2 Adamts10 Nomo1 Sh3tc2
Adamts18 Thbs2 Egf Chia
Tnr Col19a1 Ace Adamts19

Figure 9. Screened single pools. *The graphs represent the result of the in vivo screening of the 21 pools, each one containing 50 AAV vectors codifying for secreted proteins. The factors in each pool are represented in the x-axis whereas the fold enrichment in the y-axis. The factors with a barcode frequency >1SD are highlighted by the red area, whereas non-selected factors are included in the grey area. The 10 top-hit factors of the final ranking are identified in red. The factors that were not detected either after the selection in the muscle or in the input viral lysate were excluded from the analysis and are indicated in orange under each graph, whereas the factors that were missing in a few samples are indicated in blue. BD33 is also indicated as the factors with the highest barcode loss (green).*

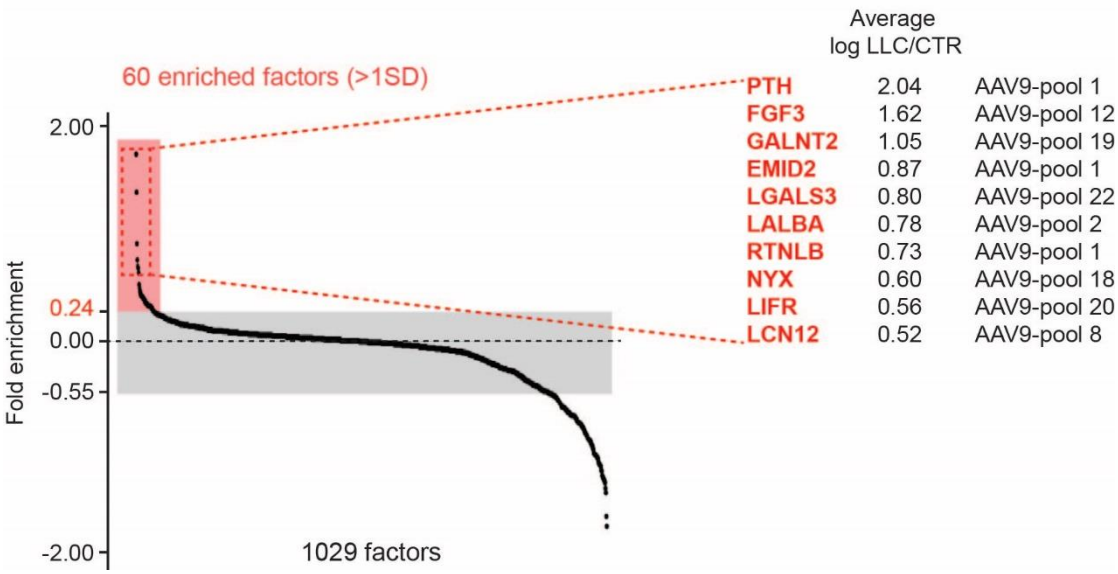

Figure 10. The final ranking of the secreted factors after FunSel. *(A) The graph represents the final ranking including 1029 factors of the secretome library (in x-axis) that were ranked together according to log values. indicated in the y-axis. The red zone identifies the 60 secreted factors that presented an enrichment >1SD. The grey area delimited the non-selected factors (log value around 0).*

3.2.1 Validation of the 10 top hits inhibiting cell migration

We decided to validate the capacity of the 10 top proteins of the final ranking to inhibit cell invasion using two common migration assays *in vitro*, namely the transwell chamber and the wound healing.

To produce serum-free media containing high levels of the 10 secreted factors, HEK-293T cells were transfected with the corresponding plasmids. We performed the transwell migration assay using two different cell types, either the same cancer cells used for the screening (LLC) and an immortalized endothelial cell line (iMAEC). The cells were seeded on the top of the membrane in FBS-free medium, while the serum-free supernatant containing each factor was added to the lower compartment. As shown by the representative images in Figure 11A and the quantification in Figure 11B, five factors, namely PTH, FGF3, EMID2, GALNT2 and LCN12, significantly reduced LLC cell migration and four of them, PTH, FGF3, EMID2 and LCN12, potently inhibited cancer cell migration even when FBS was added to the supernatant (Figure 11C). The same four factors significantly inhibited also iMAEC cell migration both in the absence (Figure 11D) and in the presence of FBS (Figure 11E).

The same 10 top hits were also tested in the wound healing assay using iMAECs. As shown by the representative images in Figure 11F and the quantifications in Figure 11 G-H, PTH, FGF3 and LCN12 showed a trend in reducing cell migration both in absence and in presence of FBS, but only EMID2 reached statistical significance.

Figure 11. FunSel identified anti-invasive secreted factors. *(A) Representative images of transwell migration assay performed with LLC and iMAEC cells, both in the presence and in the absence of FBS. Cell nuclei were stained with DAPI. (B-C) Quantification of LLC cell migration toward HEK-293T supernatant containing the 10 top-hit proteins in the absence (B) or in the presence (C) of FBS. (D, E) Quantification of iMAEC migration. (F) Representative images of wound healing assay performed with iMAEC incubated with the supernatants containing the factors that most efficiently reduced cell migration in the trasnwell assay. (H) Quantification of the distance covered by the cells in response to the 10 top factors either in absence (G) or in presence (H) of FBS. Values in B, C, D, E, H and I are expressed as mean ± SEM. *p < 0.05, **p < 0.01, ***p < 0.001 by one-way ANOVA followed by Dunnett multiple comparison test. Scale bar in F is 50 µm. Scale bar in G is 200 µm.*

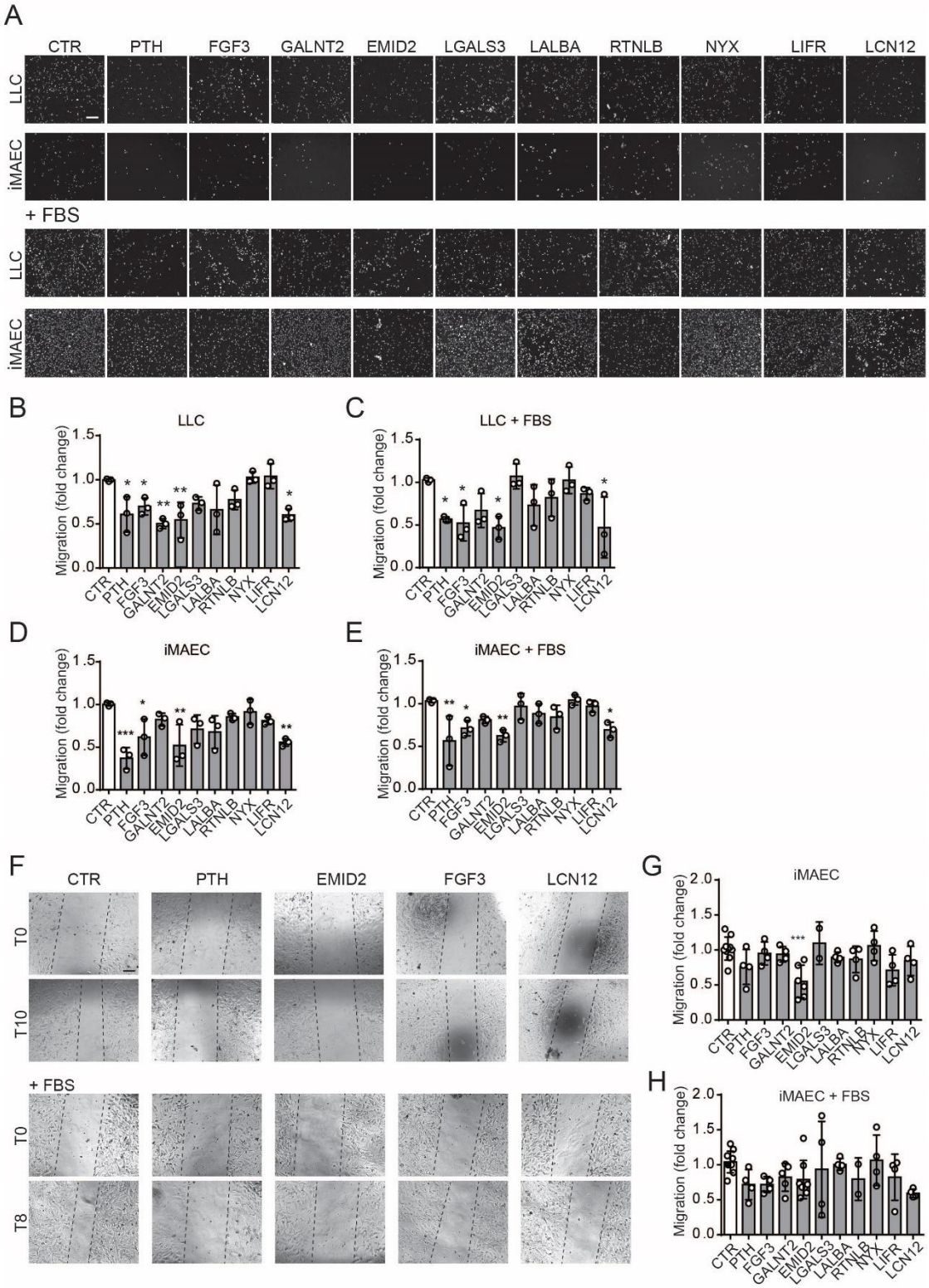
A
CTR
PTH
FGF3
GALNT2
EMID2
LGALS3
LALBA
RTNLB
NYX
LIFR
LCN12
LLC
iMAEC
+ FBS
B
LLC
C
LLC + FBS
D
iMAEC
E
iMAEC + FBS
Migration (fold change)
F
T0
T10
T8
G
iMAEC
H
iMAEC + FBS

3.2.2 EMID2 was the best factor inhibiting cancer cell growth *in vivo*

We then decided to test the four factors that more efficiently blocked cell migration *in vitro* (PTH, FGF3, EMID2 and LCN12) for their effect on cancer growth *in vivo*. We produced the corresponding AAV9 vectors for their individual overexpression and injected them, together with 50,000 LLC cells, in the *tibialis anterior* muscle of adult C57BL/6 mice (1.5×10^{10} viral genomes per mouse, 3 animals per factor). As an index of tumor size and growth capacity, we measured both nuclear density and proliferation. As shown by the representative images in Figure 12A and the quantification in Figure 12B, the overexpression of EMID2 by AAV9 significantly reduced cancer cell growth compared to the control. This was also confirmed by the quantification of $Ki67^{+}$ cells, significantly reduced in AAV9-EMID2 injected muscle compared to control (Figure 12C).

To further confirm the effect of EMID2 in reducing cancer growth *in vivo*, we repeated the experiment using a different cell type, LG cells, that tend to growth forming a more compact mass, easier to quantify, compared to LLC cells. We injected either AAV9-EMID2 or AA9-CTR together with 50,000 LG cells in the *tibialis anterior* muscle of adult C57BL/6 mice (1.5×10^{10} viral genomes per muscle, 6 per group). Representative whole-muscle images in Figure 12E clearly show a significant reduction in LG tumor size, identified by the green line, when EMID2 was overexpressed (Figure 12D).

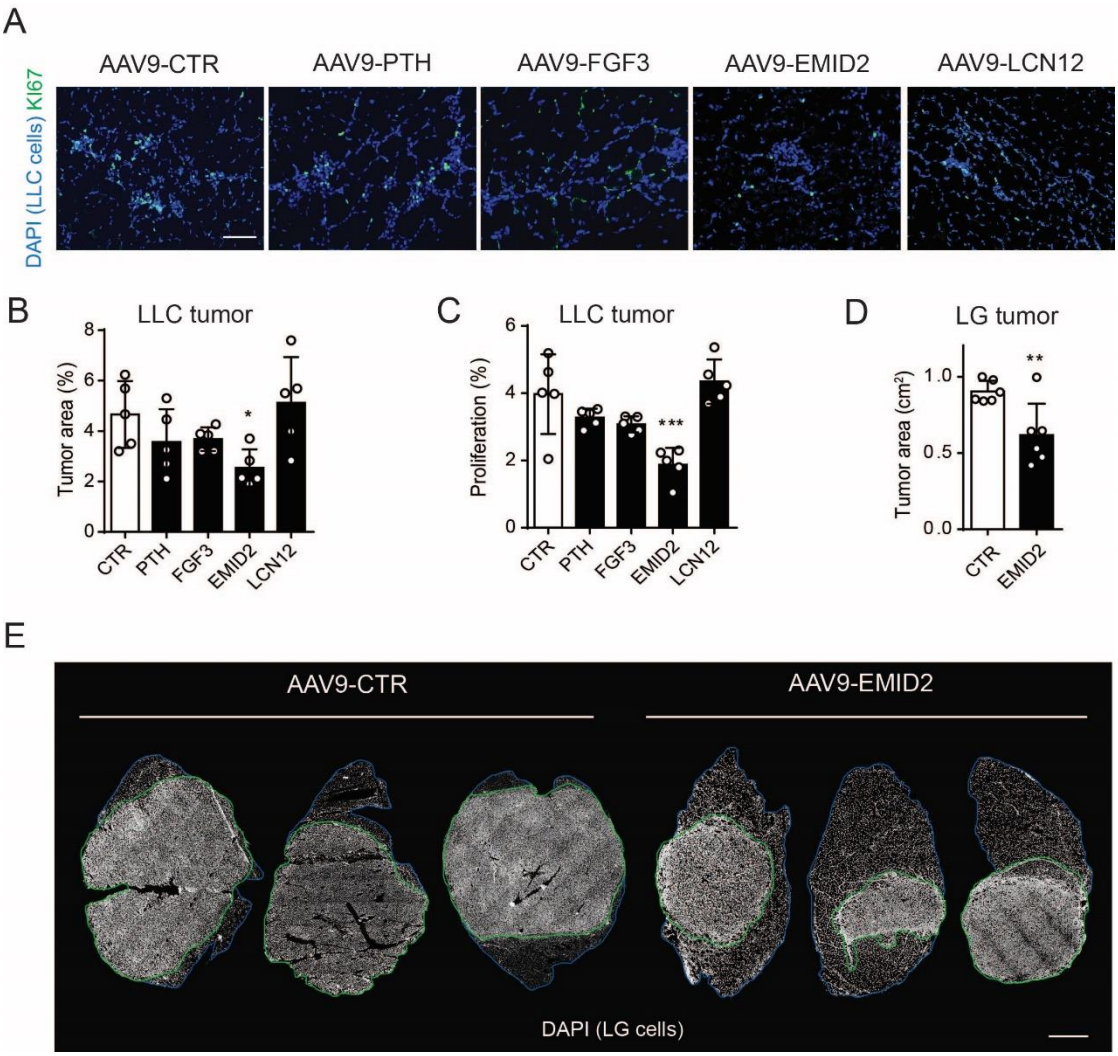

Figure 12. EMID2 reduced tumor growth in vivo. *(A) Representative images of LLC tumor cells co-injected with AAV9-CTR, AAV9-PTH, AAV9-FGF3, AAV9-EMID2 or AAV9-LCN12 in the tibialis anterior muscle. DAPI in blue, Ki67 in green. (B) Quantification of the area covered by tumor cells, identified by DAPI nuclear staining. Quantification of the tumor size was made by calculating the percentage of muscle area covered by high blue intensity on the total area, using ImageJ software. (C) Quantification of the percentage of proliferating cells in the tumor. (D) Quantification of the size of LG-tumors, by measuring the area covered by higher blue signal density. (E) Representative whole-tissue sections of tibialis anterior muscles injected with LG cells together with AAV9-CTR or AAV9-EMID2. The green line indicates the tumor mass, whereas the blue line indicated the normal muscle. All the measurements were performed by quantifying the tumor size in 4 sections per muscle, representative of the thickness of the muscle. Values in B, C and D are expressed as mean ± SEM. *p < 0.05, **p < 0.01, ***p < 0.001 by one-way ANOVA followed by Dunnett multiple comparison test (B, C) or unpaired Student's t test (D). Scale bar in A is 200 µm. Scale bar in E is 0.2 cm.*

3.3 Direct effect of the recombinant EMID2 on cell migration

In order to prove that EMID2 was responsible for the observed effects, we wanted to test whether the mouse recombinant protein was able to reproduce the same results. By Western blot, we could detect two bands (first lane, Figure 13C), at 47 kDa and at 57 kDa respectively, as indicated in the datasheet of the recombinant protein. In contrast, the supernatant collected from HEK-293T cells transfected with pGi-EMID2 showed only one band at 57 kDa (second lane, Figure 13C).

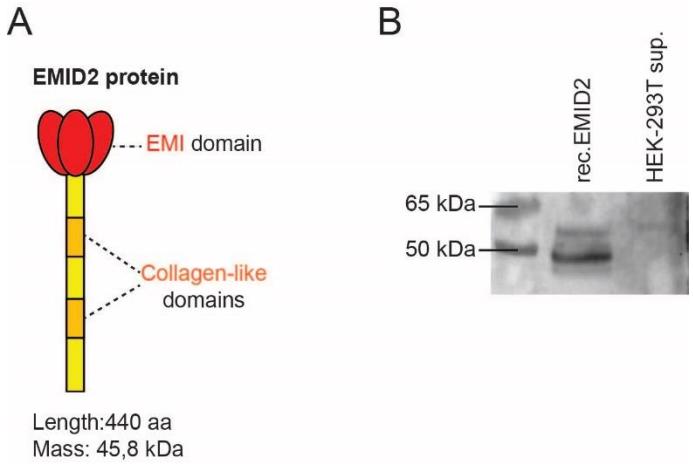

Figure13. Structure of EMID2 protein. *(A) The EMID2 protein is composed by an EMI domain (in red) and two collagen-like domains (in orange). (B) Western blot of mouse recombinant EMID2 showing two bands, at 47 kDa and 57 kDa, and the supernatant from HEK-293T overexpressing mouse EMID2 and showing one band at 57 kDa.*

3.3.1 Recombinant EMID2 blocked tumor cell migration *in vitro*

To validate the effect of EMID2 *in vitro*, we tested the recombinant EMID2 in the wound healing assay based on IBIDI chambers using multiple cell types. To avoid biases due to a possible effect of EMID2 on cell proliferation, we starved the cells for 6 hours prior to assessing their migration. Cells were seeded in both wells of the IBIDI support and allowed to reach confluence. After removing the separator, the recombinant protein was added to the culture medium and cell migration was monitored until the closure of the gap.

All the tumor cell lines tested in this experiment (lung cancer LLC and LG cells, and B16-F10 melanoma cancer cells) migrated at a significantly lower speed when recombinant EMID2 was added to the culture medium (Figure 14A-C). As shown by the representative images, the

inhibitory effect on cell migration followed a concentration-dependent trend, with the highest effect at 10 μg/mL (Figure 14A-C).

Then, we tested whether recombinant EMID2 was also able to block the migration of normal, not neoplastic cells, namely primary liver fibroblasts, in the same wound healing assay. As shown in Figure 14D, control fibroblasts fully closed the gap at 20 hours, whereas fibroblasts incubated with EMID2 migrated significantly less and the gap was still present also at the lowest concentration of the protein. As expected. EMID2 was more effective in primary fibroblasts than in cancer cells, as primary cells are normally more responsive to exogenous stimuli than immortalized cell lines.

Figure 14. Recombinant EMID2 inhibited cell migration in the wound healing assay. *Representative images and relative quantification of the wound closure showing that the recombinant EMID2 decreased the migration of tumor cells, LLC (A), LG (B) and B16-F10 (C) at the indicated concentrations. (D) Representative images and quantification of primary fibroblast migration with recombinant EMID2 at the indicated concentrations. Values in the graphs are expressed as mean ± SEM. *p < 0.05, **p < 0.01, ***p < 0.001 by one-way ANOVA followed by Dunnett multiple comparison test. Scale bar is 100 μm.*

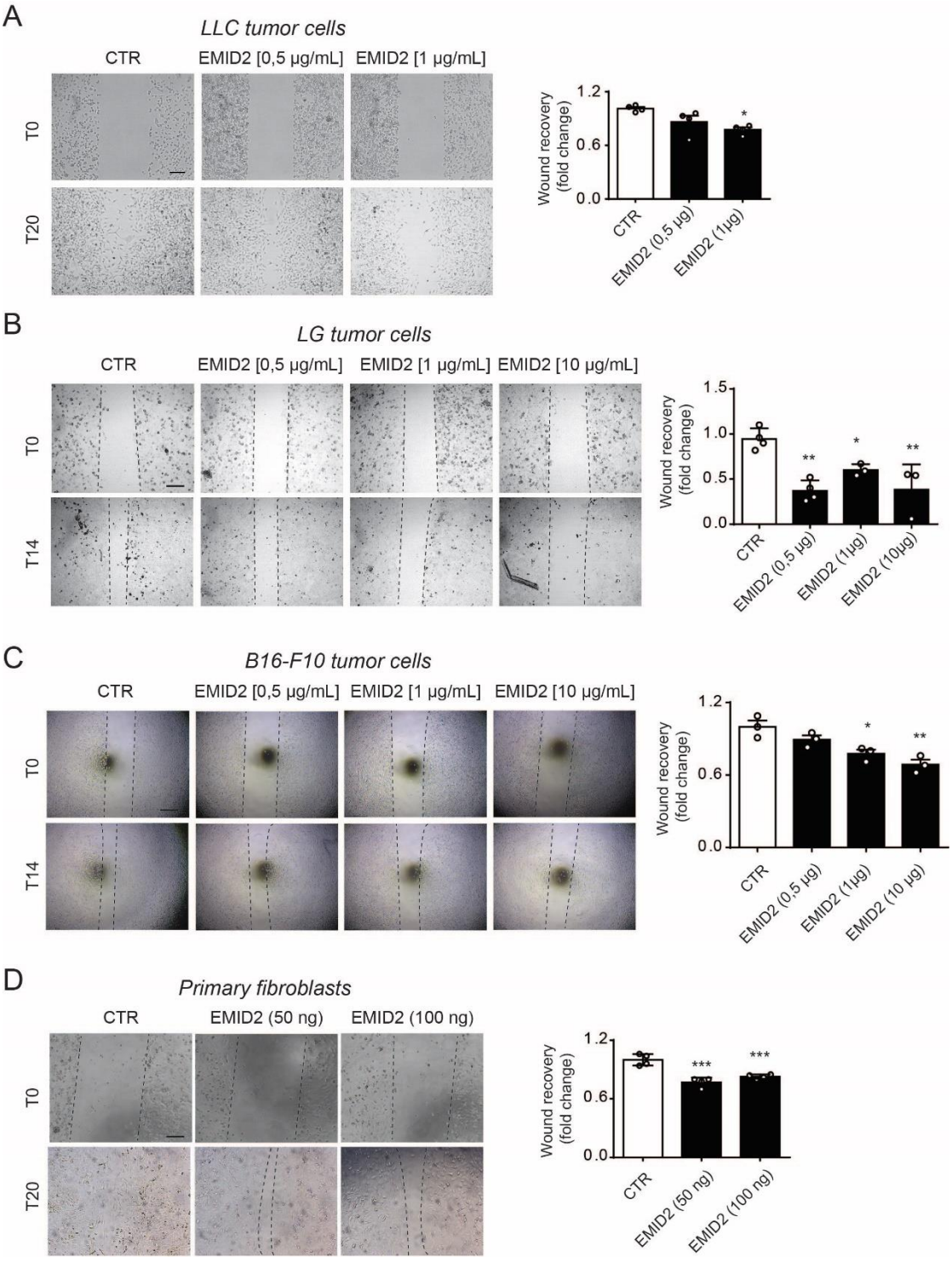
A
LLC tumor cells
CTR
EMID2 [0,5 µg/mL]
EMID2 [1 µg/mL]
T0
T20
Wound recovery (fold change)
1.2
0.6
0.0
*
CTR
EMID2 (0,5 µg)
EMID2 (1µg)
B
LG tumor cells
CTR
EMID2 [0,5 µg/mL]
EMID2 [1 µg/mL]
EMID2 [10 µg/mL]
T0
T14
Wound recovery (fold change)
1.5
1.0
0.5
0.0
**
*
**
CTR
EMID2 (0,5 µg)
EMID2 (1µg)
EMID2 (10µg)
C
B16-F10 tumor cells
CTR
EMID2 [0,5 µg/mL]
EMID2 [1 µg/mL]
EMID2 [10 µg/mL]
T0
T14
Wound recovery (fold change)
1.2
0.6
0.0
*
**
CTR
EMID2 (0,5 µg)
EMID2 (1µg)
EMID2 (10 µg)
D
Primary fibroblasts
CTR
EMID2 (50 ng)
EMID2 (100 ng)
T0
T20
Wound recovery (fold change)
1.2
0.6
0.0
***
***
CTR
EMID2 (50 ng)
EMID2 (100 ng)

3.4 EMID2 modulates angiogenesis

3.4.1 Tumors were less vascularized in presence of EMID2

Since tumor growth strictly depends on its vascularization, we assessed whether the capacity of EMID2 to reduce tumor growth was paralleled by any changes in tumor vessels. Thus, we stained tumor vessels with antibodies targeting CD31, a marker of endothelial cells, in the tumors developed in the *tibialis anterior* following the intramuscular injection of LG cancer cells together with AAV9-EMID2 or AAV9-CTR, and previously described in the paragraph 13.2.2 and in Figure 12E. As shown by the representative images in Figure 15A and the respective quantification in Figure 15B, CD31 positivity in tumors growing in EMID2-overexpressing muscles was significantly decreased compared to control muscles. This suggested that EMID2 inhibited tumor-associated angiogenesis.

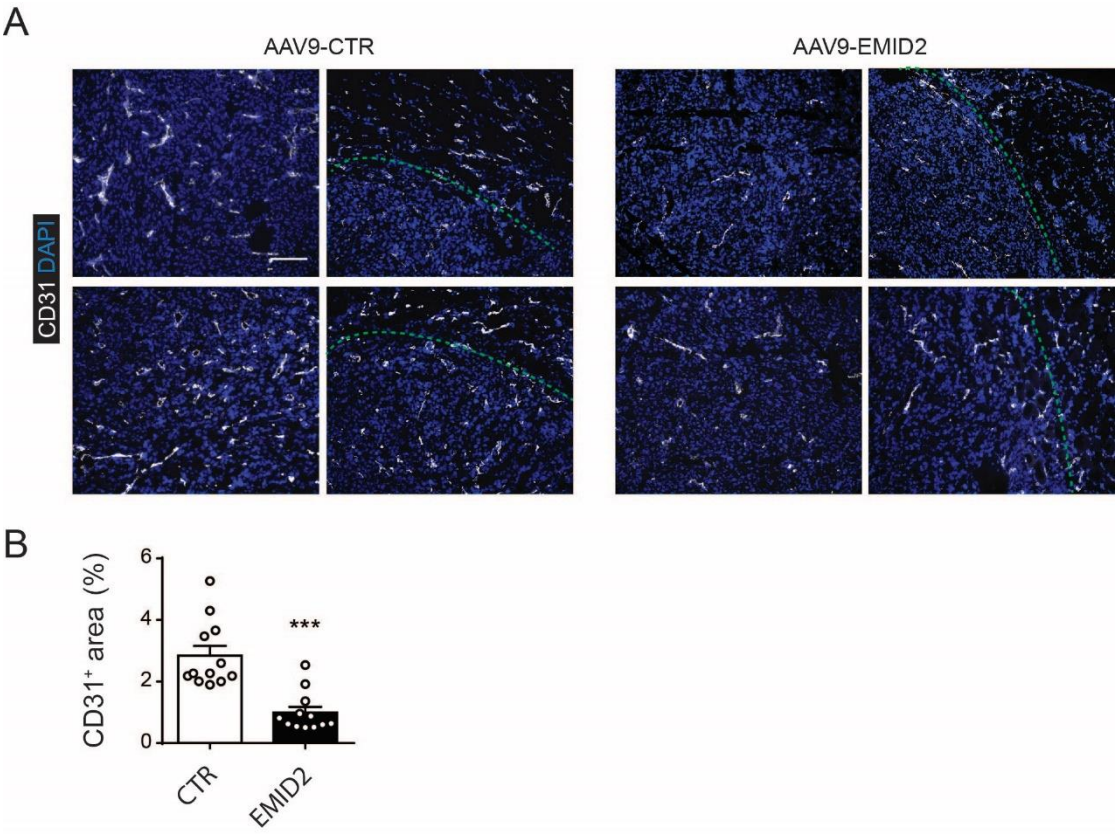

Figure 15. Tumors overexpressing EMID2 were less vascularized. *(A) Representative images of tibialis anterior muscles injected with AAV9-CTR or AAV9-EMID2 together with LG cancer cells and sacrificed after 10 days. DAPI in blue, CD31 in white. In each group, the left panels show the centre of the tumor, whereas the right panels correspond to the healthy tissue at the border of the tumor. (B) Percentage of CD31 positive area in the tumor area (6 animals per group; 2 images per animal were quantified). Values are expressed as mean ± SEM. ***p < 0.001 by unpaired Student's t test.*

3.4.2 EMID2 inhibited angiogenesis *in vivo*

As AAV9-EMID2 was able to reduce the vasculature in ectopically implanted tumors, we wanted to investigate whether the same vector also interfered with the development of the normal muscular vasculature in neonatal mice. Thus, neonatal C57BL/6 mice were injected intraperitoneally at P0 with AAV9-EMID2 or AAV9-CTR (2×10^{10} viral genomes, 3 animals per condition), followed by the harvesting of their *tibialis anterior* muscles at 4 weeks after treatment. Tissue sections were stained with three vascular markers routinely used in our laboratory, to evaluate the effect of EMID2 on physiological developmental angiogenesis. Lectin is generally used to stain the vasculature, whereas antibodies that bind CD31 specifically identify endothelial cells. Arteries are recognized by using α-SMA antibody, that binds to smooth muscle cells on the arterial wall.

As shown by the representative images in Figure 16A, when overexpressed in pups, EMID2 significantly reduced CD31 positivity in all muscles (Figure 16B). A similar trend, albeit not significant, was observed upon lectin staining (Figure 16C).

Subsequently, neonatal C57BL/6 mice were injected intraperitoneally at P0 with AAV9-EMID2 or AAV9-CTR, as above, and, after 2 weeks, they received intramuscular injection of AAV2-VEGF or AAV2-CTR (3×10^{10} viral genomes per muscle, n=3), to assess whether EMID2 was able to block the pro-angiogenic effect of VEGF. In both AAV9-CTR-injected muscles and muscles treated with AAV9-EMID2, we could recognize the recruitment of Nrp1-expressing monocytes following VEGF injection (Zacchigna et al., 2008), but the expression of EMID2 potently decreased vessel density in that area, abolishing the pro-angiogenic effect of VEGF (Figure 16D). Indeed, both $CD31^+$ area (Figure 16E) and lectin area (Figure 16F) were significantly reduced in muscles that expressed EMID2 in addition to VEGF.

We also quantified the number of $\alpha\text{-SMA}^+$ arteries and observed a significant reduction in the muscles injected with both AAV9-EMID2 and AAV2-VEGF compared to those that received only AAV2-VEGF, again supporting the anti-angiogenic effect of EMID2 (Figure 16G-H).

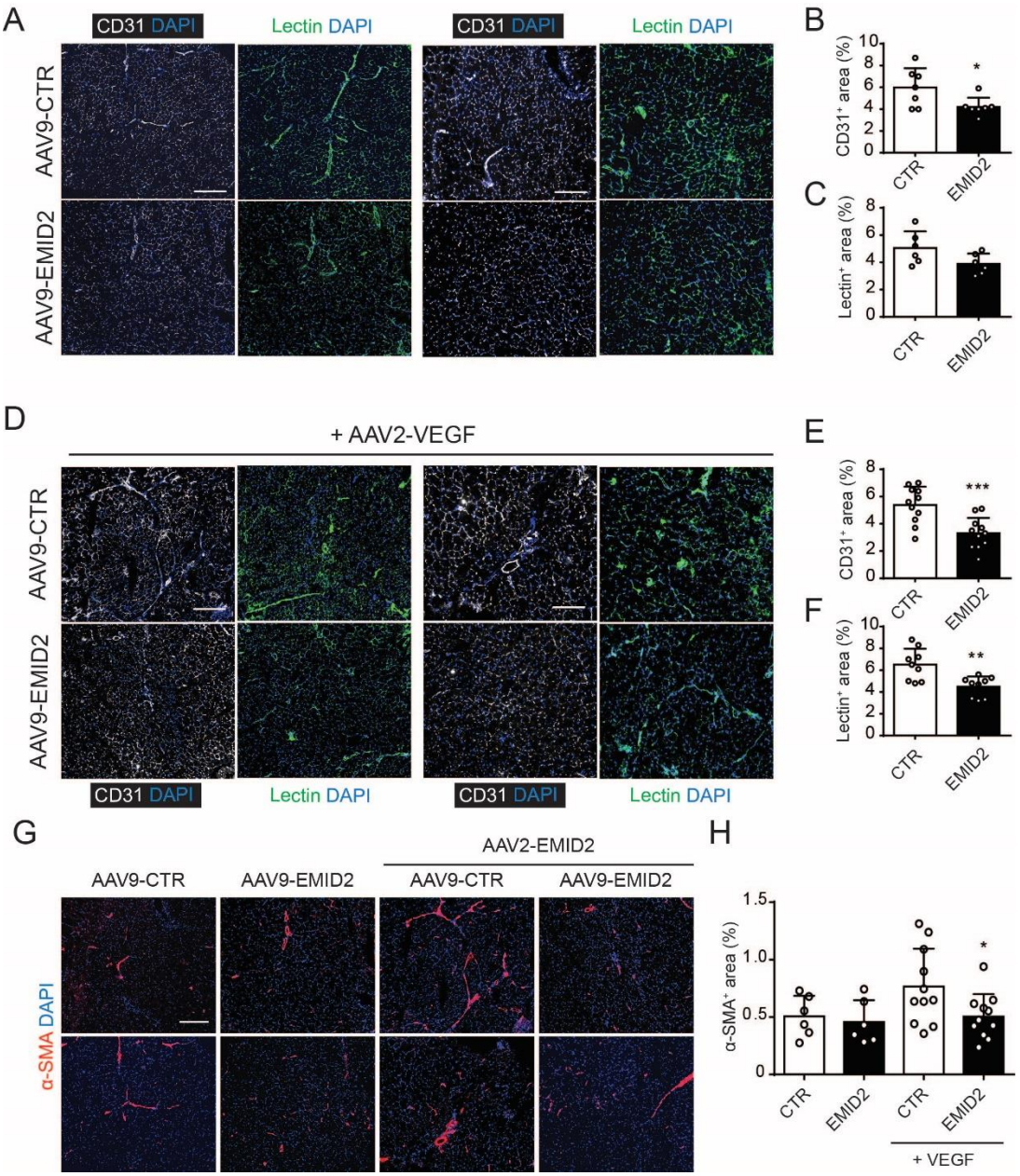

Figure 16. EMID2 inhibited angiogenesis in vivo. *Representative images of the tibialis anterior muscle of C57BL/6 mice injected with AAV9-CTR or AAV9-EMID2 intraperitoneally at birth and sacrificed at 1 month. CD31 in white, DAPI in blue, lectin in green. (B) Quantification of the area covered by CD31 staining and (C) lectin. (D) Representative images of tibialis anterior muscles of C57BL/6 mice injected with AAV9-CTR or AAV9-EMID2 intraperitoneally at birth and intramuscularly with AAV2-VEGF at 2 weeks and sacrificed at 1 month. CD31 in white, DAPI in blue, lectin in green. (E) Quantification of the area covered by CD31 staining and (F) lectin. (G) Images of tibialis anterior muscles that received AAV9-CTR or AAV9-EMID2 intraperitoneally with or without further intramuscular administration of AAV2-VEGF and respective quantification of α-SMA$^+$ area in the muscle (H). Values in B, C, E, F, H are expressed as mean ± SEM. *p < 0.05, **p < 0.01, ***p < 0.001 by unpaired Student's t test (B, C, E, F) or one-way ANOVA followed by Dunnett multiple comparison test*

(H). Scale bar is 100 μm in the left panel in A and D; 200 μm in the right panel in A and in D; 200 μm in G.

3.4.3 EMID2 inhibited angiogenesis *in vitro*

To confirm the anti-angiogenic effect of EMID2, we performed a tube formation assay using both HUVECs and primary endothelial cells. Endothelial cells are known to elongate and spontaneously form vessel-like structures when cultured on a Matrigel coating. In this assay, angiogenesis can be quantified by multiple parameters, including: i) the area covered by cells organized in a net-like structure ("covered area"), ii) the number of meshes of the net, iii) the number of "branches" starting from common points of origin called "nodes" and, finally, (iv) the number of nodes defined as knots that give rise to a minimum of 3 branches.

HUVECs were seeded in IBIDI chambers, coated with concentrated Matrigel, and cultured in a growth factor-depleted medium to reduce cell proliferation and foster tube formation. The recombinant protein was directly added to the supernatant at different concentrations, as schematically shown in Figure 17A. After a few hours, HUVECs formed a well-organized net of tubes in response to VEGF, which was added as a positive control (Figure 17B). EMID2 slightly inhibited the formation of vessel-like structures compared to the control, namely HUVEC incubated with normal medium, reaching statistical significance only for the number of nodes and tubes at the highest concentration (Figure 17B-C). As EMID2 belongs to a family of membrane proteins, we also wanted to test the effect of the protein, when embedded in the matrix instead than added to the culture medium. Thus, we repeated the assay by adding the recombinant protein directly to the Matrigel at different concentrations, as schematically shown in Figure 17D. The control condition was represented by HUVEC cells cultured on concentrated Matrigel. After Matrigel polymerization, HUVECs were seeded on the Matrigel coating and the experiment was performed as reported above. The cells quickly attached and started forming tubes that were well-organized and in a net-like structure, as shown in Figure 17E. The presence of EMID2 in the matrix significantly reduced the length of the tubes, the meshes and the area covered by organized structures at all the concentrations tested, and dramatically suppressed the formation of any vascular-like structure at the highest concentration (20 μg/mL), resulting in a marked reduction in number of tubes (Figure 17F).

The same assay was also performed with primary endothelial cells isolated from the liver of C57BL/6 adult mice. Recombinant EMID2 was added to the Matrigel coating and the formation of tube-like structures was measured. As in the case of HUVECs, primary endothelial cells, recognized by CD31 staining in green (Figure 17A), also acquired an elongated shape and detached from the colonies, forming interconnected tubes, in response to VEGF. The presence of EMID2 again significantly reduced the number of cells that tended to elongate and connect

with other colonies, at both 1 μg/mL and 10 μg/mL (Figure 18A-B) and also decreased the length of tubes, although not significantly (Figure 18C).

The effect of EMID2 was more pronounced when recombinant VEGF was added to the culture medium, to stimulate angiogenesis (Figure 18D). Endothelial cells seeded on EMID2-containing Matrigel were less prone to connect and to detach from colonies, even in presence of VEGF. At the highest concentration (10 μg/mL), the endothelial cell colonies were completely roundish and isolated (Figure 18D). The graph in Figure 18E shows a lower number of cells acquiring an elongated shape, significant at the highest concentration (10 μg/mL), whereas the length of the tubular structures was significantly shorter at all the concentrations (Figure 18F).

These experiments are consistent with the anti-angiogenic effect of EMID2. The fact that this effect was much more evident when the protein was added into the matrix than into the medium tends to exclude a receptor-mediated mechanism on endothelial cells and rather suggests that the anti-angiogenic effect of the protein depends on its capacity to interfere with the ECM composition.

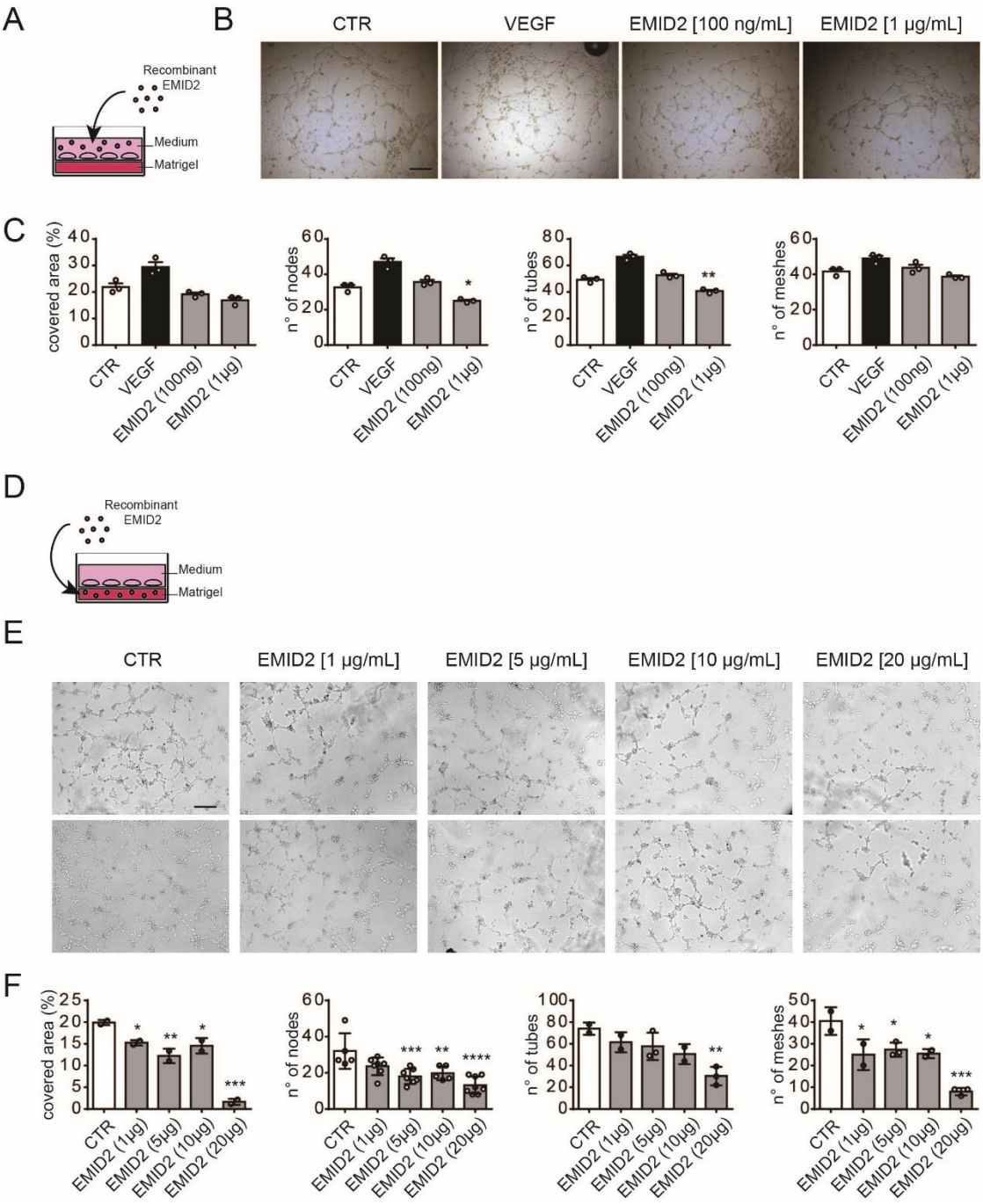

Figure 17. EMID2 inhibited tube formation of HUVECs in vitro. *(A) Schematics of the tube formation assay with HUVECs seeded on Matrigel, in which recombinant EMID2 was added to the culture medium at different concentrations. (B) Representative images of HUVECs at 3 hours after seeding on Matrigel. (C) Quantification of tube formation by manually measuring the indicated parameters using ImageJ software. (D) Schematic representation of the tube formation assay performed adding the recombinant EMID2 into the Matrigel, and representative images of HUVECs (E). Quantification of the same parameters as above are in (F). A minimum number of 3 images per condition was evaluated. Values in C and F are expressed as mean ± SEM. *p < 0.05, **p < 0.01, ***p < 0.001 by one-way ANOVA followed by Dunnett multiple comparison test. Scale bar in B and E is in 100 µm.*

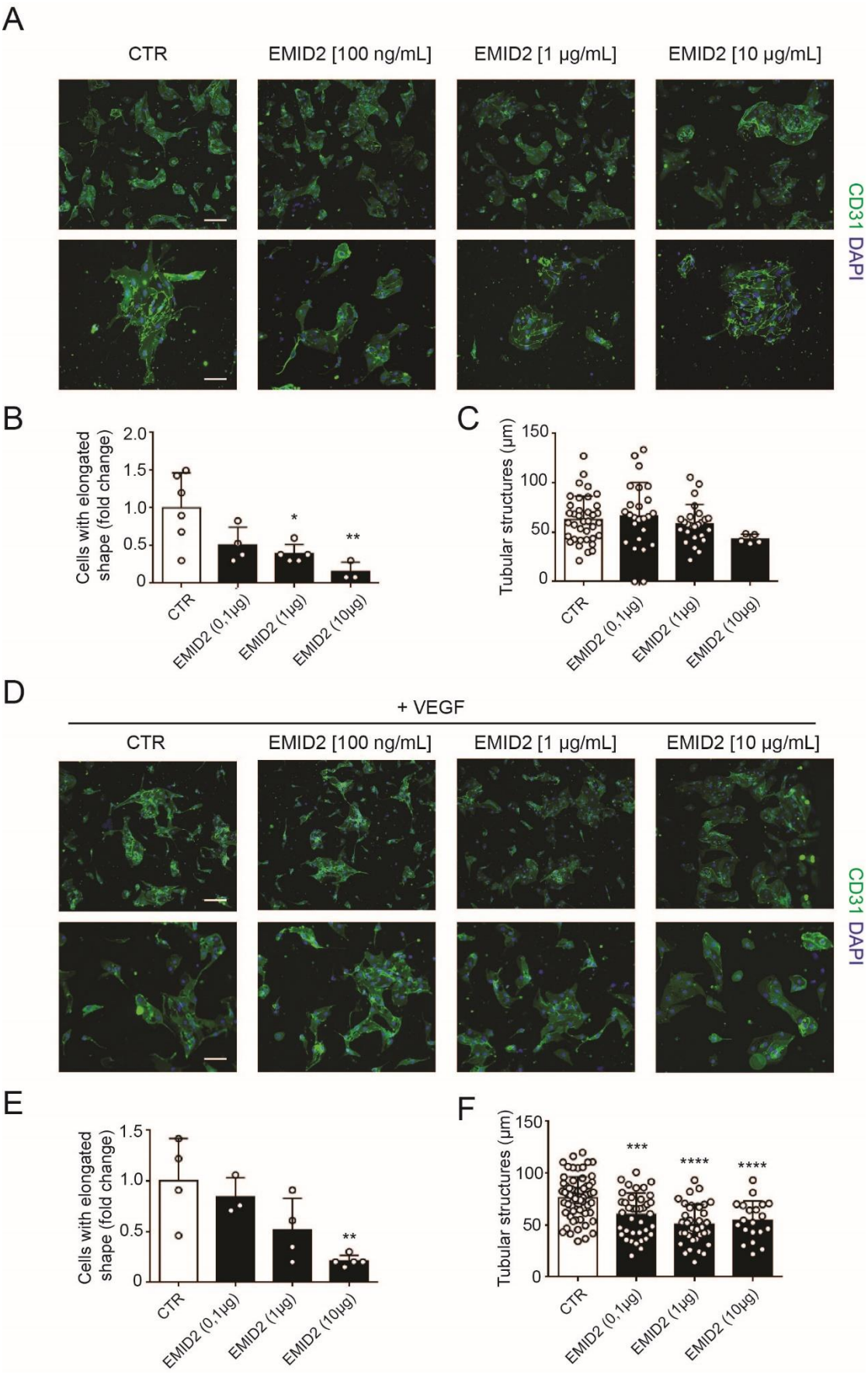
A
CTR
EMID2 [100 ng/mL]
EMID2 [1 µg/mL]
EMID2 [10 µg/mL]
CD31 DAPI
B
Cells with elongated shape (fold change)
2.0
1.5
1.0
0.5
0
*
**
CTR
EMID2 (0,1µg)
EMID2 (1µg)
EMID2 (10µg)
C
Tubular structures (µm)
150
100
50
0
CTR
EMID2 (0,1µg)
EMID2 (1µg)
EMID2 (10µg)
D
+ VEGF
CTR
EMID2 [100 ng/mL]
EMID2 [1 µg/mL]
EMID2 [10 µg/mL]
CD31 DAPI
E
Cells with elongated shape (fold change)
1.5
1.0
0.5
0
**
CTR
EMID2 (0,1µg)
EMID2 (1µg)
EMID2 (10µg)
F
Tubular structures (µm)
150
100
50
0
***
****
****
CTR
EMID2 (0,1µg)
EMID2 (1µg)
EMID2 (10µg)

Figure 18. EMID2 inhibited tube formation by primary endothelial cells. *(A) Representative images of primary endothelial cells seeded on EMID2-containing Matrigel or control Matrigel. CD31 in green, DAPI in blue. (B) Quantification of the number of cells showing an elongated shape and (C) the length of the tubular structures. (D) Representative images of primary endothelial cells seeded on EMID2-containing Matrigel or control Matrigel and with addition of VEGF in the medium. CD31 in green, DAPI in blue. (E) Quantification of the number of elongated cells and (F) the length of the tubes. A minimum of 3 images per condition were evaluated. Values in B, C, E and F are expressed as mean ± SEM. *p < 0.05, **p < 0.01, ***p < 0.001 by one-way ANOVA followed by Dunnett multiple comparison test. Scale bar in the upper line of A and D is 100 μm; in the lower line of A and D is 300 μm.*

3.5 EMID2 affects the tumor matrix

3.5.1 The tumor contained less α-SMA when EMID2 was expressed

To further characterize the capacity of EMID2 to inhibit tumor angiogenesis, we stained the LG-tumor sections with antibodies labelling α-SMA, a marker routinely used in our laboratory to detect arterial vessels. This staining did reveal the presence of numerous arteries inside tumor masses, and also highlighted the presence of several tumor-associated fibroblasts, as shown in the whole-muscle representative images in Figure 19A and the zoomed pictures in Figure 19B (α-SMA in red). It is well known that tumor growth is promoted by the activation of fibroblasts into myofibroblasts that start expressing α-SMA and acquire a contractile phenotype, becoming able to massively remodel the ECM composition and stiffness (Hinz et al., 2007). Animals injected intramuscularly with LG tumor cells and AAV9-EMID2 showed significantly decreased α-SMA positivity inside the tumor mass, compared to the animals that received tumor cells and the AAV9-CTR (Figure 19C). This suggested that EMID2 could inhibit myofibroblast activation and in this way affect the tumor matrix, resulting in reduced cancer growth.

Besides myofibroblasts, α-SMA antibodies also labelled a few arterioles, characterized by their small and round shape and largely located in the healthy muscle close to the tumor mass. As shown by the representative images in Figure 19D, a higher number of arteries (indicated by yellow arrows) were present around the tumor in the muscle injected with AAV9-EMID2, compared to control. Indeed, the border region in control tumors contained arterial vessels that exhibited the typical features of tumor vessels, with a thin and discontinued layer of α-SMA$^+$ cells and a large size (green arrows. in Figure 19D). The thicker α-SMA layer around the small vessels and the increased number of arterioles found in the AAV9-EMID2-treated muscles (Figure 19E) could be consistent with a positive effect of EMID2 on tumor vessel normalization.

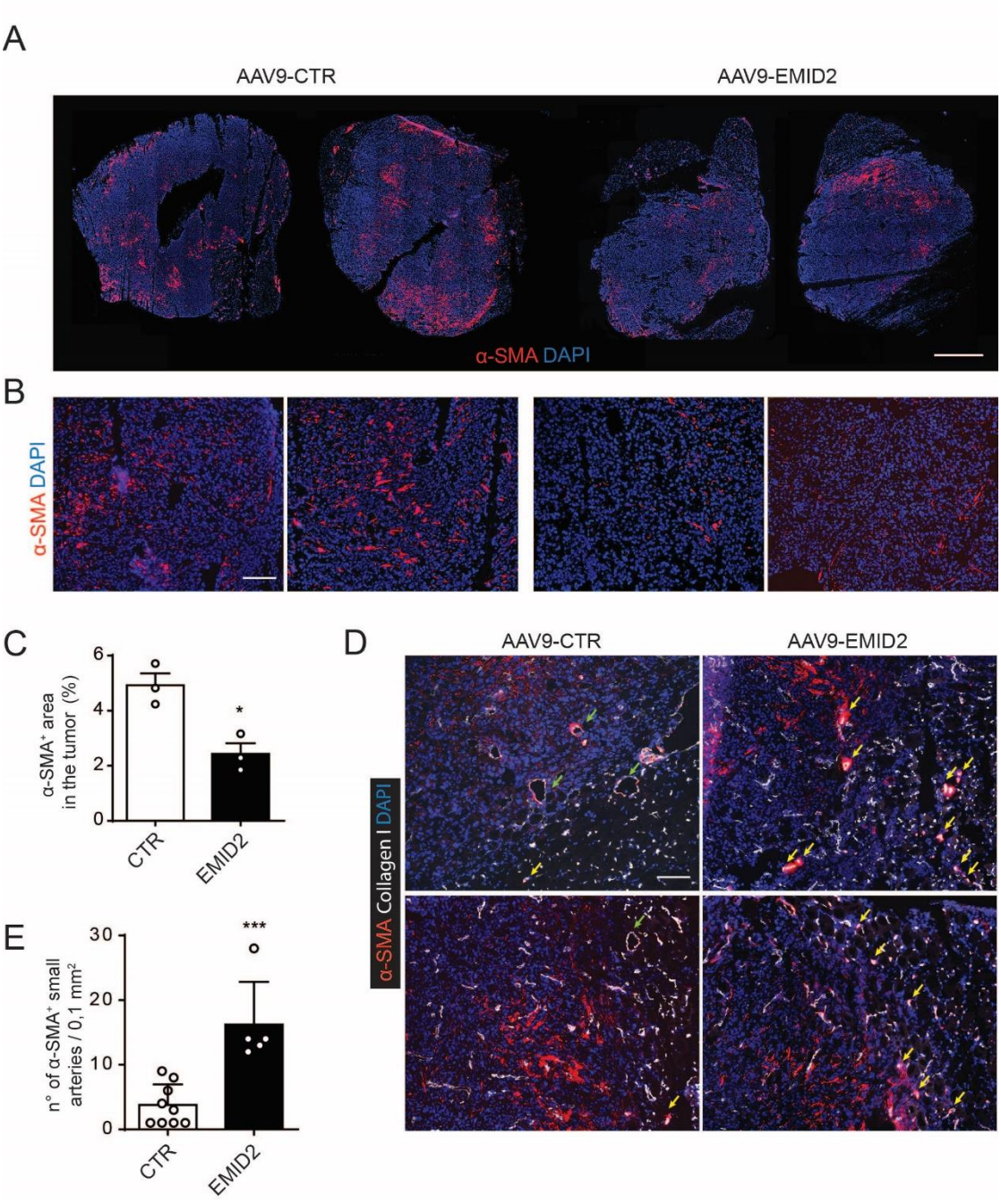

Figure 19. α-SMA was less abundant in the tumors when EMID2 was expressed. *(A) Representative whole-section and zoomed (B) images of tibialis anterior muscles injected with AAV9-CTR or AAV9-EMID2 together with LG cancer cells and stained with DAPI in blue, and α-SMA, in red. (C) Quantification of α-SMA positivity inside the tumor mass. 3 animals per condition, 4 sections per animal, representative of the muscle thickness. (D) Representative images of the border of the tumor, where small α-SMA⁺ arteries are indicated by yellow arrows and quantified in (E). DAPI in blue, α-SMA in red, CD31 in white. Values in C and E are expressed as mean ± SEM. *p < 0.05, ***p < 0.001 by unpaired Student's t test. Scale bar in A. 0.2 cm. Scale bar in B and D is 100 μm.*

3.5.2 Myofibroblast activation was inhibited by EMID2

Our observation that the tumors treated with AAV9-EMID2 contained a lower number of α-SMA$^+$ cells is indicative of a possible effect of EMID2 on myofibroblast activation, process that is essential for tumor growth and invasiveness. To investigate this possibility, we exploited a transgenic mouse model, herein referred as α-SMA-RFP/COLL-EGFP, that expresses the red fluorescent protein (RFP) under the control of the α-SMA promoter and the enhanced green fluorescent protein (EGFP) under the control of the collagen-1α1 promoter (Magness et al., 2004). This model allows to visualize fibroblast activation as a progressive induction of red fluorescence.

We first evaluated the effect of the intramuscular injection of AAV9-CTR or AAV9-EMID2 (3 x 10^{10} vg per muscle, 1 animal per condition), compared to a non-treated animal (n=1), and we could not determine differences in any group (Figure 20A, the first three muscles from the left). Subsequently, α-SMA-RFP/COLL-EGFP mice received an intramuscular injection of the AAV9-EMID2 or AAV9-CTR (3 x 10^{10} vg per muscle, 3 animals per condition) and one week later 50,000 LG cells were administered to the same muscles (schematics in Figure 20C). The mice were sacrificed after one additional week, and DAPI staining was used to recognize the tumor mass as local increase in nuclear density.

The whole-muscle images in Figure 20A and the zoomed images in Figure 20B show a marked reduction in both red and green signal inside the tumor mass, compared to control. The tumor was smaller in animals overexpressing EMID2 (quantification in Figure 20D), and myofibroblasts were significantly less abundant, as indicated by the quantification of the red signal, corresponding to α-SMA (Figure 20E). In the same tumors we also observed a reduction in collagen expression, indicated by the green signal, overall indicating a less pronounced activation of fibroblasts into myofibroblasts in EMID2-overexpressing muscle (Figure 20E).

Different from the previous experiment, in which the muscle was transduced 2 weeks prior to cancer cells in order to pre-condition the tumor microenvironment, we also performed a parallel experiment by co-injecting AAV9-EMID2 or AAV9-CTR (1.5 x 10^{10} vg per muscle, 3 animals per condition) intramuscularly together with the same number of LG cells. The results were confirmed, as represented in the images in Figure 20F-G and quantitatively measured in Figure H-I, showing a reduced tumor size and a marked reduction of α-SMA, collagen positivity and yellow signal, confirming the effect of EMID2 in reducing CAF activation inside the tumor.

To verify the capacity of EMID2 to block the transformation of fibroblasts into myofibroblasts *in vitro*, we isolated skin primary fibroblasts from α-SMA-RFP/COLL-EGFP mice and either kept them in culture to induce their spontaneous activation or co-cultured them with LG cells to accelerate their activation. Fibroblasts were either transduced with AAV9-EMID2 (2 x 10^9 vg) and AAV9-CTR or kept in culture for three days either in the presence or in the absence of

recombinant EMID2. During the culture, fibroblasts acquired a variety of red, yellow and green intensities. Separating the three colour channels, we could determine that at three days part of the cells were still green but many also turned red. Both the number of red cells and the mean red intensity were significantly reduced in fibroblasts transduced with AAV9-EMID2 or incubated with the recombinant protein (Figure 21A-C).

Also in the presence of cancer cells EMID2 was effective in inhibiting myofibroblast activation. Indeed, as shown by images in Figure 21D, fibroblasts were mostly red when co-cultured with cancer cells whereas they stayed more green when treated with EMID2 (Figure 21E). This could be quantified by measuring the red mean value, showing a reduced expression of α-SMA in fibroblasts treated with both AAV9-EMID2 and the recombinant protein, reaching statistical significance in the second case (Figure 21F).

Figure 20. EMID2 expression in the tumor reduced the presence of CAFs. *(A) Representative images of the entire tibialis anterior muscles from α-SMA-RFP/COLL-EGFP mice injected with AAV9-CTR or AAV9-EMID2, followed by injection of LG cells after one additional week. The tumor mass is indicated by the white line. DAPI in blue, endogenous α-SMA in red, endogenous Col1α1 in green. (B) Zoomed images. (C) Scheme of the experiment. (D) Quantification of the tumor size, by measuring the area of the muscle covered by high-density DAPI. We analysed 4 sections per muscle, representative of the thickness of the muscle. (E) Quantification of the red, green and yellow signal in the tumor area. (F) Whole-muscle sections and (G) zoomed images of tibialis anterior muscles from α-SMA-RFP/COLL-EGFP mice simultaneously injected with AAV9-CTR or AAV9-EMID2, and LG cancer cells. DAPI in blue, endogenous α-SMA, in red, endogenous Col1α1 in green. The tumor mass is indicated by the white line. (H) Quantification of the tumor size. (I) Quantification of the red, green and yellow signal in the tumor area. Scale bars in A and F are 0.2 cm. Scale bars in B and G are 100 μm. Values in D, E, H and I are expressed as mean ± SEM. *p < 0.05 by unpaired Student's t test.*

Figure 21. EMID2 reduced the activation of myofibroblast in vitro. *(A) Representative images of skin fibroblasts from α-SMA-RFP/COLL-EGFP mice after 3 days of culture. These cells were either transduced with AAV9-CTR or AAV9-EMID2 or incubated with the recombinant EMID2. Endogenous α-SMA in red, Col1α1 in green. (B) Quantification of the percentage of green and red fibroblasts. (C) Quantification of the red mean intensity. (D) Representative images of skin fibroblasts from α-SMA-RFP/COLL-EGFP mice, after 3 days of culture with LG cells. (E) Quantification of the number of green and red fibroblasts. (C) Quantification of the red mean intensity. Scale bars in A and D are 50 μm. Values in B, C, E and F are mean ± SEM. *p < 0.05, **p < 0.01, ***p < 0.001, ***p < 0.0001 by one-way ANOVA followed by Dunnett multiple comparison test. Scale bar in A and D is 50 μm.*

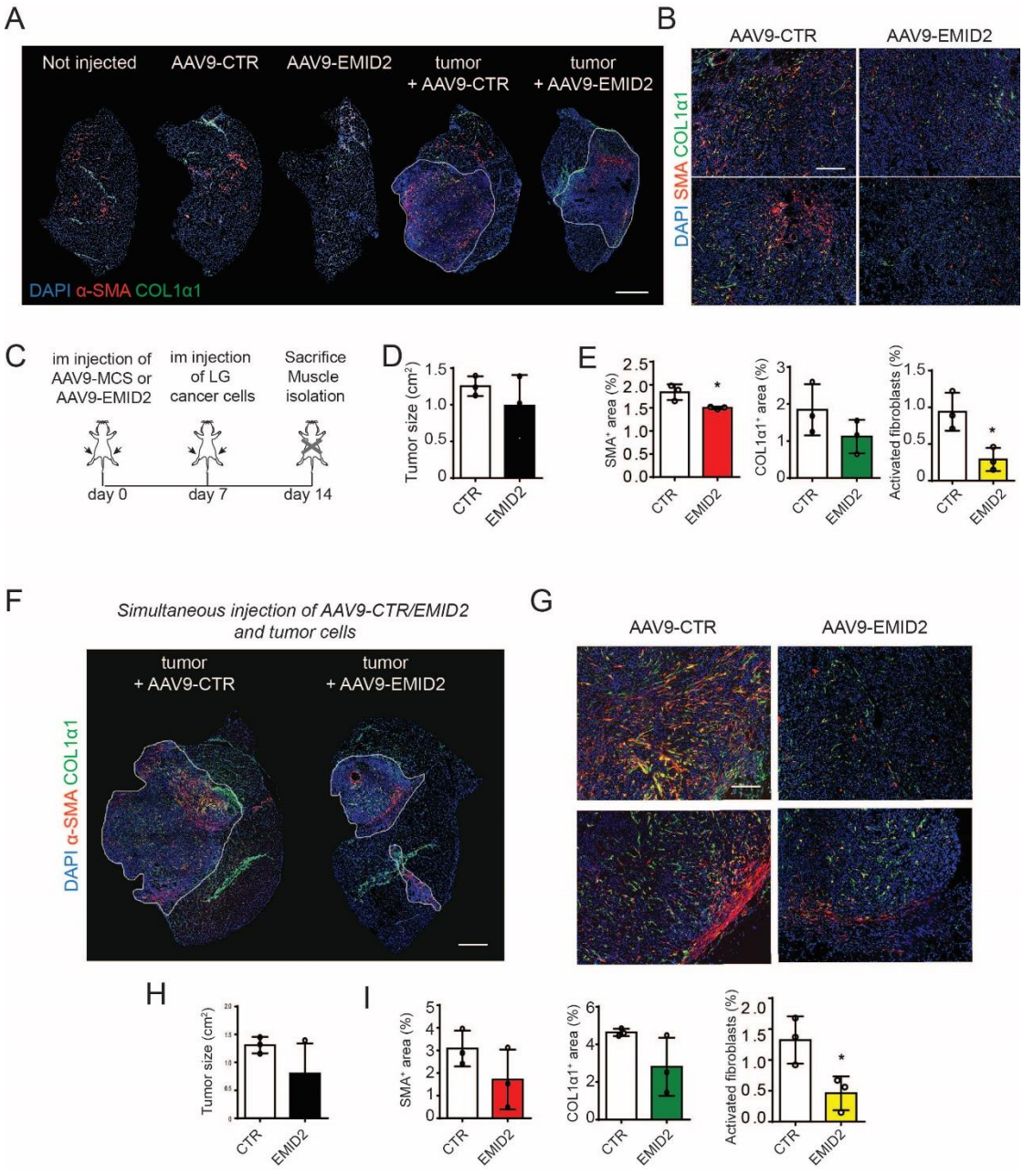
A
Not injected
AAV9-CTR
AAV9-EMID2
tumor + AAV9-CTR
tumor + AAV9-EMID2
DAPI α-SMA COL1α1
B
AAV9-CTR
AAV9-EMID2
DAPI SMA COL1α1
C
im injection of AAV9-MCS or AAV9-EMID2
im injection of LG cancer cells
Sacrifice Muscle isolation
day 0
day 7
day 14
D
Tumor size (cm²)
CTR
EMID2
E
SMA⁺ area (%)
COL1α1⁺ area (%)
Activated fibroblasts (%)
CTR
EMID2
F
Simultaneous injection of AAV9-CTR/EMID2 and tumor cells
tumor + AAV9-CTR
tumor + AAV9-EMID2
DAPI α-SMA COL1α1
G
AAV9-CTR
AAV9-EMID2
H
Tumor size (cm²)
CTR
EMID2
I
SMA⁺ area (%)
COL1α1⁺ area (%)
Activated fibroblasts (%)
CTR
EMID2

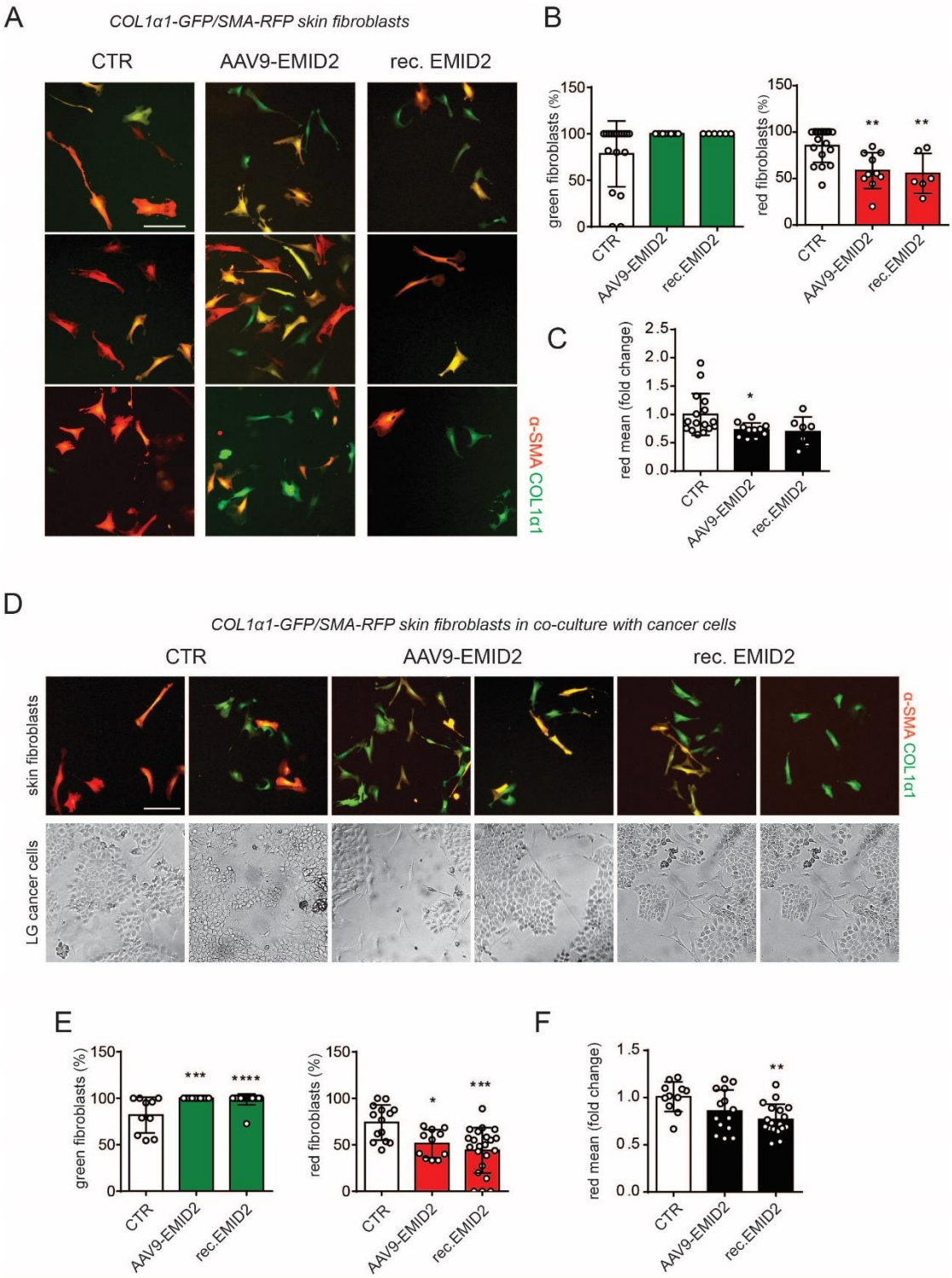
A
COL1α1-GFP/SMA-RFP skin fibroblasts
CTR
AAV9-EMID2
rec. EMID2
α-SMA COL1α1
B
green fibroblasts (%)
red fibroblasts (%)
CTR
AAV9-EMID2
rec.EMID2
C
red mean (fold change)
D
COL1α1-GFP/SMA-RFP skin fibroblasts in co-culture with cancer cells
skin fibroblasts
LG cancer cells
E
F

3.5.3 EMID2 modified the structure and composition of the ECM *in vivo* and *in vitro*

Consistent with the fact that myofibroblasts were less activated in tumors treated with AAV9-EMID2, as well as the higher anti-angiogenic activity of EMID2 when embedded in Matrigel, we hypothesized that EMID2 might profoundly modify the ECM, with functional consequences on both tumor growth and associated angiogenesis.

We first stained the LG tumors developed in the tibialis anterior after intramuscular injection of 50,000 LG cells together with AAV9-EMID2 or AAV9-CTR, to label various components of the ECM. As mentioned in the introduction, the tumor microenvironment is known to be characterized by increased abundance of collagen I and reduction of laminin. Interestingly, in the presence of EMID2, laminin content was increased (Figure 22A and quantification in Figure 22B) and collagen I was decreased (Figure 22A and quantification in Figure 22C), meaning that the matrix was more similar to the one of normal tissues, possibly counteracting tumor growth. Moreover, we observed that collagen I was not homogeneously distributed in the tumor mass. We could frequently determine areas of high collagen density in the centre of control tumors, but not in tumors treated with AAV9-EMID2. Instead, we could often observe a tendency of the collagen fibers to align parallel to the tumor border in tumors treated with AAV9-EMID2, as shown by the representative image in the lower right panel of Figure 22A. This arrangement could function as a capsule restricting cell invasion rather than promoting it, as collagen I fibers aligned perpendicularly to the tumor border were described to guide cancer cell invasion *in vitro* and *in vivo* (Riching et al., 2014).

To better characterize the effect of EMID2 in influencing ECM alignment, we cultured primary liver fibroblasts for several days and allowed them to secrete the ECM in a medium either or not supplemented with recombinant EMID2. After 9 days, the cells and the matrix were fixed and stained for ECM components. In presence of EMID2, both collagen I and fibronectin stainings showed less aligned and more relaxed fibers, that tended to fuse, resulting in a homogeneous and less structured network, as shown in Figure 22D.

Additionally, when the same matrix was decellularized and 3T3-NIH fibroblasts were seeded on top of it, they easily elongated in control conditions, but not in EMID2-conditioned ECM (Figure 22E). Indeed, both the number of protrusions (Figure 22F) and the length of filopodia (Figure 22G) of the cells seeded on the matrix were significantly decreased when the recombinant EMID2 was added during the ECM production by fibroblasts.

This data suggested that EMID2 significantly influenced the arrangement of the fibers composing the ECM *in vitro* and possibly *in vivo*. Moreover, the exposure of the tumor to EMID2 inhibited the ECM switch from laminin to collagen I, normally occurring in cancer, resulting in tumor matrix unfavourable for tumor growth and cancer cell invasion.

3.5.4 EMID2 modified the strain/stiffness properties of the matrix

We exploited rheology to explore the physical properties of the Matrigel containing EMID2. We compared the mechanical properties of a Matrigel layer containing either 10 μg/mL of recombinant EMID2 or an equal volume of PBS. We chose this concentration, as it was the most effective one in inhibiting both the migration of several cell types and the formation of tubes by endothelial cells. Matrigel is an accepted ECM model system that provides a platform for investigating cell migration within a 3D microenvironment and it behaves as a gel in terms of mechanical responses to applied forces (Albini and Noonan, 2010).

We conducted the experiments in oscillatory mode at a fixed frequency of 1.0 Hz with controlled strain amplitude (γ) of 0.01 (=1%). In all cases, Matrigel was kept in ice until 400 μL of sample were applied to the measuring stage, which was covered to maintain a temperature of 37°C in humidity. Experiments were performed in duplicate.

First, we measured the gelation kinetics for 30 minutes during Matrigel polymerization and observed a pick in the curve when EMID2 was added to the Matrigel early during polymerization (Figure 22H). This indicated that the process of gelation was accelerated by EMID2 and suggested its fast interaction with the other ECM proteins.

We then applied a series of consecutive sweeps to investigate the ability to recover after strain, as it is known that gels typically exhibit relative mechanical weakness, which worsens when subjected to repeated strains (Arevalo et al., 2010). Figure 22I and J show the graphs expressing the response of the material to the applied forces. The G' is a parameter called elastic or storage modulus and refers to the elasticity of a material when it is deformed (Figure 22I). The G'', represented in Figure 22J, refers to the viscous modulus.

A first sweep was applied at increasing strain from γ of 0.01–1.0 and did not show any difference, as we did not reach the breakage point of the network structure (black line, in Figure 22I-J). Thus, the Matrigel samples were subjected to a second sweep at increasing strain from 0.01–10.0 γ. Soon after 1 γ, we reached the breakage of the material, characterized by a sharp collapse in G' (grey line, in Figure 22I-J). However, when EMID2 was present in the Matrigel, an increased stiffness was registered by the rheometer, as indicated by the grey arrow in the right graph of Figure 22I, before the network structure broke down. We then applied a third sweep, identical to the previous one, and, as expected, we registered a recovery of the Matrigel in both conditions in terms of visco-elastic properties, as demonstrated by the plateau showing the resistance of the material to the strain (blue line, in Figure 22I-J). However, the slope of the strain/stiffness curve of the control Matrigel showed a weary behavior and its structure broke earlier than before, as indicated by the blue arrow in the left graph of Figure 22I. In contrast, the Matrigel containing EMID2 resisted longer to the applied force, as a consequence of increased elasticity rather than stiffness.

Of note, the trend of the strain/stiffness curve of the Matrigel containing EMID2 was similar to the one reported during the second sweep, suggesting that it probably recovered the almost complete functionality in terms of elasticity, although it reached the breakage point sooner (compare the grey line with the blue line, in the right graph of Figure 22I).

Overall, these data indicate that EMID2 is able to modify the visco-elastic properties of the ECM network by preserving and stabilizing the 3D structure during consecutive strain sweeps and resulting in enhanced elasticity in response to strains.

Figure 22. EMID2 modified matrix composition and structure. *(A) Representative images of tumors in tibialis anterior muscle, stained with laminin in green, collagen I in white and DAPI in blue. (B) Quantification of laminin and (C) collagen I in tumors. (D) Representative images of ECM secreted by primary fibroblasts and stained for collagen I (in white) and fibronectin (light blue). (E) NIH-3T3 fibroblasts seeded on top of the ECM produced by primary fibroblasts, stained for F-actin in green. (F) Quantification of the number and the length (G) of protruding filopodia in NIH-3T3 cells. (H) Strain/stiffness graph relative to the polymerization of Matrigel containing EMID2 (red line) or PBS as control (in black), analysed by rheology. Time in x-axis and storage modulus G' in y-axis. (I-J) Strain/stiffness graphs representing the response of Matrigel containing EMID2 or PBS to the applied sweeps. The first sweep was of γ 0.01–1.0 (in black); the second (in grey) and the third (in light blue) sweeps were of γ 0.01–10.0. Time in x-axis, storage modulus, G', in y-axis in (I) and loss modulus, G'', in y-axis in (J). Values in B, C, F, G are expressed as mean ± SEM. *p < 0.05, **p < 0.01 by unpaired Student's t test. Scale bars are reported in every set of images.*

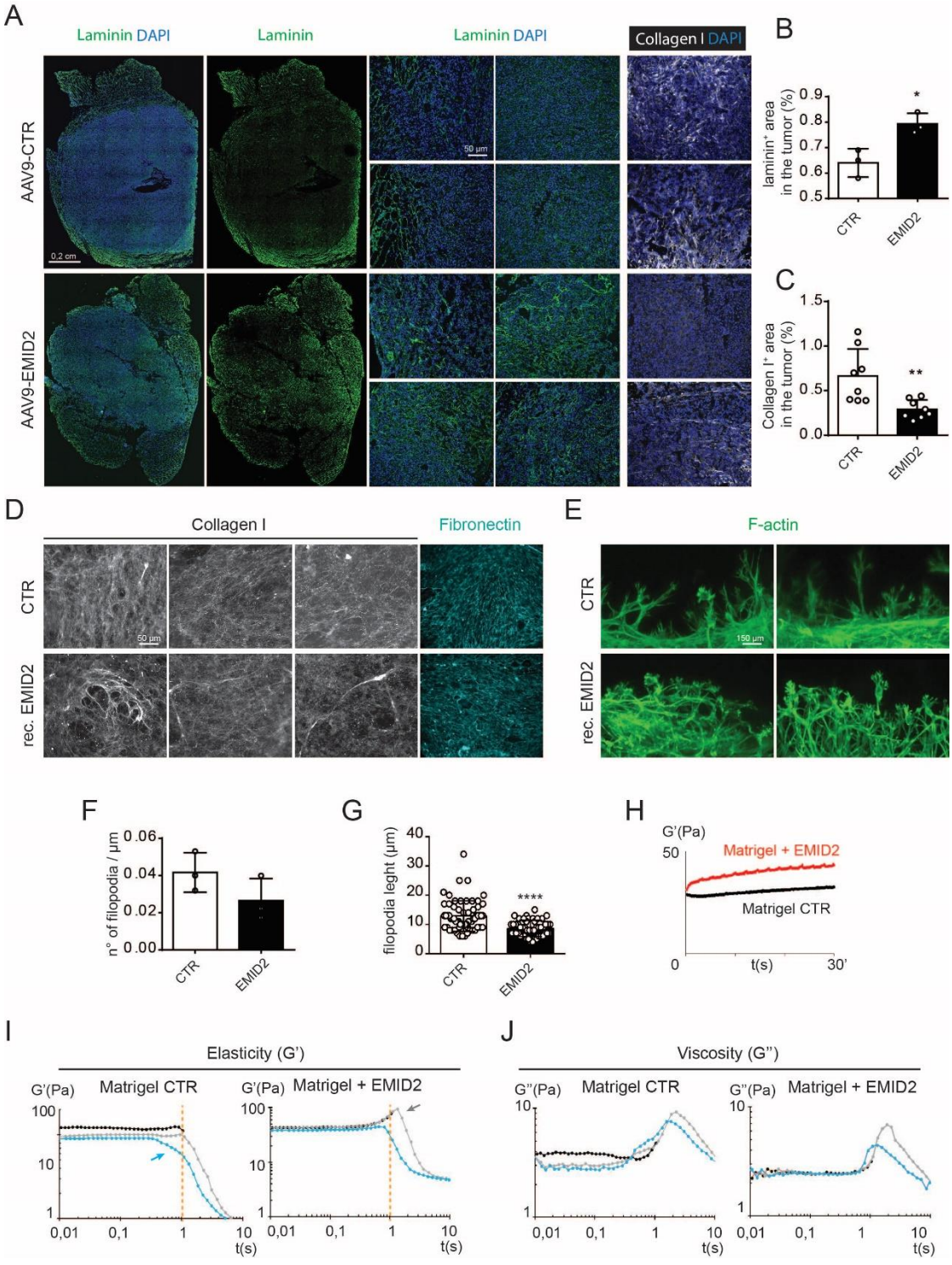
A
Laminin DAPI
Laminin
Laminin DAPI
Collagen I DAPI
AAV9-CTR
AAV9-EMID2
0.2 cm
50 µm
B
laminin+ area in the tumor (%)
CTR
EMID2
C
Collagen I+ area in the tumor (%)
D
Collagen I
Fibronectin
CTR
rec. EMID2
E
F-actin
150 µm
F
n° of filopodia / µm
G
filopodia leght (µm)
****
H
G'(Pa)
Matrigel + EMID2
Matrigel CTR
t(s)
I
Elasticity (G')
Matrigel CTR
Matrigel + EMID2
J
Viscosity (G")
G"(Pa)

3.6 EMID2 inhibits TGFβ maturation

The EMID2 protein contains a typical cysteine-rich domain of around 75 amino acids, known as the EMI domain. This domain is also contained in Elastin Microfibril Interfacer 1 (EMILIN1) and it has been shown to inhibit TGFβ signaling. The described mechanism of action implies that EMILIN1 binds to pro-TGFβ and prevents its maturation by blocking furin convertases extracellularly (Zacchigna et al., 2006). This was associated to the onset of pathologic hypertension of *Emilin1* knockout mice. TGFβ is considered a key driver in cancer, as it promotes tumor formation and malignancy in advanced tumors. Therefore, we wanted to test whether inhibition of TGFβ maturation could be a mechanism of action for EMID2 activity.

We took advantage of a construct encoding for the pro-TGFβ kindly provided by professor Piccolo and subcloned it into pGi plasmid to overexpress it in cells together with EMID2. The two plasmids were transfected in HEK-293T cells and TGFβ maturation in the supernatant was assessed by Western blot. A band of 26 kDa, corresponding to mature TGFβ, was detected when pGi-pro-TGFβ was co-transfected with an empty plasmid (Figure 23A, lane 1) but disappeared when pGi-pro-TGFβ was combined with pGi-EMID2 (Figure 23A), demonstrating that EMID2 impaired the maturation of TGFβ. In addition, we overexpressed the pro-TGFβ and a truncated EMID2, corresponding to the last part of the amino acid sequence and lacking the EMI domain. In this case, the band of the mature TGFβ was detectable as well as in the control, suggesting that, as expected, the inhibition of TGFβ maturation could be mediated by the EMI domain. Quantification in Figure 23B demonstrated the reduction of the mature form due to EMID2.

Since we showed that EMID2 impairs TGFβ maturation, we measured the amount of mature TGFβ in protein lysates of tumors developed in muscle transduced with either AAV9-EMID2 or AAV9-CTR and sacrificed 10 days after the treatment. The Western blot in Figure 23C showed that TGFβ was consistently reduced in tumors that overexpressed EMID2 compared to controls. The amount of TGFβ was normalized on tubulin and the quantification is reported in the graph in Figure 23D.

3.6.1 Inhibition of TGFβ maturation by EMID2 contributed to its anti-angiogenic function

TGFβ plays a prominent role in regulating angiogenesis, exerting potent effects on endothelial cell proliferation and migration (Ferrari et al., 2009). Therefore, we tested if the effect of EMID2 in inhibiting tube formation could be rescued by the addition of recombinant TGFβ.

We repeated the tube formation assay with HUVECs adding the recombinant EMID2 into the Matrigel at the two most effective concentrations (10 μg/mL and 20 μg/mL) and reproduced the anti-angiogenic effect described previously. The addition of recombinant mature TGFβ rescued

the angiogenic phenotype and resulted in an organized network of tube-like structures that was comparable to control, as shown by the representative images in Figure 23F. The maximal activity of TGFβ was evident at the highest concentration (20 μg/mL) of recombinant EMID2. The graphs in Figure 23F show that the rescuing effect of TGFβ at this concentration significantly increased covered area, number of nodes, tubes and meshes, compared to the condition in which EMID2 was present alone. Thus TGFβ totally prevented the anti-angiogenic effect of EMID2 on HUVECs *in vitro*, potentially explaining the reduced vascularization of the tumors injected with AAV9-EMID2.

Figure 23. TGFβ was inhibited by EMID2 and rescued its anti-angiogenic effect in vitro. *(A) Western blot of supernatants harvested from HEK-293T transfected with the indicated plasmids, containing TGFβ (secreted form, MW 26 kDa). Gel staining with chloroform was used for protein normalization. (B) Quantification of TGFβ band intensity over total protein content. (C) Quantification of mature TGFβ by Western blot in tumors grown in muscles injected with AAV9-CTR or AAV9-EMID2 and normalized on tubulin expression for quantification (D). (E) Representative images of tube formation assay performed with HUVECs. Recombinant EMID2 was added to the Matrigel and recombinant TGFβ in the culture medium. (F) Manual quantification of covered area, number of nodes and tubes, length of the meshes, using ImageJ software. A minimum of 3 images per condition were considered for the analysis. Values in B, D and F are expressed as mean ± SEM. *p < 0.05, **p < 0.01, ***p < 0.001, ****p < 0.0001 by one-way ANOVA followed by Dunnett multiple comparison test (B, F) or unpaired Student's t test (D). Scale bar in E is 100 μm.*

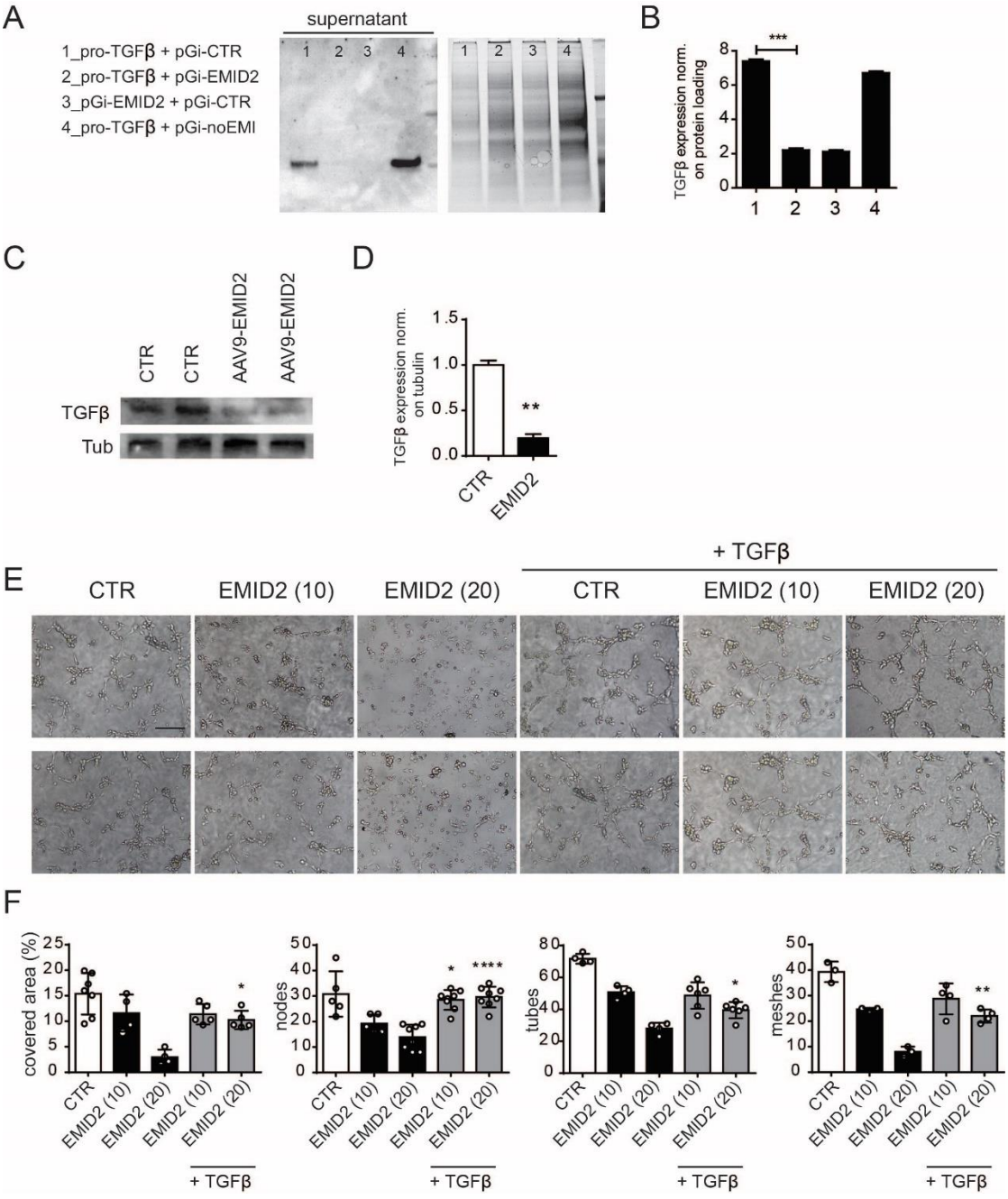
A
supernatant
1_pro-TGFβ + pGi-CTR
2_pro-TGFβ + pGi-EMID2
3_pGi-EMID2 + pGi-CTR
4_pro-TGFβ + pGi-noEMI
1 2 3 4
1 2 3 4
B
TGFβ expression norm. on protein loading
***
8
6
4
2
0
1 2 3 4
C
CTR
CTR
AAV9-EMID2
AAV9-EMID2
TGFβ
Tub
D
TGFβ expression norm. on tubulin
1.5
1.0
0.5
0.0
**
CTR
EMID2
E
+ TGFβ
CTR
EMID2 (10)
EMID2 (20)
CTR
EMID2 (10)
EMID2 (20)
F
covered area (%)
nodes
tubes
meshes
CTR
EMID2 (10)
EMID2 (20)
EMID2 (10)
EMID2 (20)
+ TGFβ

3.7 EMID2 expression in the lung protected from metastatic invasion

Finally, we wanted to assess if EMID2 was able to protect the lung from colonization by circulating cancer cells, to mimic the metastatic process. Thus, we transduced the left lung of adult C57BL/6 mice by intra-parenchymal injection of AAV6-EMID2 or AAV6-CTR (2×10^{10} vg per mouse). The AAV6 was chosen as the best serotype for lung transduction, as described in literature and confirmed in our laboratory (Halbert et al., 2001). After 2 weeks, the same mice received an intravenous injection of 10^5 cancer cells (either LG or B16-F10) and were sacrificed after 10 additional days, as schematically represented in Figure 24A. We first evaluated whether the lungs were efficiently transduced by the AAV6-EMID2 by Western blot. Figure 24B shows significant overexpression of EMID2, compared to AAV6-control-injected animals. Some spill-over of the vector occurred, as EMID2 was find to be up-regulated also in the heart of the same animals. Quantification of EMID2 protein content was normalized on tubulin and represented in the graph in Figure 24C.

We then injected 10^5 LG cells in the tail vein after transduction of the lung with either AAV6-EMID2 or AAV6-CTR (3 animals per group). LG cancer cells are known to metastasize preferentially in the lung, therefore we isolated the lungs after perfusion with PBS to remove the blood and stained them with H&E. The analysis of the left lung revealed that numerous cancer cells colonized the lungs over 10 days and started growing in metastatic foci, recognized by higher nuclear density by hematoxylin staining. Both the representative pictures of the whole left lung and the zoomed images in Figure 24D-E show a reduction in the tumor area when EMID2 was overexpressed in the lung. Both the number of tumor foci and percentage of the lung area covered by tumor cells were significantly decreased in the left lung when the animal received intra-lung administration of AAV6-EMID2 (Figure 24F-G).

The same experiment was also performed injecting 10^5 B16-F10 cells in the tail vein after transduction of the lung with AAV6-EMID2 or AAV6-CTR. This cancer cell type also metastasizes preferentially in the lung and forms multiple tumor foci, although smaller than those developed by LG cells during the same time period. Overexpression of EMID2 by AAV6 potently protected the left lung from cancer cell engraftment, as demonstrated by the lower number of tumor foci and the decreased percentage of lung tissue covered by tumor cells.

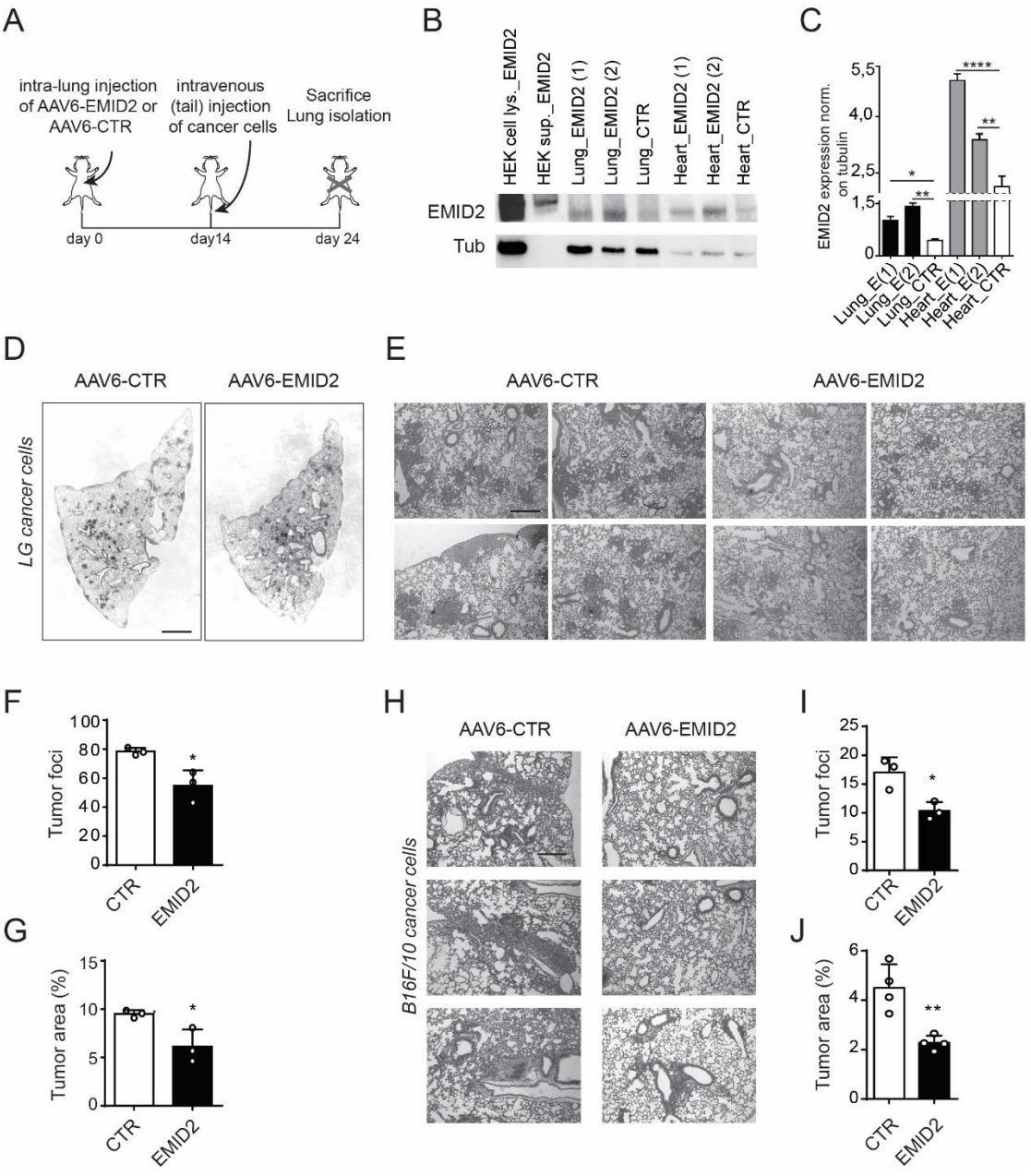

Figure 24. Expression of EMID2 in the lung protected from colonization by cancer cells. *(A) Schematic representation of the experiment. The left lung was injected with AAV6-EMID2 or AAV6-CTR and 2 weeks later cancer cells were injected intravenously. Mice were sacrificed after 10 additional days and lungs stained with hematoxylin and eosin. (B) Evaluation of the efficiency of lung and heart transduction after the injection of either AAV6-EMID2 or AAV6-CTR. The cell lysate and the supernatant of HEK-293T transfected with pGi-EMID2 were used as controls for the molecular weight. (C) Quantification of EMID2 by Western blot, relative to tubulin. (D) Representative whole and (E) zoomed images of the left lung after transduction with AAV6-EMID2 or AAV6-CTR and intravenous administration of 10^5 LG cells, stained with hematoxylin and eosin. (F) Quantification of the number of LG tumor foci in the left lung (3*

*mice per group, 4 sections per animal). (G) Percentage of area covered by LG tumor in the left lung. (H) Representative H&E images of the left lung transduced with AAV6-EMID2 or AAV6-CTR and metastasized by B16-F10 cancer cells, and relative quantification of the number of tumor foci (I) and the percentage tumor area in the left lung (J). 3 mice per group, 4 sections per animal were evaluated. Values in C, F, G, I and J are expressed as mean ± SEM. *p < 0.05, **p < 0.01, ****p < 0.0001 by one-way ANOVA followed by Dunnett multiple comparison test (C) or unpaired Student's t test (F, G, I, J). Scale bar in D is 0.2 cm. Scale bar in E and H is 100 μm.*

3.8 The “lost” factors can support the tumor growth and invasiveness

Our screening was originally designed to select for secreted proteins with anti-invasive function, with the idea that the muscle fibers that survived to cancer cell invasion might have incorporated transgenes protecting them from the tumor. In parallel, we wanted to investigate whether the factors that were “lost”, meaning that the frequency of recovered barcodes was significantly (<1SD) lower than the control condition, could promote tumor growth and invasiveness. Defensin β33 (BD33) was selected among the others and its characterization is in progress.

3.8.1 BD33 enhanced the migration of different cell types *in vitro*

First, we verified the capacity of BD33 to promote cell migration. A transwell migration assay was performed with both LLC cells and iMAECs, seeded on a porous membrane in contact with the supernatant produced by HEK-293T cells transfected with pGi-BD33 plasmid to produce the secreted protein. As shown by the representative images in Figure 25A, both LLC and iMAEC cells migrated more when BD33 was added to the lower compartment. The quantification of LLC and iMAEC cell migration is reported in the graph in Figure 25D and 25E, respectively. This result was confirmed by a scratch assay, performed with iMAEC. Again, iMAECs closed the gap faster when a BD33-enriched supernatant was added to the cells, compared to control. A similar effect in promoting cell migration was obtained both in absence (Figure 25B) and in presence (Figure 25C) of FBS, suggesting a minor role of cell proliferation in explaining the effect. The relative quantifications are reported in the graphs in Figure 25B-C.

Also in this case, we repeated the wound healing assay by adding mouse recombinant BD33 to different cell types at various concentrations. B16-F10 cancer cells migrated significantly more compared to control upon BD33 administration in a dose-dependent manner, as shown by the representative images and quantification (Figure 25H-I). A similar, dose-dependent effect was exerted by BD33 both in HUVECs and primary fibroblasts (Figure 25J-K and Figure 25L-M, respectively), confirming the capacity of BD33 to promote the migration of multiple cell types.

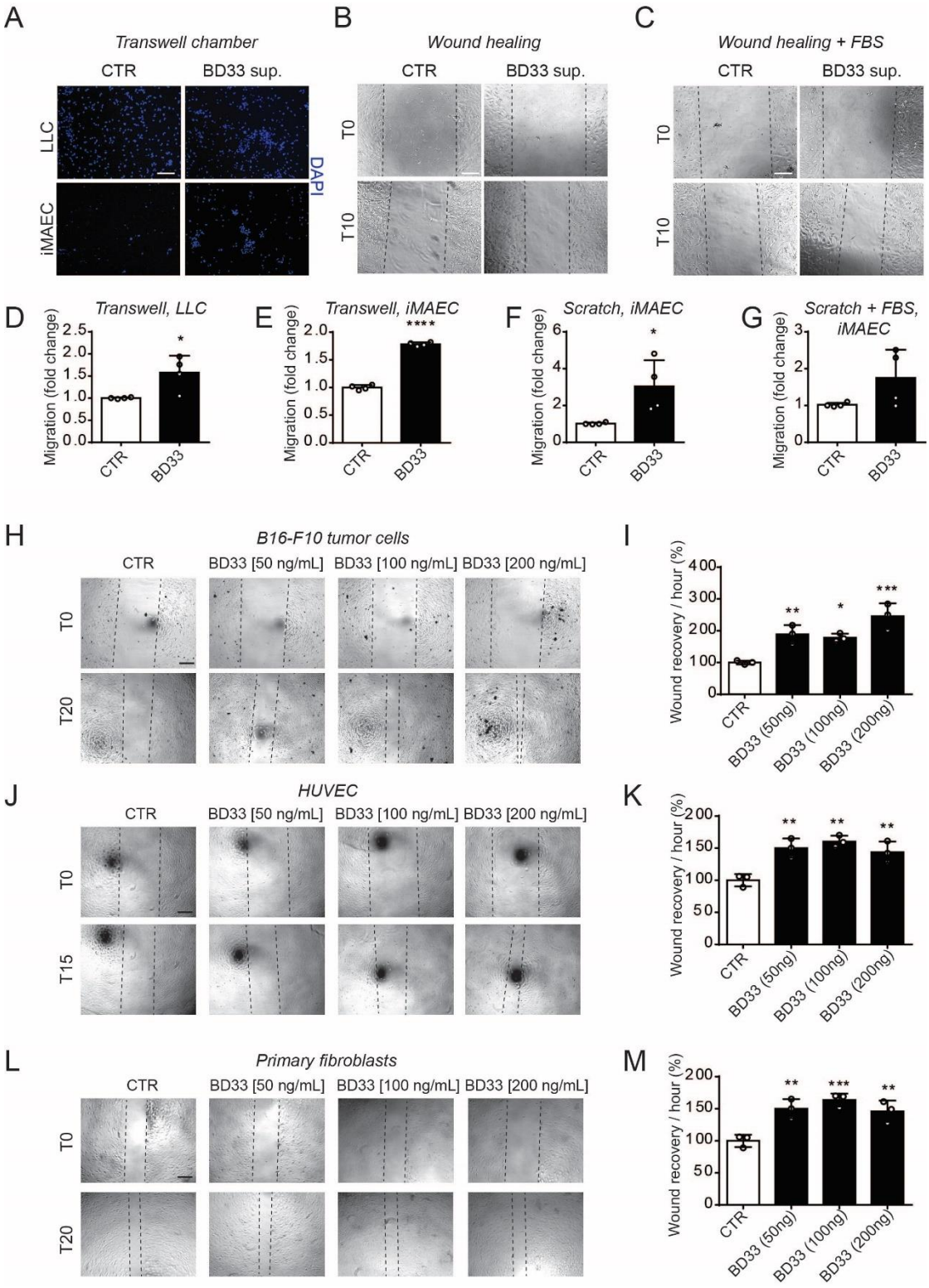

Figure 25. BD33 increased cell migration. *(A) Representative images of transwell migration assay with LLC cells and iMAECs toward HEK-293T supernatant containing BD33 or not. DAPI in blue. (B) Wound healing assay performed with iMAECs in HEK-293T supernatant containing BD33, either in the absence or (C) in the presence of FBS. (D) Quantification of LLC and (E) iMAEC cell migration in the transwell assay. (F) Quantification of the gap closure*

*by iMAECs either in the absence or (G) in the presence of FBS. (H) Wound healing assay with B16-F10 cells, (J) HUVECs and (L) primary liver fibroblasts incubated with BD33 at the indicated concentrations. Images were acquired immediately after the scratch and after 15 or 20 hours. Values in D, E, F, G, I, K and M are expressed as mean ± SEM. *p < 0.05, **p < 0.01, ***p < 0.001, ****p < 0.0001 by unpaired Student's t test (D, E, F, G) or one-way ANOVA followed by Dunnett multiple comparison test (I, K, M). Scale bar in A, B, C, H, J and L is 100 μm.*

We also performed another experiment in which HEK-293T transfected with pGi-BD33 were seeded in one chamber of the wound healing support and primary fibroblasts were seeded in the other chamber. Upon removal of the barrier, fibroblasts migrated to cover the empty space, as in the wound healing assay. This experiment allowed us to analyse the directional migration of fibroblasts toward the source of BD33. The representative images in Figure 26A show that fibroblasts (on the right) migrated significantly faster toward HEK-293T cells (on the left) secreting BD33 than towards those transfected with a control plasmid (empty pGi). Migration speed was measured as distance covered by the fibroblast edge between the starting (T0) and final (T20) timepoint (Figure 26B).

We fixed the cells before the gap closure and stained them with DAPI and phalloidin to label F-actin and characterize morphological features selectively appearing in fibroblasts migrating toward the source of BD33. Most fibroblasts in the migrating front were characterized by a large shape with evident stress fibers, typically present in cells that sense the presence of a stimulus for migration in their environment. Fibroblasts migrating toward HEK-293T secreting BD33 presented a broader and more flattened shape, with a leading edge oriented toward the source of BD33, numerous cell protrusions and lamellae. Fibroblasts in the control condition were less oriented, with a significant lower number of cells presenting leading edges, as shown by the quantification in Figure 26D. Moreover, thinner and fewer actin stress fibers were detected in the cells migrating toward BD33, whereas they were more abundant in control fibroblasts, suggesting that a directional migration was occurring (Figure 26C). Indeed, migrating fibroblasts are characterized by large lamellipodia extending into the surrounding space with few stress fibers, whereas more stationary fibroblasts present a reduced number of protrusions and multiple stress fibers (Sugawara et al., 2016).

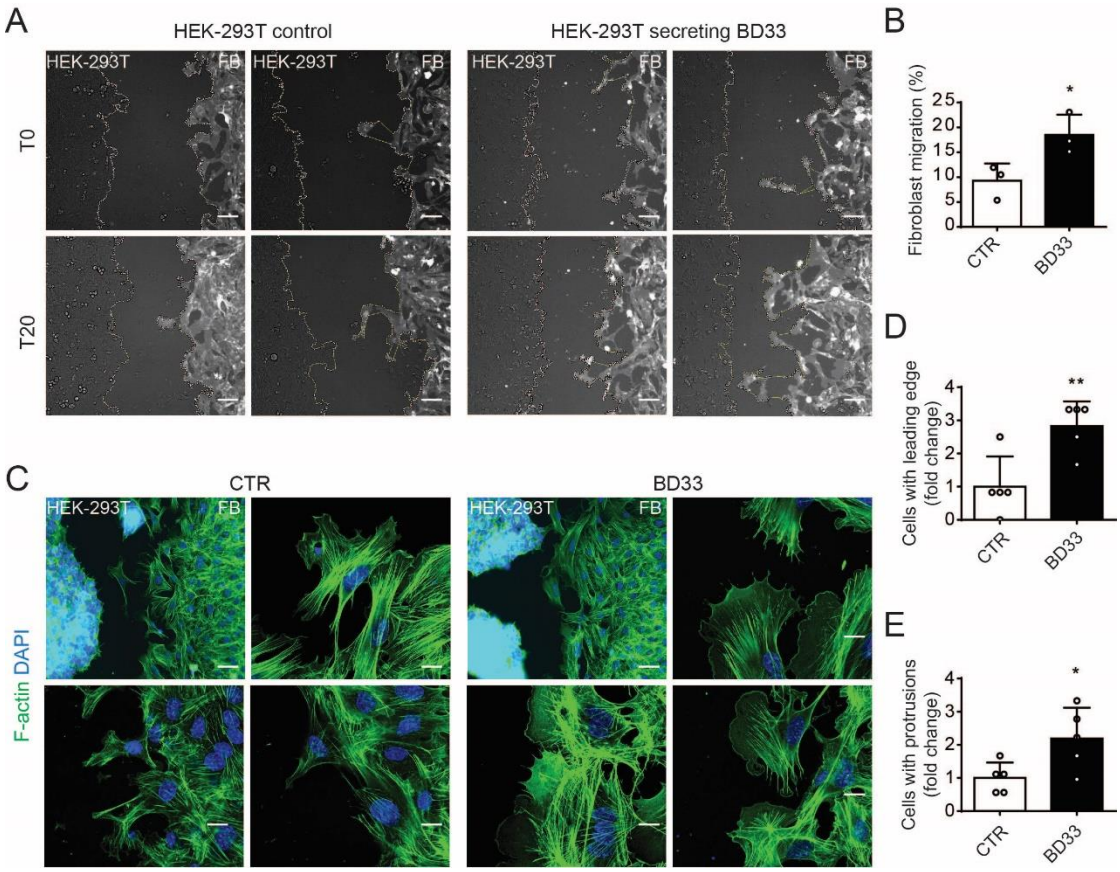

Figure 26. BD33 stimulated the directional movement and pro-migratory phenotype of fibroblasts. *(A) Wound healing assay performed by seeding HEK-293T transfected with pGi-BD33 or the empty pGi in the left chamber and primary liver fibroblasts in the right chamber. (B) Quantification of fibroblast migration. (C) Representative images of migrating fibroblasts stained for F-actin in green, and DAPI in blue. (D) Quantification of the number of cells showing a leading edge or (E) protrusions toward the HEK-293T cells. Values in B, D and E are expressed as mean ± SEM. *p < 0.05, **p < 0.01 by unpaired Student's t test. Scale bar in A and the upper left image of the two panels in C is 100 μm. Scale bar in the rest of images in C is 300 μm.*

3.8.2 BD33 stimulated tumor growth and proliferation both *in vitro* and *in vivo*

To evaluate the tumorigenic potential of BD33 *in vivo*, we injected 1.5 x 10^{10} vg of AAV9-BD33 or AAV9-CTR together with 50,000 LLC cells in the *tibialis anterior* muscle of adult C57BL/6 mice. After 10 days, the muscle was isolated for immunostaining. The area covered by cancer cells, recognized by the elevated nuclear density, was larger when the muscle was transduced with AAV9-BD33 compared to control, as shown by the representative images in Figure 27A and the quantification in Figure 27B. Moreover, a significant higher number of $Ki67^{+}$ cells, identifying proliferating cells, was detected in the tumor area grown in the muscle

transduced with BD33, suggesting that the latter had sustained cancer cell growth likely through increased proliferation and migration.

To verify this hypothesis *in vitro*, we incubated both iMAEC and LLC cells with supernatant collected from HEK-293T transfected with pGi-BD33 to produce the secreted protein or the empty pGi as a control. By adding EdU for 1 hour before fixation, we evaluated the percentage of EdU^+ cells either in the presence or in the absence of BD33. The representative images in Figure 27D show that BD33 stimulated the proliferation of both iMAEC and LLC cells, reaching statistical significance (Figure E-F). Moreover, the incubation of HUVECs with the recombinant protein also increased the percentage of proliferating cells, thus confirming the pro-proliferative effect of BD33 on a wide spectrum of cells (Figure 27G-H).

To confirm the pro-proliferative effect of BD33 on cancer cells *in vivo*, we administered 1.5 x 10^{10} vg of AAV9-BD33 or AAV9-CTR together with 50,000 LG cells in the *tibialis anterior* muscle of adult mice and isolated the muscles 10 days later. The tumor mass was easily recognizable by the increased nuclear density, largely corresponding to proliferating cells, as highlighted by the green line in the whole-section images in Figure 27I. In the muscle transduced with AAV9-BD33, the tumor grew significantly more (Figure 27J) and the percentage of proliferating cells was higher (Figure 27K-L), indicating accelerated tumor growth by BD33.

3.8.3 BD33 activated the EGFR pathway in HUVECs

Since this is the first evidence that BD33 could exert a pro-migratory and pro-proliferative effect on cancer and endothelial cells and there are no candidate receptors/pathways likely involved in mediating its activity, we performed the RTK assay, that allows to detect changes in phosphorylation of 39 different mouse receptor tyrosine kinases. HUVECs were starved in serum-free medium supplemented with hydrocortisone, bFGF and EGF for 6 hours before incubating them with 200 ng/mL of recombinant BD33. After 30 minutes, HUVECs were lysed and the array was incubated with the protein lysate overnight. An anti-Phospho-Tyrosine-HRP Antibody was used to detect the phosphorylation of the receptors spotted in the array (Figure 27M). By quantifying the relative intensity of each spot signal, we detected a statistically significant activation of EGFR in HUVECs after incubation with BD33, as shown in Figure 27N. This result represents the first evidence for a possible involvement of the EGFR pathway in mediating a pro-angiogenic and pro-tumorigenic effect of BD33.

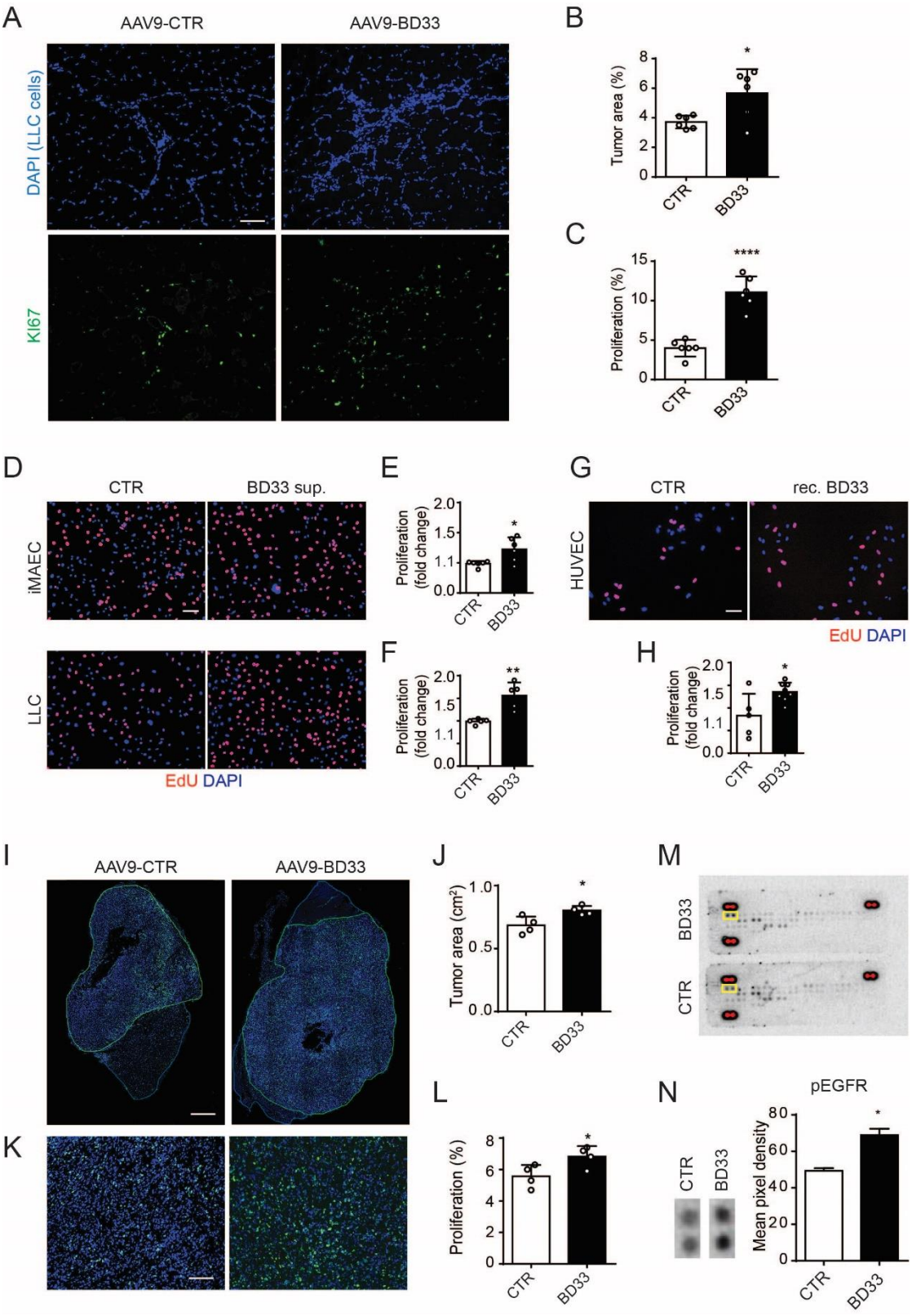

Figure 27. BD33 stimulated the proliferation of different cell types and sustained tumor growth in vivo. *(A) Representative images of LLC tumor cells co-injected with AAV-BD33 or AAV9-CTR in the tibialis anterior muscle. DAPI in blue, Ki67 in green. (B) Quantification of the tumor area, identified by the increased nuclear density. (C) Quantification of the percentage of proliferating cells in the tumor. (D) Representative images of iMAEC or LLC cells incubated*

*with supernatant collected from HEK-293T transfected with pGi-BD33 or empty pGi. EdU was added to the culture medium for 1 hour before fixation. DAPI in blue, EdU in red. (E) Quantification of proliferating iMAEC and (F) LLC cells. (G) Representative images of HUVECs incubated with recombinant BD33 at 100 ng/mL. EdU was added prior to fixation and EdU^+ cells were counted (H). (I) Representative whole-section images of tumors, highlighted by the green line, in muscles injected with LG cells together with AAV-BD33 or AAV9-CTR. (J) Quantification of the size of LG-tumors. (K) Representative images of proliferating cancer cells. DAPI in blue, Ki67 in green. (L) Quantification of proliferation in the LG tumor. (M) RTK assay performed by incubating the array with protein lysate of HUVEC incubated with the recombinant BD33. The yellow boxes highlight the phosphorylation of EGFR in the two conditions, quantified in (N) as mean pixel density. Values in B, C, E, F, J, L and N are expressed as mean ± SEM. *p < 0.05, **p < 0.01, ****p < 0.0001 by unpaired Student's t test. Scale bar in A, D, G and K is 100 µm. Scale bar in I is 0.2 cm.*

3.8.4 BD33 promoted angiogenesis

Next, we investigated the vascularization of LG tumors grown in the *tibialis anterior* muscles transduced with either AAV9-BD33 or AAV9-CTR. By CD31 staining, we identified a higher endothelial cell area and density in tumors grown in BD33-overexpressing muscles, as shown in Figure 28.

We also tested the pro-angiogenic effect of BD33 in HUVECs using the tube formation assay. Cells were seeded on Matrigel and incubated with recombinant BD33 at different concentrations, using recombinant VEGF as a positive control. After a few hours, HUVECs formed vessel-like structures in all conditions. At 100 ng/mL BD33 significantly increased the percentage of covered area and the number of tubes. The number of nodes and meshes was also increased but without reaching statistical significance. At 1 µg/mL, the effect of BD33 was more pronounced, resulting in 2-fold increase in the area covered by tubes (Figure 28E), increase in the number of vessel-like structures (Figure 28F), and meshes (Figure 28G). The number of nodes was also increased, but not significantly (Figure 28H).

The pro-angiogenic effect of BD33 was also confirmed in primary endothelial cells isolated from mouse liver in the same tube formation assay. Endothelial cells can be easily distinguished from contaminating fibroblasts by their positivity for both ERG and CD31. The incubation with the recombinant BD33 at 100 ng/mL promoted the formation of tube-like structures by primary endothelial cells, which showed a higher number of protrusions and extended structures formed by aligned cells trying to connect distant colonies, as shown by the representative images in Figure 28I and quantification of the length of tube-like structures in Figure 28J.

These results support a pro-angiogenic effect of BD33 both *in vitro* and in tumors *in vivo*.

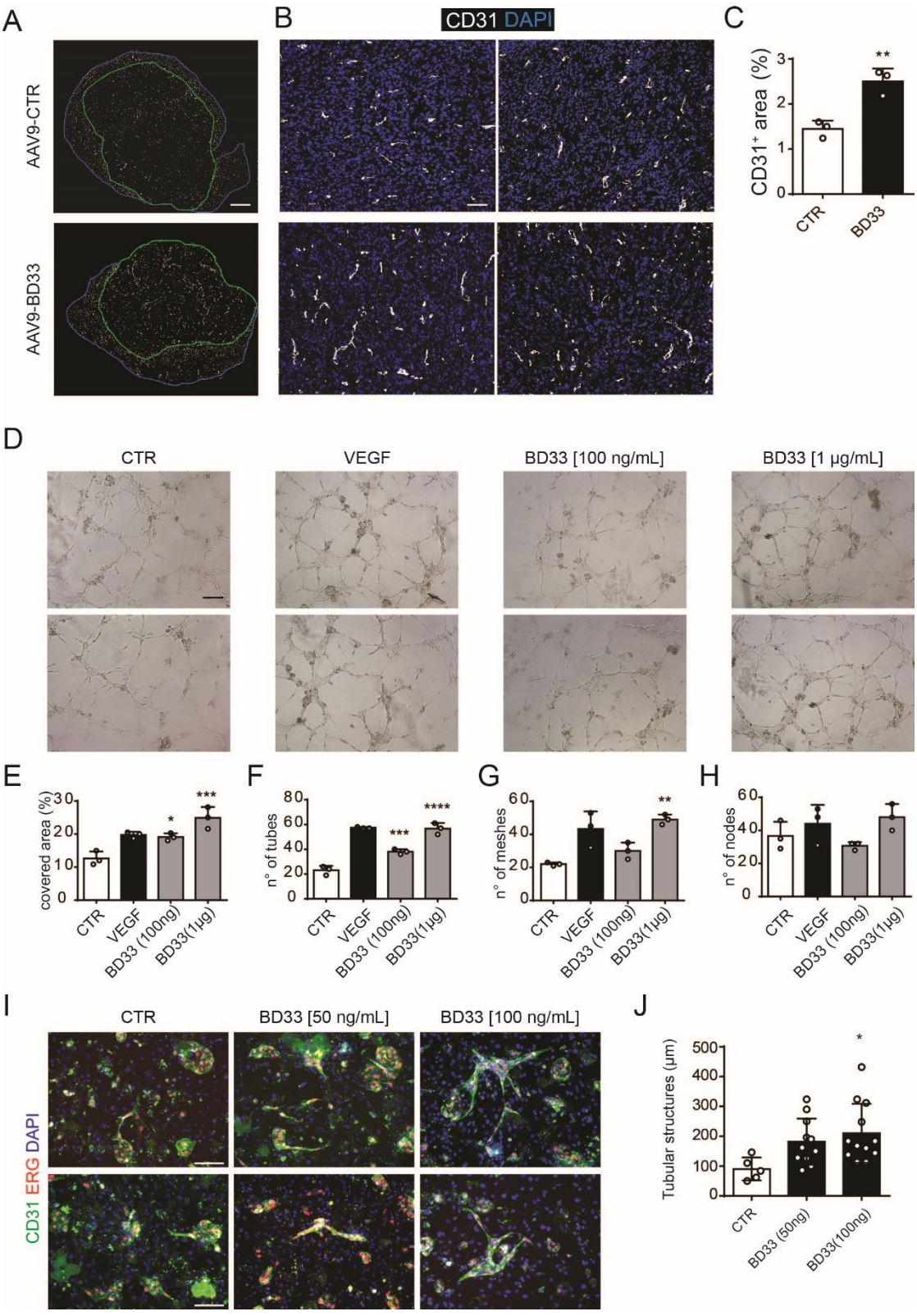
A
B
CD31 DAPI
C
AAV9-CTR
AAV9-BD33
CD31⁺ area (%)
CTR
BD33
D
CTR
VEGF
BD33 [100 ng/mL]
BD33 [1 µg/mL]
E
covered area (%)
F
n° of tubes
G
n° of meshes
H
n° of nodes
CTR
VEGF
BD33 (100ng)
BD33(1µg)
I
CTR
BD33 [50 ng/mL]
BD33 [100 ng/mL]
CD31 ERG DAPI
J
Tubular structures (µm)
CTR
BD33 (50ng)
BD33(100ng)

Figure 28. BD33 had a pro-angiogenic effect in vitro and in tumors in vivo. *(A) Representative images of whole muscles injected with AAV9-CTR or AAV9-BD33 together with LG cancer cells and stained for CD31 in white. The tumor mass is highlighted by the green line. (B) Images of the centre of the tumor. DAPI in blue, CD31 in white. (C) Quantification of vessel density as the percentage of the area covered by CD31 in the tumor. (D) Tube formation assay with HUVECs adding recombinant BD33 or VEGF to the culture medium. (E) Quantification of the percentage of the area covered by the network, (F) number of tubes, (G) meshes and (H) nodes by manual measurement using ImageJ software. (I) Representative images of primary endothelial cells seeded on Matrigel and incubated with recombinant BD33 at the indicated concentrations. CD31 in green, ERG in red, DAPI in blue. (J) Quantification of the length of the tubular structures. Values in C, E, F, H and J are expressed as mean ± SEM. *p < 0.05, **p < 0.01, ***p < 0.001, ****p < 0.001 by unpaired Student's t test (C) or one-way ANOVA followed by Dunnett multiple comparison test (E, F, G, H). Scale bar in A is 0.2 cm. Scale bar in B, D and I is 100 μm.*

4. DISCUSSION

Over the last decades, the screening of genetic libraries has become a powerful tool for the identification of proteins, genes and small nucleic acids with desired characteristics. Essential biological information has derived from these *in vitro* cell-based applications but, unfortunately, they are limited in predicting the *in vivo* relevance of the molecules that have been selected. Moreover, some factors exploit multiple and pleiotropic mechanisms to exert their function *in vivo*, thus they can be hardly identified by *in vitro* assays. Indeed, several molecules that had emerged from *in vitro* screenings have largely failed *in vivo* in animal models and in clinical applications. FunSel offers an efficient approach to identify secreted proteins exert a desired function, without any a priori knowledge. This strategy exploits gene delivery by AAV vectors, which are characterized by exquisite tropism for quiescent cells and tissues and provide long-lasting transgene expression (Asokan et al., 2012). The selection is based on a competitive process occurring between a beneficial gene and genes that are either neutral or detrimental. The best performing transgene, which results enriched among the others, is selected because it confers a survival advantage to the cell expressing it. This advantage can derive either from a direct effect of the transgene in the targeted cell, or from indirect mechanisms, such as changes in vascularization, immune response, etc. This approach is thus expected to efficiently select and identify pleiotropic factors, able to exert their beneficial function through multiple mechanisms that are difficult to reproduce simultaneously *in vitro*.

The FunSel approach has been previously validated in two models (Bortolotti et al., 2017; Ruozi et al., 2015), which paved the way to its exploitation for the selection of novel factors contrasting cancer cell invasion.

4.1.1 FunSel successfully selected secreted factors with anti-invasive and anti-angiogenic properties

This work required a series of pilot experiments to optimize the selection strategy for our purpose. First, we needed a cancer cell type with intermediate aggressiveness, progressively growing and replacing the transduced muscle fibers, but allowing the recovery of a sufficient amount of transgenes after the selective pressure. We compared the pattern of growth of four cell types and eventually chose LLC cells for their more modest aggressiveness and ability to infiltrate and eliminate muscle fibers.

Next, we had to experimentally determine the most appropriate timing for an efficient selection. For this purpose, we generated a pilot pool of AAV9 vectors containing a factor with proven anti-invasive and anti-tumorigenic function, Sema3A. This pilot experiment allowed to set a

time period of 10 days as necessary and sufficient to drive the selection of our positive control, Sema3A. The feasibility and reliability of the strategy was also confirmed in the real FunSel experiment, as among the enriched factors we found various molecules previously associated with cancer inhibition. For instance, Dickkopf-4 (DKK4) was enriched in pool 5 (3rd position) and scored 53th in the final ranking. Its overexpression was reported to decrease cell proliferation and migration, whereas its knockdown by shRNA promoted cell proliferation and invasiveness (Chouhan et al., 2016). Moreover, a potential tumor suppressor role has been attributed to DKK4, as it negatively regulates the Wnt/β-catenin pathway (Fatima et al., 2012). An additional example is the tissue inhibitor of metalloproteinase-3 (TIMP3), that was the 4th enriched factor in pool 4 and also in the top part of the final ranking, TIMP3 is a metalloproteinase inhibitor with established anti-tumor function as it inhibits the adhesion, migration and progression of papillary thyroid carcinoma cells *in vitro* and *in vivo* (Anania et al., 2011).

Of particular interest, two other members of the EDEN superfamily were identified as protective in the screening, in addition to EMID2. EMILIN2 resulted the most enriched factor in pool 21 and 33rd in the final ranking. It negatively affects tumor development by activating apoptosis in several cell lines and regulates Wnt signalling pathway, resulting in reduced tumor growth and metastasis to lymph nodes (Marastoni et al., 2014). EMILIN1 was the 2nd enriched factor in pool 21 and scored 77 in the final ranking. EMILIN1 exerts an anti-proliferative and tumor suppressor role through the involvement of α4β1 integrin (Modica et al., 2017). Moreover, EMILIN1 has been demonstrated to modulate angiogenesis, lymphangiogenesis, vascular elasticity and integrity in several models. Indeed, Emilin1 knockout mice show a marked hypertension due to the EMI domain-mediated inhibition of TGFβ maturation (Zacchigna et al., 2006). Therefore, FunSel strategy resulted successful also in selecting novel proteins involved in tumor progression.

Technical accuracy guaranteed the reliability of the screening

Although the power of FunSel selection in our experimental approach was confirmed by both the pilot experiment, in which Sema3A was efficiently selected, and the selection of some proteins with known anti-cancer properties, we extensively validated the accuracy of our NGS results.

While control muscles, injected only with a pool of AAV vectors, provided homogeneous results, a higher degree of variability was detected in samples subjected to cancer cell injection. By individually analysing each pool, the highest variability was observed among lost factors, while the enriched ones were more reproducibly selected in different animals (Figure 9). We hypothesized that the power of selection exerted by LLC cells could have been importantly

changed by the composition of the various pools, each one containing proteins of different nature and function. To face this variability, in each pool we included multiple controls. We verified the correct encapsidation of each transgene inside AAV vectors by lysing the viral pool and assessing the purity of the reads, in order to exclude the transgenes that were not represented due to technical issues. Following these quality controls, a few factors (22, Figure 9) were removed from the final ranking. Some transgenes were characterized by a non-detectable number of reads only in one or a few muscles after the selection of cancer cells, but were fairly represented in others. This was somehow expected using a model of selection *in vivo*. Thus, we decided to consider those factors in the analysis, provided that the number of readable samples was at least equal to 3 ($n \geq 3$). Three pools (3, 16 and 24) resulted characterized by very high variability in most of the transgenes and therefore we excluded them from the final analysis, in order not to affect the whole ranking.

4.1.2 EMID2 is a novel potential biotherapeutic for cancer therapy

EMID2 potently inhibited tumor growth by altering the tumor microenvironment

Besides a few enriched factors that are already known to exert anti-cancer function, most of the selected transgenes encoded for proteins with unknown function or were associated to other biological contexts. This represents an additional evidence that FunSel allows the identification of potent novel factors, without any a priori knowledge of their function (Ruozi et al., 2015).
We validated the first 10 top hits of the final ranking by multiple *in vitro* assays, to identify the most potent factor able to modulate both cancer cell and endothelial cell migration. Considering the potential of FunSel to select molecules exerting pleiotropic functions (Bortolotti et al., 2017; Ruozi et al., 2015), we aimed at identifying a molecule possibly able to modulate both cancer cell invasiveness and angiogenesis, thus representing a double-edged sword for cancer therapy. EMID2 was chosen as the best factor, because it significantly reduced LLC and iMAEC cell migration both in transwell and scratch assays (Figure 11), also in the presence of FBS. Other three additional factors, PTH, FGF3 and LCN12, similarly reduced cell migration *in vitro*, but were not equally potent *in vivo*. Indeed, the AAV9 encoding for EMID2 induced a striking reduction of tumor growth in two cancer models. Although the muscle is rarely affected by cancer, we used it as the site of tumor implantation because it is efficiently transduced by AAV vectors, in particular by serotype 9, thus allowing a high expression of the transgenes. In addition, it represents a spatially confined and easy-to-isolate organ (Zacchigna et al., 2014).
This model allowed us to evaluate multiple changes occurring in the tumor upon overexpression of EMID2.

First, the tumor was significantly less vascularized in the presence of EMID2 (Figure 15) as indicated by a reduced number of $CD31^+$ vessels. It is well established that tumor vessels are necessary to support tumor growth and 'vessel blocking' strategies (i.e. bevacizumab) have been largely exploited to inhibit angiogenesis and approved by the FDA for clinical use (Crawford and Ferrara, 2009). The anti-angiogenic effect of EMID2 was confirmed both *in vitro* (Figures 17-18) and *in vivo* (Figure 16), also in non-cancerous conditions. In particular, the AAV9-mediated overexpression of EMID2 during early post-natal development, reduced the vascularization of normal muscles (Figure 16). Additional studies will be needed to understand whether EMID2 can also modify tumor-like features of the vessels, such as leakiness. Indeed, an emerging therapeutic strategy to promote drug delivery and reduce tumor progression relies on the normalization of tumor vessels, that are fenestrated and irregularly branched. Indications that EMID2 could also promote vessel maturation emerged when we detected small and thick arteries in the border of the tumor, similar for example to the effect induced by low doses of anti-VEGF antibodies, TGFβ blockade or bone-marrow circulating monocytes exerting antitumor activity and vessel normalization (Carrer et al., 2012; Liu et al., 2012). To experimentally address the possibility that the structural maturation induced by EMID2 determines functional normalization of vessels, we plan to inject FITC dextran intravenously into the animals and assess the perfusion/leakiness of tumor vessels. An improved vessel perfusion would be determinant for the efficient intratumoral distribution of therapeutic molecules, that can also be easily verified experimentally by the administration of fluorescent drugs such as doxorubicin (Liu et al., 2012).

Another important change determined by the overexpressed EMID2 was the reduction of α-SMA^+ myofibroblasts in the tumor (Figures 19-20). CAFs are the most abundant component of the tumor stroma and co-evolve with cancer to acquire a pro-tumor phenotype, mostly by remodelling the ECM and secreting growth factors to sustain cancer cell growth and invasiveness (Chen and Song, 2019). We confirmed that EMID2 blocked the activation of CAFs *in vitro*, by culturing skin fibroblasts isolated from α-SMA-RFP/COLL-EGFP mice (Figure 21). Indeed, green fibroblasts start expressing α-SMA spontaneously when cultured *in vitro* and this activation is accelerated by the co-culture with cancer cells. EMID2 significantly reduced spontaneous myofibroblast activation either when delivered as recombinant protein or by AAV9 transduction, whereas in presence of cancer cells a more pronounced effect was exerted by the recombinant protein at 1 μg/mL. This could be explained by the fact that transduction efficiency of primary fibroblasts by AAV9 could not sustain a sufficient production of protein to strongly contrast cancer-derived CAF differentiation factors. The effect of EMID2 was evident also in tumors induced by the injection of cancer cells in the muscle of α-SMA-RFP/COLL-EGFP mice. As previously reported, the efficient transduction of the muscle by AAV of serotype 9 allows robust transgene expression *in vivo*, much more efficiently than in

cultured cells (Zacchigna et al., 2014). A similar effect was observed when EMID2 was overexpressed by AAV9 one week before cancer cell injection or also when AAV9-EMID2 was delivered simultaneously to cancer cells. Considering that AAVs require a short but necessary time window to express the transgene, this result suggests that EMID2 could be effective also whether administered in growing cancer lesions.

Consistent with the reduced presence of CAFs, important differences in the tumor ECM were determined by the overexpression of EMID2. The ECM plays a critical role in tumor progression because it supports cancer cell growth by releasing growth factors and influencing their migration through its composition, topography and physical properties. The composition and alignment of the various constituents of the matrix have been largely demonstrated to determine cancer cell aggressiveness and represent tracks for migration (Riching et al., 2014).

We observed that the massive changes in ECM composition, usually associated to cancer and entailing up-regulation of collagen I and down-regulation of laminin where both reversed by EMID2, that induced preservation of a more physiological matrix structure. The hypothesis that EMID2 could modulate ECM protein biosynthesis is supported by two gene-association studies that correlate *EMID2* gene variations with diseases associated to defective collagen biosynthesis, as corneal collagen fibrillogenesis (Rada et al., 1993) and nasal polyps (Pasaje et al., 2012). Indeed, EMID2 has been shown to interact with HSP47, a molecular chaperone involved in collagen biosynthesis (Sato et al., 2002). This could represent a major pathogenic mechanism in exacerbated asthma episodes, characterized by abnormal deposition of fibronectin and collagens in the nasal mucosa, a condition known as subepithelial fibrosis and often causing nasal polyps. In muscles injected with AAV9-EMID2 and cancer cells, we detected a stripe-shape deposition of collagen I at the tumor border, possibly constituting a sort of capsule containing the expansion of the tumor mass, as it happens in breast cancer and other epithelial lesions (Man, 2010). It is thus possible that EMID2 inhibits tumor growth by modifying the tumor matrix composition. The role of EMID2 in modifying the tumor ECM should be further investigated *in vivo* by characterizing the relative abundance of the most common types of collagens (i.e. collagen IV, mostly represented in the basement membrane of the tumor capsules) and assessing the effect of EMID2 in reducing invasion of cancer cells in epithelial tumors, that are normally contained by a structured capsule, which is disrupted by cancer cells during the process of invasion.

Indications that EMID2 could act through a matrix-mediated mechanism of action rather than by a receptor-dependent signalling first came from the fact that the addition of the recombinant protein into the culture medium slowed down the migration of several cancer cells and also fibroblasts (Figure 14). Secondly, in the tube formation assay performed with HUVECs, EMID2 reduced the formation of vessel-like structures when the recombinant protein was added into the cell medium, but its anti-angiogenic effect was more pronounced when we added the

recombinant EMID2 directly into the Matrigel before polymerization. We would tend to exclude that the poor reduction on tube formation exerted by the recombinant EMID2 in the medium was attributable to protein degradation, as we assessed the formation of tubular structures a few hours after HUVEC seeding. Most probably, and consistent to the ECM changes induced by AAV9-EMID2 administration *in vivo*, EMID2 altered cell behaviour by interacting with the proteins of the matrix and thus modifying the structure of Matrigel. Indeed, Matrigel is a reconstituted basement membrane rich in laminin, collagens, bridging molecules (i.e. entactin), heparan sulfate proteoglycans (i.e. perlecan), and several growth factors (i.e. TGF-β, EGF and FGF) that mimics the tumor ECM and constitutes a complex network, finally dictating cell behaviour and mechanotransduction (Albini and Noonan, 2010). It is known that modification of matrix composition, for example by adding ECM-interacting proteins such as fibronectin to the Matrigel, profoundly alters the mechanical properties of the matrix and thus the behaviour of cells in contact with it (Zaman et al., 2006). We used rheology to measure the capacity of EMID2 to modify the mechanical properties of the Matrigel. By adding the protein to the Matrigel during its polymerization, we could reveal an immediate interaction of the recombinant EMID2 with the material, thus suggesting an incorporation of the protein into the network that determined a change in stiffness and elasticity, particularly evident when the matrix was subjected to external forces. A correct balance between compressive/tensile strength and elasticity is fundamental to preserve the correct homeostasis of tissues (Walker et al., 2018). The increased stiffness, observed in tumors, promotes integrin activation, Rho-dependent cytoskeletal tension and cell invasion (Dupont et al., 2011; Xiao and Ge, 2012). EMID2 increased the elasticity of the Matrigel where it was embedded and preserved the integrity of the network upon application of sustained forces, suggesting its capacity to modulate ECM and mechanotransduction.

Consistently, primary fibroblasts cultured for several days in the presence of EMID2 secreted an ECM with major topological differences compared to the control and determined important changes in cell behaviour (Figure 22D-G). We have so far characterized the matrix structure by immunofluorescence staining using antibodies for the main ECM components, namely collagen I and fibronectin. Further details could be obtained using Raman spectroscopy or Second Harmonic Generation (SHG) microscopy (Auner et al., 2018; Tilbury et al., 2017). Consistent with the results of the tube formation assay, in which EMID2 inhibited the capacity of endothelial cells to form tube-like structures (Figures 17-18), the incorporation of EMID2 in the ECM also limited the propensity of cells to sprout and migrate. The identification of the molecular mechanisms and signalling pathways responsible for the reduced cell motility will be crucial to characterize the role of EMID2 in modulating ECM features. We hypothesize an involvement of adhesion molecules. For example, cells seeded on EMID2-containing matrix could activate less FAK, as its expression is known to correlate with highly stiff matrices

(Schedin and Keely, 2011). Moreover, matrix elasticity heavily regulates YAP and TAZ signalling, known to display either nuclear or cytoplasmic localization depending on mechanotransduction (Dupont et al., 2011).

The anti-tumor effect of EMID2 involves the inhibition of TGFβ maturation

EMID2 belongs to the EMI domain endowed (EDEN) superfamily, that comprises 7 genes which are subdivided into three groups. The first family includes *Emu1* and *Emu2* genes, that produce EMID1 and EMID2 proteins, respectively, and share only the EMI domain with the other members (Leimeister et al., 2002). The second family comprises one gene called EMILIN-truncated (*EMILIN-T*), that is similar in structure, apart for the C-terminal globular domain of C1q (gC1q), to the proteins of the third larger family, including Emilins and Multimerins (Colombatti et al., 2011). Apart from MMRN1 that is mostly sequestered in endothelial cells, platelets and megakaryocytes (Adam et al., 2005), the proteins of the EMILIN family are major components of the ECM. All the proteins of the superfamily share the EMI domain, which is a cysteine-rich repeat modulus of approximately 80 amino-acids always located at the N-terminus and very conserved in the EDEN proteins, indeed sharing a 60 to 70% of sequence homology among the members. Cysteine-rich domains are quite common in ECM proteins, but the EMI domain is unique for several reasons: (i) it is always located at the N-terminus; (ii) different from other cysteine-rich moduli that are always composed by either 6 or 8 cysteine residues, it has 7 cysteines located at fixed positions, with the exception of MMRN1, in which it lacks the second cysteine; (iii) it presents a very preserved consensus sequence toward the C-terminus (Doliana et al., 2000).

The EMI domain has been previously demonstrated to mediate the inhibition of TGFβ maturation in *Emilin1* knockout mice, resulting in vascular defects and arterial hypertension (Zacchigna et al., 2006). Considering the important role of TGFβ signalling in the progression of advanced tumors, we hypothesized that the anti-tumor effect exerted by EMID2 could be at least partially attributable to TGFβ inhibition. We confirmed that EMID2 blocked the activation of TGFβ *in vitro* and *in vivo* (Figure 23). It is possible that the limited availability of mature TGFβ in the tumor microenvironment contributed to the changes detected after EMID2 overexpression, namely reduced angiogenesis, less CAF activation and changes in the ECM. We demonstrated that the anti-angiogenic effect induced by EMID2 could be rescued *in vitro* by adding recombinant TGFβ to HUVEC culture medium, thus indicating that the absence of active TGFβ could be responsible for the anti-angiogenic activity of the protein. TGFβ plays a critical role in both normal vascular development and in tumor angiogenesis (Safina et al., 2007). Inhibition of TGFβ could also be associated to the proposed ability of EMID2 to induce vessel normalization, as it has been demonstrated to promote the recruitment of perivascular

cells into tumor vessels thus augmenting perfusion and drug delivery (Liu et al., 2012). Moreover, blocking TGFβ also resulted in decreased collagen I density in the tumor matrix, as we observed in EMID2-treated tumors, with further enhancement of chemotherapy efficacy (Liu et al., 2012). Finally, TGFβ is the main activator of CAFs. By blocking TGFβ, EMID2 could reduce the amount of activated fibroblasts and thus the establishment of a pro-tumorigenic ECM. To verify this hypothesis, we added recombinant TGFβ to fibroblasts in the presence of EMID2 and abrogated its capacity to inhibit their activation, thus demonstrating that also this effect of EMID2 was largely dependent on inhibition of TGFβ signalling. To further assess the relevance of this mechanism *in vivo*, we plan to co-inject an AAV9 vector codifying for the precursor of TGFβ (pro-TGFβ) together with cancer cells and AAV9-EMID2 or AAV9-CTR in the muscle.

Recombinant EMID2 for cancer therapy

Our experiments showed that EMID2 exerts a remarkable anti-tumor effect *in vivo* by modifying several characteristics of the tumor microenvironment, namely tumor vascularization, CAF activation and ECM composition. How can we translate these findings into a new therapy? FunSel has been intentionally designed and generated to identify therapeutic secreted factors that could be administered as recombinant proteins, not necessarily dependent from vector-based delivery.

To test whether EMID2 could be efficient in protecting the lung from metastasis, we performed an experiment in which the lungs of adult mice were transduced with an AAV6 to overexpress EMID2. When cancer cells (LG or B16-F10) were injected intravenously, they preferentially metastasized into the lungs, due to both their tropism and the physical location of the lung as the first organ massively perfused by the venous circulation. This model is generally accepted for evaluating cancer cell metastasis (Yang et al., 2012). Notably, EMID2 protected the lung from cancer cell engraftment, as both the size and the number of tumor foci were reduced with both cell types. Although very preliminary, this experiment suggests that EMID2 could be used as a therapy to contrast cancer metastasis, particularly in case of patients treated for primary tumors known to preferentially metastasize in the lung (i.e. breast cancer, colon-rectal cancer). The intranasal administration of the biotherapeutic treatment to target the respiratory system could be feasible and allow a limited dosage compared to intravenous delivery. However, in that case, the protective effect of EMID2 would be restricted to the lungs, thus allowing cancer metastasis in other organs. Therefore, we plan to test whether the intravenous administration of EMID2 could block the cancer engraftment in multiple body sites, particularly considering the other major targets of metastasis, such as liver and kidney. Moreover, to confirm the possible therapeutic efficacy of EMID2, we will consider other mouse models to assess metastasis,

including the injection of cancer cells subcutaneously in a Matrigel plug followed by resection or administration of 4T1 breast tumor cells into the mammary gland (Yang et al., 2012).
Based on its strong effect on contrasting the formation of a pro-tumor microenvironment and the promising results obtained by combined therapies, EMID2 could be used in combination with other targeted biotherapeutics, such as monoclonal antibodies, to target multiple tumor pathways (Roma-Rodrigues et al., 2019). Certainly, in the perspective of transforming EMID2 in an effective biotherapeutic product, not only the effective dosage should be experimentally determined, but the serum half-life and immunogenicity of the recombinant protein should be assessed and potentially improved (Kintzing et al., 2016).

4.1.3 The double power of FunSel: identifying novel proteins with pro-tumor function

Although the main idea underlying FunSel screening was to select secreted proteins with anti-invasive function, the "loss" of transgene expression during the process of selection allowed the identification of proteins potentially promoting tumor invasion. Thus, the factors identified by the lowest log value could be exploited to find new targets for cancer therapy. The function of most of the "lost" factors in the ranking is completely unknown, rendering them novel interesting candidates. Among the 10 "lost" factors, 4 are associated with less than 3 publications (Ntn3, Gm128, Prss42, 4921515J06Rik) and one, namely EG654453, also named defensin β33 (BD33) has been included in the large family of the defensins by computational studies (Schutte et al., 2002). We decided to study the function of BD33 for two main reasons. First, this was the transgene represented by the lowest log value in its original pool (pool 11) as well as in the final ranking (Figure 9). Second, defensins are antimicrobial peptides recently described to contribute to human tumor development and progression, thus supporting the hypothesis of BD33 pro-tumorigenic role (Winter et al., 2016). Indeed, we demonstrated that BD33 promotes *in vitro* migration of several cell types and increases cancer cell proliferation and tumor angiogenesis both *in vitro* and *in vivo*. In a perspective of therapeutically blocking BD33 for tumor growth suppression, we thought to investigate its expression in human cancers. Unfortunately, BD33 sequence is very conserved in horse, mouse and rat, but not in humans. A protein sequence analysis performed using the Protein Data Bank (PDB) database indicates that BD33 is for the 30% identical to Tick Carboxypeptidase Inhibitor (TCI) and they share the same folding and mechanism of interaction with carboxypeptidases. TCI is a tight binding inhibitor that blocks the enzymatic action of different metallo-carboxypeptidases, including Thrombin Activatable Fibrinolytic Inhibitor (TAFI) (Arolas et al., 2005). TAFI is a zymogen that is converted to activated TAFI (TAFIa) by plasmin, thrombin, and thrombin/thrombomodulin complexes. TAFIa, in turn, reduces plasminogen activation to plasmin, which is considered a

pro-metastasis enzyme due to its capacity to cleave multiple substrates, including ECM proteins and pro-MMPs (Dano et al., 2005). Therefore, TAFIa seems to play a key role in regulating ECM proteolysis in breast cancer and possibly angiogenesis and enhancing its activation has been suggested as a therapeutic strategy to block invasion and metastasis of breast cancer cells (Bazzi et al., 2016). Albeit speculative, a possible mechanism for explaining the pro-tumor function of BD33 described in our experiments could involve its interaction with TAFI (correspondent to carboxypeptidase B2, CPB2, in mouse) that results in the blockade of TAFIa, thus promoting tumorigenesis. If this will be confirmed, BD33 could represent a therapeutic molecule for treatment of thrombotic disorders, such as kidney fibrosis or chronic thromboembolitic pulmonary hypertension, where the blockade of TAFIa has been proved to regulate dysregulation of fibrinolysis and enhance survival in rats (Atkinson et al., 2015; Satoh et al., 2017).

5. REFERENCES

Acerbi, I., Cassereau, L., Dean, I., Shi, Q., Au, A., Park, C., Chen, Y.Y., Liphardt, J., Hwang, E.S., and Weaver, V.M. (2015). Human breast cancer invasion and aggression correlates with ECM stiffening and immune cell infiltration. Integrative biology : quantitative biosciences from nano to macro *7*, 1120-1134.

Adam, F., Zheng, S., Joshi, N., Kelton, D.S., Sandhu, A., Suehiro, Y., Jeimy, S.B., Santos, A.V., Masse, J.M., Kelton, J.G., *et al.* (2005). Analyses of cellular multimerin 1 receptors: in vitro evidence of binding mediated by alphaIIbbeta3 and alphavbeta3. Thrombosis and haemostasis *94*, 1004-1011.

Aguirre-Ghiso, J.A. (2007). Models, mechanisms and clinical evidence for cancer dormancy. Nature reviews Cancer *7*, 834-846.

Albini, A., and Noonan, D.M. (2010). The 'chemoinvasion' assay, 25 years and still going strong: the use of reconstituted basement membranes to study cell invasion and angiogenesis. Current opinion in cell biology *22*, 677-689.

Ambati, B.K., Nozaki, M., Singh, N., Takeda, A., Jani, P.D., Suthar, T., Albuquerque, R.J., Richter, E., Sakurai, E., Newcomb, M.T., *et al.* (2006). Corneal avascularity is due to soluble VEGF receptor-1. Nature *443*, 993-997.

Anania, M.C., Sensi, M., Radaelli, E., Miranda, C., Vizioli, M.G., Pagliardini, S., Favini, E., Cleris, L., Supino, R., Formelli, F., *et al.* (2011). TIMP3 regulates migration, invasion and in vivo tumorigenicity of thyroid tumor cells. Oncogene *30*, 3011-3023.

Arevalo, R.C., Urbach, J.S., and Blair, D.L. (2010). Size-dependent rheology of type-I collagen networks. Biophysical journal *99*, L65-67.

Arolas, J.L., Lorenzo, J., Rovira, A., Castella, J., Aviles, F.X., and Sommerhoff, C.P. (2005). A carboxypeptidase inhibitor from the tick Rhipicephalus bursa: isolation, cDNA cloning, recombinant expression, and characterization. The Journal of biological chemistry *280*, 3441-3448.

Arsic, N., Zacchigna, S., Zentilin, L., Ramirez-Correa, G., Pattarini, L., Salvi, A., Sinagra, G., and Giacca, M. (2004). Vascular endothelial growth factor stimulates skeletal muscle regeneration in vivo. Molecular therapy : the journal of the American Society of Gene Therapy *10*, 844-854.

Asokan, A., Schaffer, D.V., and Jude Samulski, R. (2012). The AAV Vector Toolkit: Poised at the Clinical Crossroads. Molecular therapy : the journal of the American Society of Gene Therapy *20*, 699-708.

Atkinson, J.M., Pullen, N., Da Silva-Lodge, M., Williams, L., and Johnson, T.S. (2015). Inhibition of Thrombin-Activated Fibrinolysis Inhibitor Increases Survival in Experimental Kidney Fibrosis. Journal of the American Society of Nephrology : JASN *26*, 1925-1937.

Auner, G.W., Koya, S.K., Huang, C., Broadbent, B., Trexler, M., Auner, Z., Elias, A., Mehne, K.C., and Brusatori, M.A. (2018). Applications of Raman spectroscopy in cancer diagnosis. Cancer metastasis reviews *37*, 691-717.

Aya-Bonilla, C.A., Marsavela, G., Freeman, J.B., Lomma, C., Frank, M.H., Khattak, M.A., Meniawy, T.M., Millward, M., Warkiani, M.E., Gray, E.S., *et al.* (2017). Isolation and detection

of circulating tumour cells from metastatic melanoma patients using a slanted spiral microfluidic device. Oncotarget.

Azzouz, M., Ralph, G.S., Storkebaum, E., Walmsley, L.E., Mitrophanous, K.A., Kingsman, S.M., Carmeliet, P., and Mazarakis, N.D. (2004). VEGF delivery with retrogradely transported lentivector prolongs survival in a mouse ALS model. Nature *429*, 413-417.

Bautch, V.L., and Caron, K.M. (2015). Blood and lymphatic vessel formation. Cold Spring Harbor perspectives in biology *7*, a008268.

Bazzi, Z.A., Lanoue, D., El-Youssef, M., Romagnuolo, R., Tubman, J., Cavallo-Medved, D., Porter, L.A., and Boffa, M.B. (2016). Activated thrombin-activatable fibrinolysis inhibitor (TAFIa) attenuates breast cancer cell metastatic behaviors through inhibition of plasminogen activation and extracellular proteolysis. BMC cancer *16*, 328.

Bortolotti, F., Ruozi, G., Falcione, A., Doimo, S., Dal Ferro, M., Lesizza, P., Zentilin, L., Banks, L., Zacchigna, S., and Giacca, M. (2017). In Vivo Functional Selection Identifies Cardiotrophin-1 as a Cardiac Engraftment Factor for Mesenchymal Stromal Cells. Circulation.

Bos, P.D., Zhang, X.H., Nadal, C., Shu, W., Gomis, R.R., Nguyen, D.X., Minn, A.J., van de Vijver, M.J., Gerald, W.L., Foekens, J.A., *et al.* (2009). Genes that mediate breast cancer metastasis to the brain. Nature *459*, 1005-1009.

Bruick, R.K. (2003). Oxygen sensing in the hypoxic response pathway: regulation of the hypoxia-inducible transcription factor. Genes & development *17*, 2614-2623.

Budczies, J., von Winterfeld, M., Klauschen, F., Bockmayr, M., Lennerz, J.K., Denkert, C., Wolf, T., Warth, A., Dietel, M., Anagnostopoulos, I., *et al.* (2015). The landscape of metastatic progression patterns across major human cancers. Oncotarget *6*, 570-583.

Burnet, F.M. (1970). The concept of immunological surveillance. Progress in experimental tumor research *13*, 1-27.

Calvo, F., Ege, N., Grande-Garcia, A., Hooper, S., Jenkins, R.P., Chaudhry, S.I., Harrington, K., Williamson, P., Moeendarbary, E., Charras, G., *et al.* (2013). Mechanotransduction and YAP-dependent matrix remodelling is required for the generation and maintenance of cancer-associated fibroblasts. Nature cell biology *15*, 637-646.

Cantelmo, A.R., Conradi, L.C., Brajic, A., Goveia, J., Kalucka, J., Pircher, A., Chaturvedi, P., Hol, J., Thienpont, B., Teuwen, L.A., *et al.* (2016). Inhibition of the Glycolytic Activator PFKFB3 in Endothelium Induces Tumor Vessel Normalization, Impairs Metastasis, and Improves Chemotherapy. Cancer cell *30*, 968-985.

Carmeliet, P. (2000). Mechanisms of angiogenesis and arteriogenesis. Nature medicine *6*, 389-395.

Carmeliet, P., and Jain, R.K. (2011a). Molecular mechanisms and clinical applications of angiogenesis. Nature *473*, 298-307.

Carmeliet, P., and Jain, R.K. (2011b). Principles and mechanisms of vessel normalization for cancer and other angiogenic diseases. Nature reviews Drug discovery *10*, 417-427.

Carrer, A., Moimas, S., Zacchigna, S., Pattarini, L., Zentilin, L., Ruozi, G., Mano, M., Sinigaglia, M., Maione, F., Serini, G., *et al.* (2012). Neuropilin-1 identifies a subset of bone marrow Gr1- monocytes that can induce tumor vessel normalization and inhibit tumor growth. Cancer research *72*, 6371-6381.

Cassinelli, G., Lanzi, C., Tortoreto, M., Cominetti, D., Petrangolini, G., Favini, E., Zaffaroni, N., Pisano, C., Penco, S., Vlodavsky, I., *et al.* (2013). Antitumor efficacy of the heparanase inhibitor SST0001 alone and in combination with antiangiogenic agents in the treatment of human pediatric sarcoma models. Biochemical pharmacology *85*, 1424-1432.

Chae, S.S., Kamoun, W.S., Farrar, C.T., Kirkpatrick, N.D., Niemeyer, E., de Graaf, A.M., Sorensen, A.G., Munn, L.L., Jain, R.K., and Fukumura, D. (2010). Angiopoietin-2 interferes with anti-VEGFR2-induced vessel normalization and survival benefit in mice bearing gliomas. Clinical cancer research : an official journal of the American Association for Cancer Research *16*, 3618-3627.

Chaffer, C.L., and Weinberg, R.A. (2011). A perspective on cancer cell metastasis. Science *331*, 1559-1564.

Chen, X., and Song, E. (2019). Turning foes to friends: targeting cancer-associated fibroblasts. Nature reviews Drug discovery *18*, 99-115.

Chiarugi, P., and Giannoni, E. (2008). Anoikis: a necessary death program for anchorage-dependent cells. Biochemical pharmacology *76*, 1352-1364.

Chiavenna, S.M., Jaworski, J.P., and Vendrell, A. (2017). State of the art in anti-cancer mAbs. Journal of biomedical science *24*, 15.

Chouhan, S., Singh, S., Athavale, D., Ramteke, P., Pandey, V., Joseph, J., Mohan, R., Shetty, P.K., and Bhat, M.K. (2016). Glucose induced activation of canonical Wnt signaling pathway in hepatocellular carcinoma is regulated by DKK4. Scientific reports *6*, 27558.

Cohen, J., Blethen, S., Kuntze, J., Smith, S.L., Lomax, K.G., and Mathew, P.M. (2014). Managing the child with severe primary insulin-like growth factor-1 deficiency (IGFD): IGFD diagnosis and management. Drugs in R&D *14*, 25-29.

Colombatti, A., Spessotto, P., Doliana, R., Mongiat, M., Bressan, G.M., and Esposito, G. (2011). The EMILIN/Multimerin family. Frontiers in immunology *2*, 93.

Coxon, F.P., Thompson, K., and Rogers, M.J. (2006). Recent advances in understanding the mechanism of action of bisphosphonates. Current opinion in pharmacology *6*, 307-312.

Crawford, Y., and Ferrara, N. (2009). VEGF inhibition: insights from preclinical and clinical studies. Cell and tissue research *335*, 261-269.

Cui, N., Hu, M., and Khalil, R.A. (2017). Biochemical and Biological Attributes of Matrix Metalloproteinases. Progress in molecular biology and translational science *147*, 1-73.

Dano, K., Behrendt, N., Hoyer-Hansen, G., Johnsen, M., Lund, L.R., Ploug, M., and Romer, J. (2005). Plasminogen activation and cancer. Thrombosis and haemostasis *93*, 676-681.

de Sousa Mesquita, A.P., de Araujo Lopes, S., Pernambuco Filho, P.C.A., Nader, H.B., and Lopes, C.C. (2017). Acquisition of anoikis resistance promotes alterations in the Ras/ERK and PI3K/Akt signaling pathways and matrix remodeling in endothelial cells. Apoptosis : an international journal on programmed cell death.

Diaz-Flores, L., Gutierrez, R., Madrid, J.F., Varela, H., Valladares, F., Acosta, E., Martin-Vasallo, P., and Diaz-Flores, L., Jr. (2009). Pericytes. Morphofunction, interactions and pathology in a quiescent and activated mesenchymal cell niche. Histology and histopathology *24*, 909-969.

Dieterich, L.C., and Detmar, M. (2016). Tumor lymphangiogenesis and new drug development. Advanced drug delivery reviews *99*, 148-160.

Diop-Frimpong, B., Chauhan, V.P., Krane, S., Boucher, Y., and Jain, R.K. (2011). Losartan inhibits collagen I synthesis and improves the distribution and efficacy of nanotherapeutics in tumors. Proceedings of the National Academy of Sciences of the United States of America *108*, 2909-2914.

Dirat, B., Bochet, L., Dabek, M., Daviaud, D., Dauvillier, S., Majed, B., Wang, Y.Y., Meulle, A., Salles, B., Le Gonidec, S., *et al.* (2011). Cancer-associated adipocytes exhibit an activated phenotype and contribute to breast cancer invasion. Cancer research *71*, 2455-2465.

Doliana, R., Bot, S., Bonaldo, P., and Colombatti, A. (2000). EMI, a novel cysteine-rich domain of EMILINs and other extracellular proteins, interacts with the gC1q domains and participates in multimerization. FEBS letters *484*, 164-168.

Dunn, G.P., Old, L.J., and Schreiber, R.D. (2004). The three Es of cancer immunoediting. Annual review of immunology *22*, 329-360.

Dupont, S., Morsut, L., Aragona, M., Enzo, E., Giulitti, S., Cordenonsi, M., Zanconato, F., Le Digabel, J., Forcato, M., Bicciato, S., *et al.* (2011). Role of YAP/TAZ in mechanotransduction. Nature *474*, 179-183.

Eichler, A.F., Chung, E., Kodack, D.P., Loeffler, J.S., Fukumura, D., and Jain, R.K. (2011). The biology of brain metastases-translation to new therapies. Nature reviews Clinical oncology *8*, 344-356.

Fala, L. (2016). Portrazza (Necitumumab), an IgG1 Monoclonal Antibody, FDA Approved for Advanced Squamous Non-Small-Cell Lung Cancer. American health & drug benefits *9*, 119-122.

Fang, J., Xiao, L., Joo, K.I., Liu, Y., Zhang, C., Liu, S., Conti, P.S., Li, Z., and Wang, P. (2016). A potent immunotoxin targeting fibroblast activation protein for treatment of breast cancer in mice. International journal of cancer *138*, 1013-1023.

Fatima, S., Lee, N.P., Tsang, F.H., Kolligs, F.T., Ng, I.O., Poon, R.T., Fan, S.T., and Luk, J.M. (2012). Dickkopf 4 (DKK4) acts on Wnt/beta-catenin pathway by influencing beta-catenin in hepatocellular carcinoma. Oncogene *31*, 4233-4244.

Ferdinand, R., Mitchell, S.A., Batson, S., and Tumur, I. (2012). Treatments for chronic myeloid leukemia: a qualitative systematic review. Journal of blood medicine *3*, 51-76.

Ferrari, G., Cook, B.D., Terushkin, V., Pintucci, G., and Mignatti, P. (2009). Transforming growth factor-beta 1 (TGF-beta1) induces angiogenesis through vascular endothelial growth factor (VEGF)-mediated apoptosis. Journal of cellular physiology *219*, 449-458.

Ferrarini, M., Arsic, N., Recchia, F.A., Zentilin, L., Zacchigna, S., Xu, X., Linke, A., Giacca, M., and Hintze, T.H. (2006). Adeno-associated virus-mediated transduction of VEGF165 improves cardiac tissue viability and functional recovery after permanent coronary occlusion in conscious dogs. Circ Res *98*, 954-961.

Fidler, I.J., and Kripke, M.L. (1977). Metastasis results from preexisting variant cells within a malignant tumor. Science *197*, 893-895.

Folgueras, A.R., Pendas, A.M., Sanchez, L.M., and Lopez-Otin, C. (2004). Matrix metalloproteinases in cancer: from new functions to improved inhibition strategies. The International journal of developmental biology *48*, 411-424.

Franco-Barraza, J., Beacham, D.A., Amatangelo, M.D., and Cukierman, E. (2016). Preparation of Extracellular Matrices Produced by Cultured and Primary Fibroblasts. Current protocols in cell biology *71*, 10 19 11-10 19 34.

Friedl, P., and Wolf, K. (2003). Tumour-cell invasion and migration: diversity and escape mechanisms. Nature reviews Cancer *3*, 362-374.

Friedman, R.M. (2008). Clinical uses of interferons. British journal of clinical pharmacology *65*, 158-162.

Frink, R.E., Peyton, M., Schiller, J.H., Gazdar, A.F., Shay, J.W., and Minna, J.D. (2016). Telomerase inhibitor imetelstat has preclinical activity across the spectrum of non-small cell lung cancer oncogenotypes in a telomere length dependent manner. Oncotarget *7*, 31639-31651.

Froeling, F.E., Feig, C., Chelala, C., Dobson, R., Mein, C.E., Tuveson, D.A., Clevers, H., Hart, I.R., and Kocher, H.M. (2011). Retinoic acid-induced pancreatic stellate cell quiescence reduces paracrine Wnt-beta-catenin signaling to slow tumor progression. Gastroenterology *141*, 1486-1497, 1497 e1481-1414.

Garcia-Caballero, M., Paupert, J., Blacher, S., Van de Velde, M., Quesada, A.R., Medina, M.A., and Noel, A. (2017). Targeting VEGFR-3/-2 signaling pathways with AD0157: a potential strategy against tumor-associated lymphangiogenesis and lymphatic metastases. Journal of hematology & oncology *10*, 122.

Gholamin, S., Mirzaei, H., Razavi, S.M., Hassanian, S.M., Saadatpour, L., Masoudifar, A., ShahidSales, S., and Avan, A. (2017). GD2-targeted immunotherapy and potential value of circulating microRNAs in neuroblastoma. Journal of cellular physiology.

Giacca, M. (2010). Non-redundant functions of the protein isoforms arising from alternative splicing of the VEGF-A pre-mRNA. Transcription *1*, 149-153.

Gialeli, C., Theocharis, A.D., and Karamanos, N.K. (2011). Roles of matrix metalloproteinases in cancer progression and their pharmacological targeting. The FEBS journal *278*, 16-27.

Giannoni, E., Bianchini, F., Calorini, L., and Chiarugi, P. (2011). Cancer associated fibroblasts exploit reactive oxygen species through a proinflammatory signature leading to epithelial mesenchymal transition and stemness. Antioxidants & redox signaling *14*, 2361-2371.

Gioelli, N., Maione, F., Camillo, C., Ghitti, M., Valdembri, D., Morello, N., Darche, M., Zentilin, L., Cagnoni, G., Qiu, Y., *et al.* (2018). A rationally designed NRP1-independent superagonist SEMA3A mutant is an effective anticancer agent. Science translational medicine *10*.

Gocheva, V., Wang, H.W., Gadea, B.B., Shree, T., Hunter, K.E., Garfall, A.L., Berman, T., and Joyce, J.A. (2010). IL-4 induces cathepsin protease activity in tumor-associated macrophages to promote cancer growth and invasion. Genes & development *24*, 241-255.

Gupta, G.P., Nguyen, D.X., Chiang, A.C., Bos, P.D., Kim, J.Y., Nadal, C., Gomis, R.R., Manova-Todorova, K., and Massague, J. (2007). Mediators of vascular remodelling co-opted for sequential steps in lung metastasis. Nature *446*, 765-770.

Halbert, C.L., Allen, J.M., and Miller, A.D. (2001). Adeno-associated virus type 6 (AAV6) vectors mediate efficient transduction of airway epithelial cells in mouse lungs compared to that of AAV2 vectors. Journal of virology *75*, 6615-6624.

Hamzah, J., Jugold, M., Kiessling, F., Rigby, P., Manzur, M., Marti, H.H., Rabie, T., Kaden, S., Grone, H.J., Hammerling, G.J., *et al.* (2008). Vascular normalization in Rgs5-deficient tumours promotes immune destruction. Nature *453*, 410-414.

Heller, A. (2009). The need for monitoring the actual nitric oxide concentration in tumors. Bioanalytical reviews *1*, 3-6.

Hinz, B., Phan, S.H., Thannickal, V.J., Galli, A., Bochaton-Piallat, M.L., and Gabbiani, G. (2007). The myofibroblast: one function, multiple origins. The American journal of pathology *170*, 1807-1816.

Hiratsuka, S., Nakamura, K., Iwai, S., Murakami, M., Itoh, T., Kijima, H., Shipley, J.M., Senior, R.M., and Shibuya, M. (2002). MMP9 induction by vascular endothelial growth factor receptor-1 is involved in lung-specific metastasis. Cancer cell *2*, 289-300.

Hiratsuka, S., Watanabe, A., Aburatani, H., and Maru, Y. (2006). Tumour-mediated upregulation of chemoattractants and recruitment of myeloid cells predetermines lung metastasis. Nature cell biology *8*, 1369-1375.

Holland, S.J., Pan, A., Franci, C., Hu, Y., Chang, B., Li, W., Duan, M., Torneros, A., Yu, J., Heckrodt, T.J., *et al.* (2010). R428, a selective small molecule inhibitor of Axl kinase, blocks tumor spread and prolongs survival in models of metastatic breast cancer. Cancer research *70*, 1544-1554.

Hu, M., Yao, J., Carroll, D.K., Weremowicz, S., Chen, H., Carrasco, D., Richardson, A., Violette, S., Nikolskaya, T., Nikolsky, Y., *et al.* (2008). Regulation of in situ to invasive breast carcinoma transition. Cancer cell *13*, 394-406.

Huber, M.A., Kraut, N., Park, J.E., Schubert, R.D., Rettig, W.J., Peter, R.U., and Garin-Chesa, P. (2003). Fibroblast activation protein: differential expression and serine protease activity in reactive stromal fibroblasts of melanocytic skin tumors. The Journal of investigative dermatology *120*, 182-188.

Jain, R.K. (2001). Normalizing tumor vasculature with anti-angiogenic therapy: a new paradigm for combination therapy. Nature medicine *7*, 987-989.

Jain, R.K., and Carmeliet, P. (2012). SnapShot: Tumor angiogenesis. Cell *149*, 1408-1408 e1401.

Jakobsson, L., Franco, C.A., Bentley, K., Collins, R.T., Ponsioen, B., Aspalter, I.M., Rosewell, I., Busse, M., Thurston, G., Medvinsky, A., *et al.* (2010). Endothelial cells dynamically compete for the tip cell position during angiogenic sprouting. Nature cell biology *12*, 943-953.

Janitz, A.E., Campbell, J.E., Pate, A., Anderson, A., and McNall-Knapp, R. (2016). Racial, Ethnic, and Age Differences in the Incidence and Survival of Childhood Cancer in Oklahoma, 1997-2012. The Journal of the Oklahoma State Medical Association *109*, 355-365.

Jia, H., Bagherzadeh, A., Hartzoulakis, B., Jarvis, A., Lohr, M., Shaikh, S., Aqil, R., Cheng, L., Tickner, M., Esposito, D., *et al.* (2006). Characterization of a bicyclic peptide neuropilin-1 (NP-1) antagonist (EG3287) reveals importance of vascular endothelial growth factor exon 8 for NP-1 binding and role of NP-1 in KDR signaling. The Journal of biological chemistry *281*, 13493-13502.

Joyce, J.A., and Pollard, J.W. (2009). Microenvironmental regulation of metastasis. Nature reviews Cancer *9*, 239-252.

Kalluri, R., and Weinberg, R.A. (2009). The basics of epithelial-mesenchymal transition. The Journal of clinical investigation *119*, 1420-1428.

Kang, Y., Siegel, P.M., Shu, W., Drobnjak, M., Kakonen, S.M., Cordon-Cardo, C., Guise, T.A., and Massague, J. (2003). A multigenic program mediating breast cancer metastasis to bone. Cancer cell *3*, 537-549.

Kaplan, R.N., Riba, R.D., Zacharoulis, S., Bramley, A.H., Vincent, L., Costa, C., MacDonald, D.D., Jin, D.K., Shido, K., Kerns, S.A., *et al.* (2005). VEGFR1-positive haematopoietic bone marrow progenitors initiate the pre-metastatic niche. Nature *438*, 820-827.

Karkkainen, M.J., Haiko, P., Sainio, K., Partanen, J., Taipale, J., Petrova, T.V., Jeltsch, M., Jackson, D.G., Talikka, M., Rauvala, H., *et al.* (2004). Vascular endothelial growth factor C is required for sprouting of the first lymphatic vessels from embryonic veins. Nature immunology *5*, 74-80.

Keeler, A.M., ElMallah, M.K., and Flotte, T.R. (2017). Gene Therapy 2017: Progress and Future Directions. Clinical and translational science *10*, 242-248.

Kerbel, R.S. (2011). Reappraising antiangiogenic therapy for breast cancer. Breast *20 Suppl 3*, S56-60.

Kessenbrock, K., Plaks, V., and Werb, Z. (2010). Matrix metalloproteinases: regulators of the tumor microenvironment. Cell *141*, 52-67.

Khoo, B.L., Warkiani, M.E., Tan, D.S., Bhagat, A.A., Irwin, D., Lau, D.P., Lim, A.S., Lim, K.H., Krisna, S.S., Lim, W.T., *et al.* (2014). Clinical validation of an ultra high-throughput spiral microfluidics for the detection and enrichment of viable circulating tumor cells. PloS one *9*, e99409.

Kintzing, J.R., Filsinger Interrante, M.V., and Cochran, J.R. (2016). Emerging Strategies for Developing Next-Generation Protein Therapeutics for Cancer Treatment. Trends in pharmacological sciences *37*, 993-1008.

Klosowska-Wardega, A., Hasumi, Y., Burmakin, M., Ahgren, A., Stuhr, L., Moen, I., Reed, R.K., Rubin, K., Hellberg, C., and Heldin, C.H. (2009). Combined anti-angiogenic therapy targeting PDGF and VEGF receptors lowers the interstitial fluid pressure in a murine experimental carcinoma. PloS one *4*, e8149.

Klotz, L., Norman, S., Vieira, J.M., Masters, M., Rohling, M., Dube, K.N., Bollini, S., Matsuzaki, F., Carr, C.A., and Riley, P.R. (2015). Cardiac lymphatics are heterogeneous in origin and respond to injury. Nature *522*, 62-67.

Koh, Y.J., Kim, H.Z., Hwang, S.I., Lee, J.E., Oh, N., Jung, K., Kim, M., Kim, K.E., Kim, H., Lim, N.K., *et al.* (2010). Double antiangiogenic protein, DAAP, targeting VEGF-A and angiopoietins in tumor angiogenesis, metastasis, and vascular leakage. Cancer cell *18*, 171-184.

Laklai, H., Miroshnikova, Y.A., Pickup, M.W., Collisson, E.A., Kim, G.E., Barrett, A.S., Hill, R.C., Lakins, J.N., Schlaepfer, D.D., Mouw, J.K., *et al.* (2016). Genotype tunes pancreatic ductal adenocarcinoma tissue tension to induce matricellular fibrosis and tumor progression. Nature medicine *22*, 497-505.

Lecomte, N., Njardarson, J.T., Nagorny, P., Yang, G., Downey, R., Ouerfelli, O., Moore, M.A., and Danishefsky, S.J. (2011). Emergence of potent inhibitors of metastasis in lung cancer via syntheses based on migrastatin. Proceedings of the National Academy of Sciences of the United States of America *108*, 15074-15078.

Lee, J., Ryoo, N.K., Han, H., Hong, H.K., Park, J.Y., Park, S.J., Kim, Y.K., Sim, C., Kim, K., Woo, S.J., *et al.* (2016). Anti-VEGF PolysiRNA Polyplex for the Treatment of Choroidal Neovascularization. Molecular pharmaceutics *13*, 1988-1995.

Leimeister, C., Steidl, C., Schumacher, N., Erhard, S., and Gessler, M. (2002). Developmental expression and biochemical characterization of Emu family members. Developmental biology *249*, 204-218.

Levental, K.R., Yu, H., Kass, L., Lakins, J.N., Egeblad, M., Erler, J.T., Fong, S.F., Csiszar, K., Giaccia, A., Weninger, W., *et al.* (2009). Matrix crosslinking forces tumor progression by enhancing integrin signaling. Cell *139*, 891-906.

Liu, J., Liao, S., Diop-Frimpong, B., Chen, W., Goel, S., Naxerova, K., Ancukiewicz, M., Boucher, Y., Jain, R.K., and Xu, L. (2012). TGF-beta blockade improves the distribution and efficacy of therapeutics in breast carcinoma by normalizing the tumor stroma. Proceedings of the National Academy of Sciences of the United States of America *109*, 16618-16623.

Lu, P., Takai, K., Weaver, V.M., and Werb, Z. (2011). Extracellular matrix degradation and remodeling in development and disease. Cold Spring Harbor perspectives in biology *3*.

Lupinski, R.W. (2009). Aortic fat pad and atrial fibrillation: cardiac lymphatics revisited. ANZ journal of surgery *79*, 70-74.

Lv, Q., Gong, L., Zhang, T., Ye, J., Chai, L., Ni, C., and Mao, Y. (2016). Prognostic value of circulating tumor cells in metastatic breast cancer: a systemic review and meta-analysis. Clinical & translational oncology : official publication of the Federation of Spanish Oncology Societies and of the National Cancer Institute of Mexico *18*, 322-330.

Magness, S.T., Bataller, R., Yang, L., and Brenner, D.A. (2004). A dual reporter gene transgenic mouse demonstrates heterogeneity in hepatic fibrogenic cell populations. Hepatology *40*, 1151-1159.

Man, Y.G. (2010). Tumor cell budding from focally disrupted tumor capsules: a common pathway for all breast cancer subtype derived invasion? Journal of Cancer *1*, 32-37.

Marastoni, S., Andreuzzi, E., Paulitti, A., Colladel, R., Pellicani, R., Todaro, F., Schiavinato, A., Bonaldo, P., Colombatti, A., and Mongiat, M. (2014). EMILIN2 down-modulates the Wnt signalling pathway and suppresses breast cancer cell growth and migration. The Journal of pathology *232*, 391-404.

Marmor, M.D., Skaria, K.B., and Yarden, Y. (2004). Signal transduction and oncogenesis by ErbB/HER receptors. International journal of radiation oncology, biology, physics *58*, 903-913.

Mathur, R., and Weiner, G.J. (2013). Picking the optimal target for antibody-drug conjugates. American Society of Clinical Oncology educational book American Society of Clinical Oncology Meeting.

Mazzone, M., Dettori, D., de Oliveira, R.L., Loges, S., Schmidt, T., Jonckx, B., Tian, Y.M., Lanahan, A.A., Pollard, P., de Almodovar, C.R., *et al.* (2009). Heterozygous deficiency of PHD2 restores tumor oxygenation and inhibits metastasis via endothelial normalization. Cell *136*, 839-851.

McCoy, E.M., Hong, H., Pruitt, H.C., and Feng, X. (2013). IL-11 produced by breast cancer cells augments osteoclastogenesis by sustaining the pool of osteoclast progenitor cells. BMC cancer *13*, 16.

McGinty, L., and Kolesar, J. (2017). Dinutuximab for maintenance therapy in pediatric neuroblastoma. American journal of health-system pharmacy : AJHP : official journal of the American Society of Health-System Pharmacists *74*, 563-567.

Mehta, H.M., Malandra, M., and Corey, S.J. (2015). G-CSF and GM-CSF in Neutropenia. Journal of immunology *195*, 1341-1349.

Messina, S., Mazzeo, A., Bitto, A., Aguennouz, M., Migliorato, A., De Pasquale, M.G., Minutoli, L., Altavilla, D., Zentilin, L., Giacca, M., *et al.* (2007). VEGF overexpression via adeno-associated virus gene transfer promotes skeletal muscle regeneration and enhances muscle function in mdx mice. FASEB journal : official publication of the Federation of American Societies for Experimental Biology *21*, 3737-3746.

Minn, A.J., Gupta, G.P., Siegel, P.M., Bos, P.D., Shu, W., Giri, D.D., Viale, A., Olshen, A.B., Gerald, W.L., and Massague, J. (2005). Genes that mediate breast cancer metastasis to lung. Nature *436*, 518-524.

Modica, T.M.E., Maiorani, O., Sartori, G., Pivetta, E., Doliana, R., Capuano, A., Colombatti, A., and Spessotto, P. (2017). The extracellular matrix protein EMILIN1 silences the RAS-ERK pathway via alpha4beta1 integrin and decreases tumor cell growth. Oncotarget *8*, 27034-27046.

Mouw, J.K., Ou, G., and Weaver, V.M. (2014). Extracellular matrix assembly: a multiscale deconstruction. Nature reviews Molecular cell biology *15*, 771-785.

Nieto, M.A., Huang, R.Y., Jackson, R.A., and Thiery, J.P. (2016). Emt: 2016. Cell *166*, 21-45.

Obenauf, A.C., and Massague, J. (2015). Surviving at a Distance: Organ-Specific Metastasis. Trends in cancer *1*, 76-91.

Ostermann, E., Garin-Chesa, P., Heider, K.H., Kalat, M., Lamche, H., Puri, C., Kerjaschki, D., Rettig, W.J., and Adolf, G.R. (2008). Effective immunoconjugate therapy in cancer models targeting a serine protease of tumor fibroblasts. Clinical cancer research : an official journal of the American Association for Cancer Research *14*, 4584-4592.

Ozdemir, B.C., Pentcheva-Hoang, T., Carstens, J.L., Zheng, X., Wu, C.C., Simpson, T.R., Laklai, H., Sugimoto, H., Kahlert, C., Novitskiy, S.V., *et al.* (2014). Depletion of carcinoma-associated fibroblasts and fibrosis induces immunosuppression and accelerates pancreas cancer with reduced survival. Cancer cell *25*, 719-734.

Paget, G. (1889). Remarks on a Case of Alternate Partial Anaesthesia. British medical journal *1*, 1-3.

Pasaje, C.F., Bae, J.S., Park, B.L., Cheong, H.S., Kim, J.H., Jang, A.S., Uh, S.T., Park, C.S., and Shin, H.D. (2012). Possible role of EMID2 on nasal polyps pathogenesis in Korean asthma patients. BMC medical genetics *13*, 2.

Pietras, K., Pahler, J., Bergers, G., and Hanahan, D. (2008). Functions of paracrine PDGF signaling in the proangiogenic tumor stroma revealed by pharmacological targeting. PLoS medicine *5*, e19.

Pries, A.R., Hopfner, M., le Noble, F., Dewhirst, M.W., and Secomb, T.W. (2010). The shunt problem: control of functional shunting in normal and tumour vasculature. Nature reviews Cancer *10*, 587-593.

Quante, M., Tu, S.P., Tomita, H., Gonda, T., Wang, S.S., Takashi, S., Baik, G.H., Shibata, W., Diprete, B., Betz, K.S., *et al.* (2011). Bone marrow-derived myofibroblasts contribute to the mesenchymal stem cell niche and promote tumor growth. Cancer cell *19*, 257-272.

Rada, J.A., Cornuet, P.K., and Hassell, J.R. (1993). Regulation of corneal collagen fibrillogenesis in vitro by corneal proteoglycan (lumican and decorin) core proteins. Experimental eye research *56*, 635-648.

Rehman, H., Silk, A.W., Kane, M.P., and Kaufman, H.L. (2016). Into the clinic: Talimogene laherparepvec (T-VEC), a first-in-class intratumoral oncolytic viral therapy. Journal for immunotherapy of cancer *4*, 53.

Ricard-Blum, S. (2011). The collagen family. Cold Spring Harbor perspectives in biology *3*, a004978.

Riching, K.M., Cox, B.L., Salick, M.R., Pehlke, C., Riching, A.S., Ponik, S.M., Bass, B.R., Crone, W.C., Jiang, Y., Weaver, A.M., *et al.* (2014). 3D collagen alignment limits protrusions to enhance breast cancer cell persistence. Biophysical journal *107*, 2546-2558.

Roma-Rodrigues, C., Mendes, R., Baptista, P.V., and Fernandes, A.R. (2019). Targeting Tumor Microenvironment for Cancer Therapy. International journal of molecular sciences *20*.

Ruozi, G., Bortolotti, F., Falcione, A., Dal Ferro, M., Ukovich, L., Macedo, A., Zentilin, L., Filigheddu, N., Gortan Cappellari, G., Baldini, G., *et al.* (2015). AAV-mediated in vivo functional selection of tissue-protective factors against ischaemia. Nature communications *6*, 7388.

Safina, A., Vandette, E., and Bakin, A.V. (2007). ALK5 promotes tumor angiogenesis by upregulating matrix metalloproteinase-9 in tumor cells. Oncogene *26*, 2407-2422.

Saif, M.W., Knost, J.A., Chiorean, E.G., Kambhampati, S.R., Yu, D., Pytowski, B., Qin, A., Kauh, J.S., and O'Neil, B.H. (2016). Phase 1 study of the anti-vascular endothelial growth factor receptor 3 monoclonal antibody LY3022856/IMC-3C5 in patients with advanced and refractory solid tumors and advanced colorectal cancer. Cancer chemotherapy and pharmacology *78*, 815-824.

Saintigny, P., Zhang, L., Fan, Y.H., El-Naggar, A.K., Papadimitrakopoulou, V.A., Feng, L., Lee, J.J., Kim, E.S., Ki Hong, W., and Mao, L. (2011). Gene expression profiling predicts the development of oral cancer. Cancer prevention research *4*, 218-229.

Sapadin, A.N., and Fleischmajer, R. (2006). Tetracyclines: nonantibiotic properties and their clinical implications. Journal of the American Academy of Dermatology *54*, 258-265.

Sato, K., Yomogida, K., Wada, T., Yorihuzi, T., Nishimune, Y., Hosokawa, N., and Nagata, K. (2002). Type XXVI collagen, a new member of the collagen family, is specifically expressed in the testis and ovary. The Journal of biological chemistry *277*, 37678-37684.

Satoh, T., Satoh, K., Yaoita, N., Kikuchi, N., Omura, J., Kurosawa, R., Numano, K., Al-Mamun, E., Siddique, M.A., Sunamura, S., *et al.* (2017). Activated TAFI Promotes the Development of Chronic Thromboembolic Pulmonary Hypertension: A Possible Novel Therapeutic Target. Circ Res *120*, 1246-1262.

Schedin, P., and Keely, P.J. (2011). Mammary gland ECM remodeling, stiffness, and mechanosignaling in normal development and tumor progression. Cold Spring Harbor perspectives in biology *3*, a003228.

Schutte, B.C., Mitros, J.P., Bartlett, J.A., Walters, J.D., Jia, H.P., Welsh, M.J., Casavant, T.L., and McCray, P.B., Jr. (2002). Discovery of five conserved beta -defensin gene clusters using a computational search strategy. Proceedings of the National Academy of Sciences of the United States of America *99*, 2129-2133.

Scott, A.M., Wiseman, G., Welt, S., Adjei, A., Lee, F.T., Hopkins, W., Divgi, C.R., Hanson, L.H., Mitchell, P., Gansen, D.N., *et al.* (2003). A Phase I dose-escalation study of sibrotuzumab in patients with advanced or metastatic fibroblast activation protein-positive cancer. Clinical cancer research : an official journal of the American Association for Cancer Research *9*, 1639-1647.

Sethi, N., Dai, X., Winter, C.G., and Kang, Y. (2011). Tumor-derived JAGGED1 promotes osteolytic bone metastasis of breast cancer by engaging notch signaling in bone cells. Cancer cell *19*, 192-205.

Sherman, M.H., Yu, R.T., Engle, D.D., Ding, N., Atkins, A.R., Tiriac, H., Collisson, E.A., Connor, F., Van Dyke, T., Kozlov, S., *et al.* (2014). Vitamin D receptor-mediated stromal reprogramming suppresses pancreatitis and enhances pancreatic cancer therapy. Cell *159*, 80-93.

Siegel, R.L., Miller, K.D., and Jemal, A. (2019). Cancer statistics, 2019. CA: a cancer journal for clinicians *69*, 7-34.

Steeg, P.S. (2006). Tumor metastasis: mechanistic insights and clinical challenges. Nature medicine *12*, 895-904.

Sternlicht, M.D., and Werb, Z. (2001). How matrix metalloproteinases regulate cell behavior. Annual review of cell and developmental biology *17*, 463-516.

Stoeltzing, O., Ahmad, S.A., Liu, W., McCarty, M.F., Wey, J.S., Parikh, A.A., Fan, F., Reinmuth, N., Kawaguchi, M., Bucana, C.D., *et al.* (2003). Angiopoietin-1 inhibits vascular permeability, angiogenesis, and growth of hepatic colon cancer tumors. Cancer research *63*, 3370-3377.

Su, S., Chen, J., Yao, H., Liu, J., Yu, S., Lao, L., Wang, M., Luo, M., Xing, Y., Chen, F., *et al.* (2018). CD10(+)GPR77(+) Cancer-Associated Fibroblasts Promote Cancer Formation and Chemoresistance by Sustaining Cancer Stemness. Cell *172*, 841-856 e816.

Sugawara, M., Miyoshi, H., Miura, T., Tanaka, H., Tsubota, K.I., and Liu, H. (2016). Dynamics of Actin Stress Fibers and Focal Adhesions during Slow Migration in Swiss 3T3 Fibroblasts: Intracellular Mechanism of Cell Turning. BioMed research international *2016*, 5749749.

Swift, M.R., and Weinstein, B.M. (2009). Arterial-venous specification during development. Circ Res *104*, 576-588.

Thiery, J.P. (2009). [Epithelial-mesenchymal transitions in cancer onset and progression]. Bulletin de l'Academie nationale de medecine *193*, 1969-1978; discussion 1978-1969.

Tilbury, K.B., Campbell, K.R., Eliceiri, K.W., Salih, S.M., Patankar, M., and Campagnola, P.J. (2017). Stromal alterations in ovarian cancers via wavelength dependent Second Harmonic Generation microscopy and optical scattering. BMC cancer *17*, 102.

Tsujino, T., Seshimo, I., Yamamoto, H., Ngan, C.Y., Ezumi, K., Takemasa, I., Ikeda, M., Sekimoto, M., Matsuura, N., and Monden, M. (2007). Stromal myofibroblasts predict disease recurrence for colorectal cancer. Clinical cancer research : an official journal of the American Association for Cancer Research *13*, 2082-2090.

Uhler, C., and Shivashankar, G.V. (2017). Regulation of genome organization and gene expression by nuclear mechanotransduction. Nature reviews Molecular cell biology *18*, 717-727.

Valastyan, S., and Weinberg, R.A. (2011). Tumor metastasis: molecular insights and evolving paradigms. Cell *147*, 275-292.

Vandekeere, S., Dewerchin, M., and Carmeliet, P. (2015). Angiogenesis Revisited: An Overlooked Role of Endothelial Cell Metabolism in Vessel Sprouting. Microcirculation *22*, 509-517.

Vosseler, S., Mirancea, N., Bohlen, P., Mueller, M.M., and Fusenig, N.E. (2005). Angiogenesis inhibition by vascular endothelial growth factor receptor-2 blockade reduces stromal matrix metalloproteinase expression, normalizes stromal tissue, and reverts epithelial tumor phenotype in surface heterotransplants. Cancer research *65*, 1294-1305.

Walker, C., Mojares, E., and Del Rio Hernandez, A. (2018). Role of Extracellular Matrix in Development and Cancer Progression. International journal of molecular sciences *19*.

Walsh, G. (2014). Biopharmaceutical benchmarks 2014. Nature biotechnology *32*, 992-1000.

Warkiani, M.E., Guan, G., Luan, K.B., Lee, W.C., Bhagat, A.A., Chaudhuri, P.K., Tan, D.S., Lim, W.T., Lee, S.C., Chen, P.C., *et al.* (2014). Slanted spiral microfluidics for the ultra-fast, label-free isolation of circulating tumor cells. Lab on a chip *14*, 128-137.

Weilbaecher, K.N., Guise, T.A., and McCauley, L.K. (2011). Cancer to bone: a fatal attraction. Nature reviews Cancer *11*, 411-425.

Weissmueller, S., Manchado, E., Saborowski, M., Morris, J.P.t., Wagenblast, E., Davis, C.A., Moon, S.H., Pfister, N.T., Tschaharganeh, D.F., Kitzing, T., *et al.* (2014). Mutant p53 drives pancreatic cancer metastasis through cell-autonomous PDGF receptor beta signaling. Cell *157*, 382-394.

Wigle, J.T., Harvey, N., Detmar, M., Lagutina, I., Grosveld, G., Gunn, M.D., Jackson, D.G., and Oliver, G. (2002). An essential role for Prox1 in the induction of the lymphatic endothelial cell phenotype. The EMBO journal *21*, 1505-1513.

Winkler, F., Kozin, S.V., Tong, R.T., Chae, S.S., Booth, M.F., Garkavtsev, I., Xu, L., Hicklin, D.J., Fukumura, D., di Tomaso, E., *et al.* (2004). Kinetics of vascular normalization by VEGFR2 blockade governs brain tumor response to radiation: role of oxygenation, angiopoietin-1, and matrix metalloproteinases. Cancer cell *6*, 553-563.

Winter, J., Kraus, D., Reckenbeil, J., and Probstmeier, R. (2016). Oncogenic relevant defensins: expression pattern and proliferation characteristics of human tumor cell lines. Tumour biology : the journal of the International Society for Oncodevelopmental Biology and Medicine *37*, 7959-7966.

Xiao, Q., and Ge, G. (2012). Lysyl oxidase, extracellular matrix remodeling and cancer metastasis. Cancer microenvironment : official journal of the International Cancer Microenvironment Society *5*, 261-273.

Xiao, X., Xiao, W., Li, J., and Samulski, R.J. (1997). A novel 165-base-pair terminal repeat sequence is the sole cis requirement for the adeno-associated virus life cycle. Journal of virology *71*, 941-948.

Yan, Y.L., Miller, M.T., Cao, Y., and Cohen, S.M. (2009). Synthesis of hydroxypyrone- and hydroxythiopyrone-based matrix metalloproteinase inhibitors: developing a structure-activity relationship. Bioorganic & medicinal chemistry letters *19*, 1970-1976.

Yang, L., and Moses, H.L. (2008). Transforming growth factor beta: tumor suppressor or promoter? Are host immune cells the answer? Cancer research *68*, 9107-9111.

Yang, S., Zhang, J.J., and Huang, X.Y. (2012). Mouse models for tumor metastasis. Methods in molecular biology *928*, 221-228.

Yang, Z.F., and Poon, R.T. (2008). Vascular changes in hepatocellular carcinoma. Anatomical record *291*, 721-734.

Ye, J., Wu, D., Wu, P., Chen, Z., and Huang, J. (2014). The cancer stem cell niche: cross talk between cancer stem cells and their microenvironment. Tumour biology : the journal of the International Society for Oncodevelopmental Biology and Medicine *35*, 3945-3951.

Zacchigna, L., Vecchione, C., Notte, A., Cordenonsi, M., Dupont, S., Maretto, S., Cifelli, G., Ferrari, A., Maffei, A., Fabbro, C., *et al.* (2006). Emilin1 links TGF-beta maturation to blood pressure homeostasis. Cell *124*, 929-942.

Zacchigna, S., Pattarini, L., Zentilin, L., Moimas, S., Carrer, A., Sinigaglia, M., Arsic, N., Tafuro, S., Sinagra, G., and Giacca, M. (2008). Bone marrow cells recruited through the neuropilin-1 receptor promote arterial formation at the sites of adult neoangiogenesis in mice. The Journal of clinical investigation *118*, 2062-2075.

Zacchigna, S., Zentilin, L., and Giacca, M. (2014). Adeno-associated virus vectors as therapeutic and investigational tools in the cardiovascular system. Circ Res *114*, 1827-1846.

Zaman, M.H., Trapani, L.M., Sieminski, A.L., Mackellar, D., Gong, H., Kamm, R.D., Wells, A., Lauffenburger, D.A., and Matsudaira, P. (2006). Migration of tumor cells in 3D matrices is governed by matrix stiffness along with cell-matrix adhesion and proteolysis. Proceedings of the National Academy of Sciences of the United States of America *103*, 10889-10894.

Zhang, H., Yang, B., Mu, X., Ahmed, S.S., Su, Q., He, R., Wang, H., Mueller, C., Sena-Esteves, M., Brown, R., *et al.* (2011). Several rAAV vectors efficiently cross the blood-brain barrier and transduce neurons and astrocytes in the neonatal mouse central nervous system. Molecular therapy : the journal of the American Society of Gene Therapy *19*, 1440-1448.

Zhou, W., Fong, M.Y., Min, Y., Somlo, G., Liu, L., Palomares, M.R., Yu, Y., Chow, A., O'Connor, S.T., Chin, A.R., *et al.* (2014). Cancer-secreted miR-105 destroys vascular endothelial barriers to promote metastasis. Cancer cell *25*, 501-515.

WEBSITE REFERENCES

World Health Organization, *https://www.who.int*

Cetuximab, *https://www.accessdata.fda.gov/drugsatfda_docs/label/2012/125084s0228lbl.pdf*

Panitumumab, *https://www.accessdata.fda.gov/drugsatfda_docs/label/2009/125147s080lbl.pdf*

Trastuzumab, *https://www.accessdata.fda.gov/drugsatfda_docs/label/2010/103792s5250lbl.pdf*

Pertuzumab, *https://www.accessdata.fda.gov/drugsatfda_docs/label/2013/125409s051lbl.pdf*

Dinutuximab, *https://www.accessdata.fda.gov/drugsatfda_docs/label/2015/125516s000lbl.pdf*

Olaratumab, *https://www.accessdata.fda.gov/drugsatfda_docs/label/2016/761038lbl.pdf*

Bevacizumab, *https://www.accessdata.fda.gov/drugsatfda_docs/label/2009/125085s0169lbl.pdf*

Ramucirumab, *https://www.accessdata.fda.gov/drugsatfda_docs/label/2014/125477lbl.pdf*

Ipilimumab, *https://www.accessdata.fda.gov/drugsatfda_docs/label/2015/125377s073lbl.pdf*

Nivolumab, *https://www.accessdata.fda.gov/drugsatfda_docs/label/2014/125554lbl.pdf*

Pembrolizumab, *https://www.accessdata.fda.gov/drugsatfda_docs/label/2016/125514s012lbl.pdf*

Atezolizumab, *https://www.accessdata.fda.gov/drugsatfda_docs/label/2016/761034s000lbl.pdf*

Denosumab, *https://www.accessdata.fda.gov/drugsatfda_docs/label/2010/125320s0000lbl.pdf*

Ado-trastuzumab emtansine *https://www.accessdata.fda.gov/drugsatfda_docs/label/2013/125427lbl.pdf*

6. APPENDIX

Ranking of the screened secreted factors.

Ranking position	AAV9-Pool	Factor	LOG	SEM	N
1	1	Pth	2,04	0,17	3
2	12	Fgf3	1,62	0,09	4
3	19	Galnt2	1,05	0,11	4
4	1	Emid2	0,87	0,09	3
5	22	Lgals3	0,80	0,13	3
6	2	Lalba	0,78	0,17	4
7	1	Retnlb	0,73	0,11	3
8	18	Nyx	0,60	0,02	4
9	20	Lifr	0,56	0,04	6
10	8	Lcn12	0,52	0,03	4
11	23	Fbln2	0,52	0,30	4
12	23	Dhh	0,49	0,37	5
13	22	Crhbp	0,48	0,13	3
14	23	Tnfrsf11b	0,48	0,31	5
15	1	Lcn6	0,47	0,01	3
16	13	Sfrp4	0,46	0,07	4
17	1	Retnla	0,46	0,25	3
18	15	Serpini1	0,46	0,12	3
19	22	Bglap2	0,44	0,03	3
20	23	Bmp8b	0,43	0,37	5
21	17	Fbln5	0,42	0,49	5
22	1	Abpg	0,40	0,37	3
23	12	Pla2g2f	0,40	0,03	4
24	23	Fst	0,39	0,39	5
25	1	Spink6	0,39	0,02	3
26	13	Prss8	0,38	0,04	4
27	12	Cd70	0,37	0,12	4
28	13	Clec11a	0,37	0,10	4
29	19	Lao1	0,37	0,72	4
30	23	Thbs1	0,36	0,36	5
31	13	Prss27	0,36	0,80	4
32	1	1100001G20Rik	0,36	0,03	3
33	21	Emilin2	0,36	0,10	6
34	12	4921521F21Rik	0,36	0,09	4
35	23	Apol8	0,35	0,28	5
36	12	Car6	0,34	0,05	4
37	5	Igfbp6	0,33	0,05	6
38	22	Il21	0,32	0,02	3
39	15	Gfod1	0,31	0,15	3
40	22	Art5	0,31	0,21	3
41	13	4921521F21Rik	0,30	0,19	4

42	15	Serpina1f	0,30	0,14	4
43	1	Figf	0,29	0,17	3
44	1	Tff3	0,28	0,04	3
45	12	Il33	0,28	0,46	4
46	7	Defb19	0,28	0,20	3
47	17	Bmp3	0,28	0,06	5
48	13	Frzb	0,27	0,05	4
49	1	Igfbp1	0,27	0,51	3
50	15	Cx3cl1	0,27	0,14	4
51	5	Fibin	0,27	0,03	6
52	1	Defb29	0,27	0,22	3
53	5	Dkk4	0,26	0,04	6
54	22	Tpbpb	0,26	0,02	3
55	1	Wfdc15a	0,26	0,24	3
56	2	Lgals2	0,26	0,20	4
57	13	Apoh	0,25	0,05	4
58	15	Serpine2	0,25	0,19	4
59	22	Nenf	0,25	0,14	3
60	12	Nxph1	0,25	0,13	4
61	23	Col19a1	0,24	0,22	4
62	20	Col10a1	0,24	0,05	6
63	7	Gast	0,24	0,21	3
64	23	Bmp1	0,23	0,30	5
65	23	Scube1	0,23	0,39	5
66	23	Adamts2	0,23	0,30	5
67	1	Mif	0,22	0,21	3
68	6	Prl7c1	0,22	0,13	3
69	1	Mgp	0,22	0,13	3
70	7	Defcr4	0,21	0,15	3
71	5	Tfpi	0,21	0,06	6
72	5	Tfpi2	0,21	0,05	6
73	4	Fgf7	0,21	0,05	3
74	15	Serpina1e	0,21	0,11	4
75	1	Ins1	0,21	0,07	3
76	22	Lyg1	0,21	0,05	3
77	21	Emilin1	0,20	0,04	6
78	19	Gpc6	0,20	0,17	4
79	5	Prl3d1	0,20	0,03	6
80	15	Serpina5	0,19	0,21	4
81	12	Npvf	0,19	0,06	4
82	7	Gip	0,19	0,13	3
83	5	Gpx6	0,19	0,02	6
84	12	Prss28	0,19	0,73	4
85	22	Lcn10	0,19	0,10	3
86	14	Wnt16	0,19	0,05	5
87	4	Tnfrsf19	0,19	0,03	3
88	1	Apoc3	0,18	0,02	3
89	19	Ecm1	0,18	0,04	4

90	6	Mfap4	0,18	0,10	3
91	17	Rya3	0,18	0,08	5
92	12	Cthrc1	0,18	0,18	4
93	10	Rarres1	0,17	0,07	6
94	23	Egf	0,17	0,17	4
95	17	Cpa5	0,17	0,08	5
96	17	Emid1	0,17	0,02	5
97	11	Obp1a	0,16	0,02	6
98	15	Lipf	0,16	0,05	4
99	1	Abpa	0,16	0,10	3
100	2	Kap	0,16	0,18	4
101	5	Psp	0,16	0,03	6
102	10	Spp1	0,16	0,08	6
103	7	1110017I16Rik	0,16	0,10	3
104	20	Pros1	0,16	0,02	6
105	19	Gpc5	0,16	0,03	4
106	13	Spon2	0,15	0,11	4
107	4	Spt1	0,15	0,08	3
108	17	Lpl	0,15	0,07	5
109	21	Egflam	0,15	0,12	6
110	19	Il16	0,15	0,12	4
111	12	Prss34	0,15	0,20	3
112	12	Fgf20	0,15	0,10	4
113	19	Pglyrp2	0,15	0,15	4
114	13	4930486L24Rik	0,15	0,08	4
115	8	Fgf9	0,15	0,03	4
116	12	Clec3a	0,14	0,14	4
117	21	Thbs3	0,14	0,04	6
118	22	Defb36	0,14	0,03	3
119	14	Tgfb1	0,14	0,02	5
120	22	8030411F24Rik	0,14	0,05	3
121	13	Chrdl1	0,14	0,06	4
122	20	1300017J02Rik	0,14	0,03	6
123	20	Lrriq3	0,14	0,04	6
124	6	C1qa	0,14	0,22	3
125	22	Cbln3	0,14	0,06	3
126	18	Bpil2	0,14	0,09	4
127	6	Ntf3	0,14	0,16	3
128	7	Spinlw1	0,14	0,27	3
129	13	AI182371	0,14	0,09	4
130	4	Timp3	0,14	0,07	3
131	11	Crh	0,13	0,09	6
132	8	Mup3	0,13	0,02	4
133	19	Lgi3	0,13	0,11	4
134	22	Lcn11	0,13	0,03	3
135	6	Klk1	0,13	0,15	3
136	5	Prl8a9	0,13	0,06	6
137	23	Wnt4	0,13	0,29	5

138	22	Saa1	0,13	0,03	3
139	17	Mmp13	0,13	0,17	5
140	15	Lox	0,12	0,07	4
141	1	Clps	0,12	0,16	3
142	15	Chi3l4	0,12	0,08	4
143	12	Egfl7	0,12	0,10	4
144	7	Fam24a	0,12	0,22	3
145	12	Wfdc1	0,12	0,11	4
146	12	Lgals8	0,12	0,20	4
147	22	Prdx6	0,12	0,07	3
148	7	Defb11	0,12	0,08	3
149	4	Spp2	0,12	0,02	3
150	19	Adamts17	0,12	0,07	4
151	5	Prl8a6	0,11	0,01	6
152	4	Scg5	0,11	0,02	3
153	14	Wnt2	0,11	0,03	5
154	9	BC048599	0,11	0,03	6
155	5	Timp2	0,11	0,01	6
156	2	Fam19a2	0,11	0,12	4
157	13	Prss38	0,11	0,32	4
158	21	Eln	0,10	0,07	6
159	10	Aagab	0,10	0,05	6
160	5	Prl2b1	0,10	0,04	6
161	18	Adpgk	0,10	0,06	4
162	20	Pamr1	0,10	0,02	6
163	20	Masp1	0,10	0,04	6
164	10	Metrnl	0,10	0,04	6
165	2	Ctla2a	0,10	0,13	4
166	20	Hgf	0,10	0,01	6
167	1	AI462493	0,10	0,03	3
168	20	Arsj	0,09	0,05	6
169	5	Crisp3	0,09	0,03	6
170	13	Epyc	0,09	0,20	4
171	10	Fcnb	0,09	0,05	6
172	11	Lcn3	0,09	0,03	6
173	14	Wnt6	0,09	0,05	5
174	20	Alb1	0,09	0,04	6
175	1	Abpb	0,09	0,17	3
176	4	Oosp1	0,09	0,03	3
177	17	Cpxm1	0,09	0,10	5
178	15	Bmp8a	0,09	0,07	4
179	10	Klk5	0,09	0,03	6
180	21	C6	0,09	0,03	6
181	1	Ccdc126	0,09	0,12	3
182	10	Dhrs13	0,09	0,02	6
183	10	Dhrs7	0,09	0,07	6
184	18	Gdf5	0,09	0,04	4
185	8	Cfc1	0,09	0,04	4

186	15	Pgc	0,09	0,18	3
187	4	Krtap13	0,09	0,10	3
188	2	Mdk	0,09	0,09	4
189	23	Chia	0,09	0,69	4
190	17	Serpina10	0,09	0,04	5
191	7	Defb2	0,08	0,24	3
192	12	Ifna11	0,08	0,11	4
193	19	Gpc2	0,08	0,05	4
194	10	Dnase1	0,08	0,03	6
195	18	Pcyox1l	0,08	0,12	4
196	8	Ifna12	0,08	0,01	4
197	4	Eppb9	0,08	0,04	3
198	5	Prl8a8	0,08	0,03	6
199	19	Grn	0,08	0,07	4
200	22	Fshb	0,08	0,08	3
201	15	Serpini2	0,08	0,06	4
202	11	Spint4	0,08	0,10	6
203	5	Fam3a	0,08	0,02	6
204	19	C9	0,07	0,09	4
205	22	Tnfsf4	0,07	0,01	3
206	15	4921510H08Rik	0,07	0,09	4
207	21	Lepr	0,07	0,04	6
208	8	1700016D06Rik	0,07	0,05	4
209	9	Trh	0,07	0,04	6
210	22	Lhb	0,07	0,03	3
211	13	Lgals9	0,07	0,10	4
212	18	Lbp	0,07	0,12	4
213	19	Gp2	0,07	0,04	4
214	4	Ctf1	0,07	0,10	3
215	8	Pspn	0,07	0,03	4
216	4	Orm1	0,07	0,03	3
217	18	Papln	0,07	0,08	4
218	18	Pla2g3	0,07	0,07	4
219	5	Ebi3	0,07	0,08	6
220	15	Ccbe1	0,07	0,08	4
221	5	Rspo4	0,07	0,03	6
222	20	Klkb1	0,07	0,02	6
223	5	Ccdc134	0,07	0,05	6
224	10	Ogn	0,06	0,07	6
225	20	Hhip	0,06	0,06	6
226	8	A930018P22Rik	0,06	0,02	4
227	22	Cort	0,06	0,03	3
228	14	Sphk1	0,06	0,03	5
229	4	Pdgfa	0,06	0,02	3
230	21	Olfml2b	0,06	0,03	6
231	11	Wfdc3	0,06	0,04	6
232	8	Nbl1	0,06	0,04	4
233	4	Pla2g12b	0,06	0,03	3

234	19	Wfikkn1	0,06	0,05	4
235	14	Lefty2	0,06	0,05	5
236	14	Hapln1	0,06	0,02	5
237	22	Prl2a1	0,06	0,06	3
238	14	Wnt7b	0,06	0,03	5
239	20	Podn	0,06	0,05	6
240	7	Npff	0,06	0,41	3
241	8	Gpihbp1	0,06	0,03	4
242	18	Amy1	0,06	0,08	4
243	5	Mbl1	0,06	0,02	6
244	8	Sbp	0,06	0,03	4
245	20	Trf	0,06	0,04	6
246	17	Hyal1	0,06	0,08	5
247	21	Qsox1	0,05	0,09	6
248	10	Apol9b	0,05	0,02	6
249	21	Matn2	0,05	0,03	6
250	10	Azgp1	0,05	0,04	6
251	8	Gh	0,05	0,04	4
252	13	Inhbe	0,05	0,52	4
253	8	Edn2	0,05	0,02	4
254	6	Pdgfd	0,05	0,13	3
255	5	Olfml1	0,05	0,04	6
256	17	U46068	0,05	0,11	5
257	17	Pla1a	0,05	0,04	5
258	10	Tnfsf13b	0,05	0,04	6
259	9	Prdx4	0,05	0,05	6
260	12	Cer1	0,05	0,10	4
261	14	9030224M15	0,05	0,04	5
262	4	Rnase10	0,05	0,08	3
263	9	Klk10	0,05	0,02	6
264	21	Itih3	0,05	0,02	6
265	9	Il4ra	0,05	0,01	6
266	21	Sema3a	0,05	0,05	6
267	13	Angptl7	0,05	0,13	4
268	6	Crisp1	0,05	0,23	3
269	8	Ifna5	0,04	0,02	4
270	5	Afm	0,04	0,01	6
271	8	Dand5	0,04	0,01	4
272	9	Fasl	0,04	0,02	6
273	18	Pm20d1	0,04	0,09	4
274	22	Rarres2	0,04	0,03	3
275	6	Klk8	0,04	0,10	3
276	11	Defcr-rs2	0,04	0,04	6
277	11	Defb10	0,04	0,05	6
278	11	Ifnb1	0,04	0,04	6
279	20	Matn4	0,04	0,05	6
280	8	Timp4	0,04	0,04	4
281	22	Rspo1	0,04	0,06	3

282	9	Colec11	0,04	0,02	6
283	4	Sostdc1	0,04	0,03	3
284	14	Tesp1	0,04	0,01	5
285	21	Comp	0,04	0,01	6
286	5	Gpx3	0,04	0,03	6
287	18	Crispld2	0,04	0,13	4
288	23	Adamts18	0,04	0,65	4
289	22	Apol6	0,04	0,19	3
290	4	Il12a	0,04	0,04	3
291	4	Il18bp	0,04	0,04	3
292	17	Pnliprp1	0,04	0,08	5
293	21	Spon1	0,04	0,03	6
294	9	Klk14	0,04	0,02	6
295	8	Sva	0,04	0,01	4
296	8	Lcn8	0,04	0,01	4
297	18	Dmp1	0,04	0,09	4
298	18	Myoc	0,04	0,05	4
299	9	Tnfaip6	0,03	0,04	6
300	8	Rnase9	0,03	0,02	4
301	9	Rnaset2a	0,03	0,03	6
302	9	Egfl8	0,03	0,04	6
303	18	Epor	0,03	0,05	4
304	4	Il18	0,03	0,02	3
305	22	Scrg1	0,03	0,08	3
306	17	Srpx2	0,03	0,05	5
307	14	Wnt8a	0,03	0,03	5
308	5	Fam3c	0,03	0,03	6
309	7	Defcr-rs10	0,03	0,09	3
310	13	Fcna	0,03	0,09	4
311	4	Gkn2	0,03	0,03	3
312	21	Adamtsl2	0,03	0,08	6
313	8	Lep	0,03	0,01	4
314	21	Adamts16	0,03	0,02	6
315	18	Vtn	0,03	0,09	4
316	14	Thpo	0,03	0,08	5
317	14	Serpinb5	0,03	0,04	5
318	10	Kazald1	0,03	0,05	6
319	20	Ache	0,03	0,04	6
320	9	Pomc	0,03	0,08	6
321	1	Wfdc12	0,03	0,33	3
322	17	Serpinc1	0,03	0,04	5
323	5	Prl4a1	0,03	0,03	6
324	14	Pglyrp4	0,03	0,04	5
325	9	4930473A06Rik	0,03	0,02	6
326	10	C1qtnf1	0,03	0,03	6
327	14	Cyr61	0,03	0,06	5
328	9	1700066M21Rik	0,03	0,03	6
329	18	Fkrp	0,02	0,06	4

330	9	Prss33	0,02	0,04	6
331	8	Apcs	0,02	0,02	4
332	4	Dpt	0,02	0,12	3
333	21	Cp	0,02	0,14	6
334	9	Mcpt7	0,02	0,03	6
335	22	Chchd5	0,02	0,05	3
336	21	Cpxm2	0,02	0,03	6
337	19	Egfl6	0,02	0,08	4
338	14	Sftpd	0,02	0,10	5
339	21	Gsn	0,02	0,02	6
340	15	Serpina1a	0,02	0,11	4
341	9	Plunc	0,02	0,03	6
342	8	Lyzl1	0,02	0,03	4
343	21	Furin	0,02	0,03	6
344	23	Itih5	0,02	0,38	5
345	9	Nxph2	0,02	0,03	6
346	9	BC049730	0,02	0,03	6
347	11	Defb30	0,02	0,04	6
348	14	Chad	0,02	0,05	5
349	4	Mmrn1	0,02	0,05	3
350	1	Pon3	0,02	0,18	3
351	2	Tpbpa	0,02	0,29	4
352	21	St14	0,02	0,03	6
353	4	Ntf5	0,02	0,08	3
354	14	Chi3l1	0,02	0,02	5
355	11	Pdap1	0,02	0,05	6
356	14	Apol7c	0,02	0,03	5
357	4	Edn1	0,02	0,03	3
358	13	Cfhr1	0,01	0,26	4
359	18	Itgbl1	0,01	0,02	4
360	11	Btc	0,01	0,05	6
361	11	Pate4	0,01	0,07	6
362	8	Reg3g	0,01	0,03	4
363	17	Scg3	0,01	0,05	5
364	11	Svs6	0,01	0,06	6
365	21	Cfb	0,01	0,01	6
366	15	Lipk	0,01	0,03	4
367	4	Rbp4	0,01	0,02	3
368	10	Nudt22	0,01	0,05	6
369	11	Prok1	0,01	0,04	6
370	13	C1qtnf9	0,01	0,18	4
371	14	Svs2	0,01	0,03	5
372	20	Rnpep	0,01	0,07	6
373	17	Mmp8	0,01	0,05	5
374	11	Msmb	0,01	0,07	6
375	21	Morc2a	0,01	0,03	6
376	11	EG654465	0,01	0,13	6
377	14	Wnt9b	0,01	0,02	5

378	18	Serpind1	0,01	0,12	4
379	5	Il34	0,01	0,01	6
380	9	Igfbpl1	0,01	0,03	6
381	6	Prl7a1	0,01	0,07	3
382	10	Fam92a	0,01	0,03	6
383	9	1810065E05Rik	0,01	0,03	6
384	13	Wnt8b	0,01	0,12	4
385	10	2410001C21Rik	0,01	0,08	6
386	9	Tpsb2	0,01	0,02	6
387	21	Man2b2	0,00	0,14	5
388	9	Il22ra2	0,00	0,06	6
389	21	Ephb6	0,00	0,12	6
390	8	4930549C01Rik	0,00	0,04	4
391	19	Psapl1	0,00	0,11	4
392	9	Pi15	0,00	0,01	6
393	11	Uts2d	0,00	0,08	6
394	9	Colec10	0,00	0,06	6
395	17	Gc	0,00	0,01	5
396	14	Wnt1	0,00	0,04	5
397	8	Il13	0,00	0,02	4
398	8	Csn3	0,00	0,03	4
399	5	1810030J14Rik	0,00	0,01	6
400	14	Hapln3	0,00	0,03	5
401	9	Cma1	0,00	0,03	6
402	11	Defcr-rs1	0,00	0,05	6
403	14	Fam131a	0,00	0,03	5
404	14	Tsku	0,00	0,05	5
405	9	Sbpl	0,00	0,03	6
406	21	Heg1	0,00	0,06	6
407	21	Adamts4	0,00	0,03	6
408	18	F10	0,00	0,08	4
409	18	E030002O03Rik	0,00	0,03	4
410	21	C2	0,00	0,05	6
411	14	Gdf1	0,00	0,04	5
412	10	Lgals12	0,00	0,11	6
413	14	Apoa5	-0,01	0,04	5
414	22	Ifne	-0,01	0,10	3
415	9	Mbl2	-0,01	0,02	6
416	14	Wnt5a	-0,01	0,06	5
417	11	Defb25	-0,01	0,06	6
418	17	Smoc2	-0,01	0,02	5
419	17	Angptl3	-0,01	0,03	5
420	11	Defb42	-0,01	0,03	6
421	11	Sval2	-0,01	0,05	6
422	22	Rln3	-0,01	0,06	3
423	14	Wif1	-0,01	0,05	5
424	20	Ntn4	-0,01	0,08	6
425	21	Postn	-0,01	0,02	6

426	10	Acrbp	-0,01	0,04	6
427	5	Vwc2l	-0,01	0,01	6
428	8	Fgf10	-0,01	0,05	4
429	21	Prss12	-0,01	0,03	6
430	9	Gzma	-0,01	0,03	6
431	4	Vegfb	-0,01	0,06	3
432	17	Srpx	-0,01	0,06	5
433	21	Fstl5	-0,01	0,02	6
434	1	Guca2a	-0,01	0,12	3
435	22	Lgals7	-0,01	0,04	3
436	8	Iltifb	-0,01	0,02	4
437	14	Pdgfrl	-0,01	0,04	5
438	21	Pcsk1	-0,01	0,03	6
439	10	Cgref1	-0,01	0,04	6
440	19	A130022J15Rik	-0,01	0,10	4
441	4	Pla2g12a	-0,01	0,03	3
442	18	Angpt4	-0,01	0,02	4
443	19	6130401L20Rik	-0,01	0,10	4
444	9	Prl	-0,01	0,04	6
445	20	C1ra	-0,01	0,02	6
446	9	Fstl3	-0,01	0,05	6
447	17	Proc	-0,01	0,01	5
448	9	2310021H06Rik	-0,02	0,03	6
449	10	Fam108a	-0,02	0,02	6
450	10	1700040L02Rik	-0,02	0,06	6
451	21	BC046331	-0,02	0,05	6
452	10	Sfrp5	-0,02	0,03	6
453	17	Fuca2	-0,02	0,04	5
454	8	Tha1	-0,02	0,04	4
455	11	Pla2g1b	-0,02	0,10	6
456	8	Ly6k	-0,02	0,03	4
457	4	C8g	-0,02	0,04	3
458	8	Adm2	-0,02	0,02	4
459	11	Spink12	-0,02	0,10	6
460	19	C8a	-0,02	0,06	4
461	8	Ifna7	-0,02	0,02	4
462	14	Gdf3	-0,02	0,08	5
463	21	Nell2	-0,02	0,06	6
464	5	Fgf8	-0,02	0,01	6
465	9	Pcsk1n	-0,02	0,03	6
466	9	Kitl	-0,02	0,02	6
467	21	Loxl3	-0,02	0,03	6
468	5	Prl7d1	-0,02	0,01	6
469	22	Prtn3	-0,02	0,08	3
470	11	Gm94	-0,02	0,10	6
471	7	Cst13	-0,02	0,15	3
472	11	Bola3	-0,02	0,06	6
473	5	Fam3b	-0,02	0,02	6

474	20	Pcsk2	-0,02	0,03	6
475	1	Guca2b	-0,02	0,09	3
476	12	Prl2c3	-0,02	0,08	4
477	9	Prl8a2	-0,02	0,02	6
478	8	Fgf21	-0,02	0,05	4
479	18	Matn3	-0,02	0,06	4
480	17	Gdf10	-0,02	0,02	5
481	1	D730039F16Rik	-0,02	0,06	3
482	4	Lyg2	-0,02	0,12	3
483	18	Dmkn	-0,02	0,08	4
484	9	Crisp2	-0,02	0,03	6
485	11	Tff1	-0,02	0,05	6
486	15	Serpina1c	-0,02	0,12	4
487	4	Il28b	-0,02	0,07	3
488	21	Sema3f	-0,02	0,02	6
489	22	Defa3	-0,03	0,05	3
490	20	Vit	-0,03	0,04	6
491	10	Gm1019	-0,03	0,03	6
492	22	Spink4	-0,03	0,06	3
493	21	Dpp4	-0,03	0,04	6
494	23	Ace	-0,03	0,14	3
495	10	BC107230	-0,03	0,09	6
496	12	Ifnab	-0,03	0,20	4
497	12	Csf3	-0,03	0,15	4
498	5	Dkkl1	-0,03	0,02	6
499	21	Svs1	-0,03	0,02	6
500	12	1190003M12Rik	-0,03	0,06	4
501	20	Afp	-0,03	0,02	6
502	20	Mmp9	-0,03	0,02	6
503	4	Apom	-0,03	0,05	3
504	20	Hgfac	-0,03	0,05	6
505	9	Dkk1	-0,03	0,03	6
506	12	Mcpt8	-0,03	0,09	4
507	4	Vegfa	-0,03	0,09	3
508	14	Cxadr	-0,03	0,04	5
509	20	Col9a2	-0,04	0,09	6
510	8	Plac1l	-0,04	0,01	4
511	5	Prl3a1	-0,04	0,02	6
512	17	Clu	-0,04	0,14	5
513	20	F11	-0,04	0,05	6
514	22	Defb7	-0,04	0,03	3
515	8	Prg3	-0,04	0,04	4
516	5	Csn2	-0,04	0,02	6
517	12	Apod	-0,04	0,13	4
518	21	Dag1	-0,04	0,04	6
519	21	Plg	-0,04	0,02	6
520	21	Sema3c	-0,04	0,07	6
521	1	Pyy	-0,04	0,15	3

522	11	Reg3a	-0,04	0,11	6
523	5	Twsg1	-0,04	0,03	6
524	4	Hmgb1	-0,04	0,06	3
525	22	Fgf18	-0,04	0,04	3
526	9	Prl8a1	-0,04	0,05	6
527	15	Prss35	-0,04	0,08	3
528	14	Pon1	-0,04	0,04	5
529	9	Mcpt1	-0,04	0,05	6
530	1	S100a13	-0,04	0,26	3
531	12	Epo	-0,04	0,09	4
532	1	Txn1	-0,04	0,07	3
533	14	Wnt3	-0,04	0,06	5
534	4	Lta	-0,04	0,02	3
535	22	Clec3b	-0,04	0,05	3
536	13	Anxa1	-0,04	0,06	4
537	14	Wisp1	-0,04	0,04	5
538	9	Fgfbp3	-0,05	0,06	6
539	15	Serpina12	-0,05	0,16	4
540	18	Angptl1	-0,05	0,08	4
541	15	Serpine1	-0,05	0,14	4
542	4	Gpx7	-0,05	0,06	3
543	18	Hhipl2	-0,05	0,03	4
544	14	Lefty1	-0,05	0,05	5
545	15	Chid1	-0,05	0,20	4
546	5	5730469M10Rik	-0,05	0,04	6
547	4	Sdf2	-0,05	0,01	3
548	19	Gpc4	-0,05	0,10	4
549	19	Mmp21	-0,05	0,17	4
550	17	Mmp28	-0,05	0,03	5
551	20	Mmp2	-0,05	0,04	6
552	18	Lipc	-0,05	0,05	4
553	18	Vwde	-0,05	0,03	4
554	11	Ly96	-0,05	0,06	6
555	8	Lyzl6	-0,05	0,03	4
556	18	Ifnar2	-0,05	0,10	4
557	10	Gdf15	-0,05	0,06	6
558	21	Itih1	-0,05	0,05	6
559	21	Adamts15	-0,05	0,13	6
560	20	Ltf	-0,05	0,01	6
561	18	Pnliprp2	-0,05	0,07	4
562	5	Oit1	-0,05	0,02	6
563	19	Vwa2	-0,05	0,09	4
564	9	6030468B19Rik	-0,06	0,03	6
565	13	Pglyrp3	-0,06	0,12	4
566	14	Fam166b	-0,06	0,11	5
567	14	Mstn	-0,06	0,04	5
568	22	Ppy	-0,06	0,06	3
569	11	Camp	-0,06	0,06	6

570	21	Hhipl1	-0,06	0,03	6
571	14	Col9a3	-0,06	0,02	5
572	18	1700008I05Rik	-0,06	0,07	4
573	10	Nodal	-0,06	0,06	6
574	20	Ghr	-0,06	0,06	6
575	1	Ghrh	-0,06	1,11	3
576	17	Fjx1	-0,06	0,08	5
577	4	Ctf2	-0,06	0,02	3
578	14	Bgn	-0,06	0,07	5
579	17	Scpep1	-0,06	0,03	5
580	18	Il17rb	-0,06	0,06	3
581	20	Col9a1	-0,06	0,06	6
582	20	Loxl1	-0,06	0,04	6
583	14	Fmod	-0,07	0,08	5
584	8	Ucn3	-0,07	0,02	4
585	18	Edil3	-0,07	0,03	4
586	12	Ifna13	-0,07	0,10	4
587	5	Prl2c2	-0,07	0,02	6
588	22	1600012H06Rik	-0,07	0,08	3
589	10	Prss22	-0,07	0,03	6
590	8	Sval1	-0,07	0,02	4
591	10	Igfbp3	-0,07	0,08	6
592	22	Ifna6	-0,07	0,02	3
593	4	Mia1	-0,07	0,09	3
594	22	Defb15	-0,07	0,03	3
595	20	Pcsk9	-0,07	0,04	6
596	1	Apoa2	-0,07	0,02	3
597	12	Tnfsf11	-0,07	0,10	4
598	10	C1ql2	-0,07	0,07	6
599	22	Ang2	-0,07	0,07	3
600	15	Gm1006	-0,07	0,06	4
601	22	Rspo3	-0,07	0,12	3
602	8	OTTMUSG00000007655	-0,07	0,03	4
603	11	Retnlg	-0,08	0,02	6
604	4	Gkn1	-0,08	0,06	3
605	9	Ccdc3	-0,08	0,05	6
606	8	Manf	-0,08	0,01	4
607	8	Timp1	-0,08	0,02	4
608	23	Nhlrc3	-0,08	0,39	5
609	17	C1rl	-0,08	0,05	5
610	11	Gphb5	-0,08	0,09	6
611	9	Penk	-0,08	0,05	6
612	14	Crlf2	-0,08	0,06	5
613	17	Efemp2	-0,08	0,03	5
614	10	Hyls1	-0,08	0,05	6
615	9	Klk4	-0,08	0,03	6
616	8	Edn3	-0,08	0,04	4
617	19	Coch	-0,08	0,05	4

618	1	Expi	-0,08	0,10	3
619	11	Prok2	-0,08	0,11	6
620	10	Lgi4	-0,08	0,03	6
621	4	Sectm1b	-0,09	0,13	3
622	19	Mmp19	-0,09	0,02	4
623	8	Armetl1	-0,09	0,02	4
624	10	6330406I15Rik	-0,09	0,06	6
625	10	Apol9a	-0,09	0,12	6
626	18	Mmp3	-0,09	0,07	4
627	9	Cfd	-0,09	0,06	6
628	19	Es1	-0,09	0,05	4
629	8	Fgf4	-0,09	0,03	4
630	14	Aspn	-0,09	0,06	5
631	21	Lepre1	-0,09	0,10	6
632	18	Mmp11	-0,09	0,09	4
633	13	Lect1	-0,09	0,06	4
634	18	Cfh	-0,09	0,03	4
635	8	Gpx5	-0,09	0,05	4
636	6	Tnfsf15	-0,09	0,04	3
637	14	Nov	-0,10	0,11	5
638	11	Defb38	-0,10	0,06	6
639	8	Lcn4	-0,10	0,07	4
640	11	Defa6	-0,10	0,06	6
641	10	Csn1s1	-0,10	0,16	6
642	19	Mmp17	-0,10	0,12	4
643	17	C4bp	-0,10	0,44	5
644	4	Orm2	-0,10	0,03	3
645	20	Msln	-0,10	0,34	6
646	15	Fetub	-0,10	0,07	4
647	22	Tnfrsf22	-0,10	0,01	3
648	5	Glipr1l1	-0,10	0,02	6
649	21	Vwa5a	-0,10	0,03	6
650	4	Nrtn	-0,10	0,06	3
651	7	Scgb3a2	-0,10	0,49	3
652	9	Klk15	-0,10	0,04	6
653	18	Crispld1	-0,10	0,11	4
654	4	Grem1	-0,10	0,07	3
655	10	Cd40	-0,11	0,09	6
656	17	Pgcp	-0,11	0,02	5
657	4	Il23a	-0,11	0,06	3
658	8	Sftpc	-0,11	0,04	4
659	4	Cbln4	-0,11	0,11	3
660	15	Chi3l3	-0,11	0,12	4
661	11	Ifna4	-0,11	0,05	6
662	14	Rccd1	-0,11	0,08	5
663	11	Ifnz	-0,11	0,05	6
664	10	Gnptg	-0,11	0,08	6
665	11	Oxt	-0,11	0,10	6

666	5	Vstm2a	-0,11	0,06	6
667	11	EG328354	-0,11	0,12	6
668	15	Hapln4	-0,11	0,10	4
669	17	Mmp1a	-0,11	0,05	5
670	14	Il1rap	-0,12	0,12	5
671	2	Gal	-0,12	0,44	4
672	21	Ace2	-0,12	0,04	6
673	10	Fgl1	-0,12	0,04	6
674	19	Gpc3	-0,12	0,15	4
675	13	Bat4	-0,12	0,15	4
676	11	Hcrt	-0,12	0,06	6
677	22	Defb8	-0,12	0,09	3
678	22	Cbln1	-0,12	0,05	3
679	8	Lyz1	-0,12	0,03	4
680	15	Gfod2	-0,12	0,12	4
681	1	Iapp	-0,12	0,07	3
682	15	Bmp15	-0,12	0,06	4
683	15	Pla2g15	-0,12	0,19	4
684	12	Tnf	-0,12	0,12	4
685	11	Wfdc13	-0,12	0,05	6
686	4	Insl6	-0,13	0,13	3
687	19	Npnt	-0,13	0,19	4
688	20	Sparcl1	-0,13	0,14	6
689	4	Amtn	-0,13	0,07	3
690	5	Anxa2	-0,13	0,03	6
691	5	4933406J08Rik	-0,13	0,05	6
692	13	Wnt7a	-0,13	0,48	4
693	5	Prl5a1	-0,13	0,02	6
694	18	Angpt1	-0,13	0,12	4
695	20	Cntn4	-0,13	0,02	6
696	1	Nxph3	-0,13	0,09	3
697	11	Tac1	-0,13	0,03	6
698	20	Adamts1	-0,13	0,07	6
699	4	Sost	-0,13	0,04	3
700	20	Flt1	-0,14	0,06	6
701	1	Apoc1	-0,14	0,42	3
702	8	Wfdc2	-0,14	0,02	4
703	17	Ihh	-0,14	0,13	5
704	10	Hsd17b11	-0,14	0,08	6
705	11	Ifng	-0,14	0,05	6
706	19	Aoah	-0,14	0,08	4
707	21	Bcan	-0,14	0,09	6
708	18	Fam20a	-0,14	0,14	4
709	2	Rnase1	-0,14	0,45	4
710	22	Klk12	-0,14	0,08	3
711	5	Prl3b1	-0,14	0,02	6
712	7	Cst8	-0,14	0,16	3
713	12	Ifna14	-0,14	0,03	4

714	12	Fgf23	-0,15	0,72	4
715	22	Mup5	-0,15	0,04	3
716	11	Ucn	-0,15	0,08	6
717	13	Car11	-0,15	0,10	4
718	20	Aggf1	-0,15	0,35	6
719	18	Matn1	-0,15	0,08	4
720	7	Smr2	-0,15	0,21	3
721	14	Prelp	-0,15	0,09	5
722	19	Habp2	-0,16	0,12	4
723	17	Chga	-0,16	0,06	5
724	18	Htra1	-0,16	0,10	4
725	6	C1qtnf3	-0,16	0,12	3
726	13	Ambp	-0,16	0,10	4
727	5	Fgf15	-0,16	0,03	6
728	7	Cga	-0,17	0,16	3
729	4	Esm1	-0,17	0,08	3
730	6	Klk1b9	-0,17	0,00	3
731	14	Sepp1	-0,17	0,06	5
732	23	Sema3b	-0,17	0,32	5
733	22	Ghrl	-0,18	0,03	3
734	1	B2m	-0,18	0,06	3
735	23	Htra3	-0,18	0,31	5
736	20	F12	-0,18	0,07	6
737	14	Ptx3	-0,18	0,07	5
738	12	Mmp7	-0,18	0,17	4
739	5	Folr4	-0,19	0,05	6
740	15	Fam20b	-0,19	0,13	4
741	19	Scg2	-0,19	0,16	4
742	4	Ifnk	-0,19	0,05	3
743	23	Bmp4	-0,20	0,36	5
744	13	Cd5l	-0,20	0,11	4
745	18	Nptxr	-0,20	0,08	4
746	19	Fga	-0,20	0,78	4
747	15	Efemp1	-0,20	0,03	4
748	23	Loxl4	-0,20	0,36	5
749	14	Wnt9a	-0,21	0,10	5
750	10	Stc2	-0,21	0,14	6
751	6	Dkk2	-0,21	0,10	3
752	5	Crp	-0,21	0,02	6
753	12	Ngfb	-0,21	0,16	4
754	19	Csf1	-0,22	0,06	4
755	5	Adamtsl4	-0,22	0,03	6
756	15	Eda	-0,22	0,15	4
757	5	Amelx	-0,22	0,02	6
758	12	Tnfsf8	-0,22	0,20	4
759	13	Inhbc	-0,22	0,18	4
760	2	Ptgds	-0,23	0,31	4
761	7	Slpi	-0,23	0,26	3

762	20	Cfi	-0,23	0,35	6
763	10	Fam132a	-0,23	0,11	6
764	15	Angptl4	-0,24	0,09	4
765	6	C1qb	-0,24	0,10	3
766	15	Crtap	-0,24	0,28	4
767	23	Sfrp4	-0,24	0,35	5
768	7	Nppc	-0,25	0,18	3
769	2	Npc2	-0,26	0,48	4
770	20	F2	-0,26	0,35	6
771	19	Podnl1	-0,26	0,15	4
772	22	Adm	-0,26	0,05	3
773	13	Creld2	-0,26	0,27	4
774	2	Lgals1	-0,26	0,39	4
775	11	Cst7	-0,26	0,25	6
776	11	Rln1	-0,27	0,29	6
777	7	Pip	-0,27	0,38	3
778	19	Fam55d	-0,27	0,09	4
779	1	Apoc2	-0,28	0,09	3
780	17	Angptl6	-0,28	0,31	5
781	6	Adipoq	-0,28	0,81	3
782	23	BC053749	-0,28	0,38	5
783	12	Klk1b3	-0,28	0,27	4
784	18	Fgb	-0,28	0,15	4
785	6	Bdnf	-0,28	0,12	3
786	17	Cfp	-0,29	0,44	5
787	12	Fam178b	-0,29	0,53	4
788	23	Aoc2	-0,29	0,37	5
789	1	Bola2	-0,29	0,40	3
790	15	Mmp23	-0,29	0,24	4
791	23	Olfml2a	-0,29	0,45	5
792	7	Apbh	-0,30	0,14	3
793	5	Il27	-0,30	0,02	6
794	18	Acpl2	-0,31	0,16	4
795	7	Tslp	-0,31	0,18	3
796	1	Plac9	-0,32	1,06	3
797	17	Olfm3	-0,32	0,48	5
798	23	Nell1	-0,32	0,31	5
799	15	Fam46c	-0,32	0,12	4
800	19	Wfikkn2	-0,32	0,31	4
801	23	Vwa5b2	-0,32	0,33	5
802	23	Serpina6	-0,33	0,29	5
803	6	Cnpy4	-0,33	0,10	3
804	23	5430419D17Rik	-0,33	0,31	5
805	20	Vwce	-0,33	0,33	6
806	17	Bpil1	-0,33	0,35	5
807	23	Adamtsl5	-0,33	0,27	5
808	15	Hyal3	-0,33	0,17	4
809	23	Adamts8	-0,34	0,34	5

810	2	Saa3	-0,34	0,48	4
811	7	Tac2	-0,34	0,32	3
812	23	Wnt5b	-0,34	0,36	5
813	20	Zp1	-0,34	0,35	6
814	6	Klk1b5	-0,35	0,62	3
815	20	Mmp25	-0,35	0,21	6
816	6	Klk1b8	-0,35	0,09	3
817	13	Ahsg	-0,35	0,16	4
818	13	Il12b	-0,35	0,09	4
819	18	Lipg	-0,35	0,45	4
820	1	Retn	-0,35	0,04	3
821	7	Spink8	-0,35	0,33	3
822	7	Abpz	-0,35	0,10	3
823	17	Mmp10	-0,36	0,40	5
824	6	Klk1b1	-0,36	0,88	3
825	7	Defb9	-0,36	0,31	3
826	23	Umod	-0,36	0,33	5
827	12	Il1b	-0,36	0,47	4
828	17	Il9r	-0,36	0,40	5
829	12	Pnoc	-0,37	0,44	4
830	2	Pla2g2e	-0,37	0,34	4
831	17	Tinagl1	-0,38	0,56	5
832	13	Vwc2	-0,38	0,12	4
833	2	1810020D17Rik	-0,38	0,39	4
834	6	Wisp2	-0,38	0,70	3
835	10	C1qtnf2	-0,39	0,06	6
836	2	Nmb	-0,39	0,56	4
837	2	Grp	-0,40	0,47	4
838	7	Fshb	-0,40	0,35	3
839	7	Sct	-0,41	0,09	3
840	20	Glb1l	-0,41	0,34	6
841	12	Prl3c1	-0,41	0,66	4
842	7	Cst11	-0,41	0,15	3
843	1	Wfdc9	-0,42	1,04	3
844	20	Il17re	-0,42	0,34	6
845	13	Ctgf	-0,42	0,73	4
846	23	Amy2a5	-0,42	0,36	5
847	17	Oc90	-0,43	0,50	5
848	6	Gm106	-0,43	0,19	3
849	2	Qrfp	-0,45	0,56	4
850	1	Sst	-0,45	1,18	3
851	2	D16H22S680E	-0,45	0,46	4
852	22	Ela2	-0,45	0,24	3
853	7	Igf1	-0,46	0,04	3
854	23	C330005M16Rik	-0,46	0,35	5
855	12	Tnfsf10	-0,46	0,42	4
856	19	Rai2	-0,47	0,45	4
857	20	Mmp16	-0,47	0,35	6

858	13	Mfap3	-0,47	0,39	4
859	7	Tac4	-0,47	0,11	3
860	20	5430413K10Rik	-0,48	0,35	6
861	23	Pnlip	-0,48	0,34	5
862	17	Ntn5	-0,48	0,35	5
863	7	Nppb	-0,49	0,29	3
864	23	Lcat	-0,49	0,35	5
865	10	Fstl1	-0,49	0,52	6
866	19	Plat	-0,49	0,80	4
867	23	Cpa3	-0,50	0,36	5
868	20	Zp2	-0,51	0,35	6
869	1	Enho	-0,51	0,28	3
870	19	Lad1	-0,51	0,45	4
871	7	Gm14461	-0,51	0,11	3
872	13	2610109H07Rik	-0,51	0,59	4
873	23	Cpa2	-0,52	0,39	5
874	6	Svs3b	-0,52	0,10	3
875	7	1700040I03Rik	-0,52	0,14	3
876	7	Tff2	-0,52	0,48	3
877	13	Luzp2	-0,52	0,57	4
878	7	Calcb	-0,52	0,45	3
879	12	Ggh	-0,53	0,74	4
880	7	Uts2	-0,53	0,22	3
881	2	Csn1s2b	-0,53	0,41	4
882	9	Igfbp5	-0,54	0,06	6
883	23	Abhd15	-0,55	0,39	5
884	2	Fam19a5	-0,55	0,49	4
885	1	Scgb1a1	-0,55	0,93	3
886	10	Ghr	-0,56	0,51	6
887	21	AK053037	-0,56	0,07	6
888	11	Tshb	-0,56	0,04	6
889	2	Saa4	-0,57	0,41	4
890	2	Lyzl4	-0,57	0,47	4
891	17	Hpx	-0,57	0,51	5
892	19	Arsk	-0,58	0,70	4
893	10	Apoe	-0,58	0,52	6
894	23	Fbln1	-0,58	0,35	5
895	12	Prl3d2	-0,58	0,38	4
896	13	Pdgfc	-0,58	0,54	4
897	17	Mmp12	-0,58	0,53	5
898	12	Prl7b1	-0,58	0,47	4
899	2	3200002M19Rik	-0,59	0,45	4
900	11	Fgf22	-0,59	0,50	6
901	18	Bpi	-0,59	0,87	4
902	7	Svs5	-0,60	1,03	3
903	2	Gpha2	-0,60	0,54	4
904	2	Fam19a3	-0,61	0,45	4
905	13	Wnt3a	-0,61	0,99	4

906	6	Sod3	-0,61	0,23	3
907	2	Pla2g10	-0,61	0,49	4
908	10	Sfrp1	-0,61	0,53	6
909	10	Igfbp2	-0,61	0,52	6
910	17	Adamdec1	-0,62	0,64	5
911	21	Spink5	-0,62	0,14	6
912	1	Defb1	-0,62	0,76	3
913	7	Wfdc15b	-0,63	0,43	3
914	17	Bmp5	-0,63	0,55	5
915	17	Smpdl3b	-0,63	0,34	5
916	1	Npy	-0,64	0,79	3
917	2	Pla2g2c	-0,64	0,34	4
918	19	Gpc1	-0,64	0,14	4
919	18	Angpt2	-0,65	0,76	4
920	12	Cd40lg	-0,65	0,72	4
921	1	Hamp	-0,67	0,50	3
922	6	2310044H10Rik	-0,68	0,68	3
923	19	Psap	-0,68	0,76	4
924	2	Wfdc6a	-0,68	0,44	4
925	18	Spint1	-0,69	0,78	4
926	23	Adamts19	-0,70	0,86	4
927	2	Metrn	-0,71	0,52	4
928	19	2210023G05Rik	-0,72	0,74	4
929	7	Slurp1	-0,72	0,67	3
930	7	Npb	-0,73	0,68	3
931	2	Ndp	-0,74	0,56	4
932	13	Car15	-0,75	0,79	4
933	6	Fgfbp1	-0,75	0,97	3
934	1	Apln	-0,75	0,75	3
935	12	Fgf17	-0,75	0,63	4
936	2	Smr3a	-0,75	0,59	4
937	19	A930038C07Rik	-0,76	0,75	4
938	2	Cartpt	-0,77	0,51	4
939	15	Loxl2	-0,77	0,82	4
940	6	Klk6	-0,78	0,40	3
941	6	Apoa1	-0,78	0,57	3
942	2	Il15ra	-0,79	0,55	4
943	18	Serpinf2	-0,79	0,79	4
944	19	Lgi1	-0,81	0,73	4
945	10	Prss29	-0,81	0,48	6
946	6	Ceacam10	-0,81	0,68	3
947	6	Rtbdn	-0,81	1,31	3
948	6	C1ql3	-0,81	0,67	3
949	19	Ces8	-0,82	0,79	4
950	2	Fam178b	-0,83	0,47	4
951	12	Gdnf	-0,84	0,67	4
952	2	Bola1	-0,84	0,57	4
953	11	Il10	-0,84	0,57	6

954	13	Capg	-0,84	0,73	4
955	12	Sparc	-0,85	0,57	4
956	2	Saa2	-0,85	0,51	4
957	23	Tnr	-0,85	0,77	5
958	7	Defb6	-0,85	0,75	3
959	2	Cst3	-0,85	0,39	4
960	12	Il6	-0,85	0,74	4
961	15	Olfml3	-0,86	1,07	3
962	6	Klk1b21	-0,88	1,06	3
963	2	Cck	-0,88	0,52	4
964	6	Dhrs11	-0,89	0,95	3
965	15	Tgfb3	-0,91	1,12	4
966	2	Pla2g5	-0,91	0,52	4
967	12	Il1a	-0,92	0,67	4
968	6	Optc	-0,92	1,06	3
969	23	Crlf1	-0,93	0,69	5
970	1	AI413582	-0,93	0,75	3
971	15	Apoa4	-0,93	0,92	4
972	7	Cst9	-0,94	0,58	3
973	13	Ibsp	-0,94	1,07	4
974	6	Egfbp2	-0,95	1,18	3
975	6	C1qtnf6	-0,97	1,04	3
976	15	Il13ra2	-0,97	1,10	4
977	2	Calca	-0,98	0,47	4
978	2	Prap1	-0,98	0,53	4
979	13	Kera	-0,99	0,85	4
980	2	Wfdc5	-1,01	0,53	4
981	7	Pla2g2d	-1,02	1,41	3
982	6	C1qc	-1,04	0,79	3
983	7	Dppa1	-1,04	0,70	3
984	2	Prss40	-1,05	0,77	4
985	15	Wnt2b	-1,05	0,76	4
986	6	Rnaset2b	-1,07	0,78	3
987	2	Ang4	-1,07	0,67	4
988	15	Cpa4	-1,10	0,91	4
989	19	Ces5	-1,10	0,69	4
990	13	Lum	-1,11	0,87	4
991	13	Il1rl1	-1,11	0,81	4
992	15	Ren1	-1,12	0,59	4
993	6	Stc1	-1,13	1,06	3
994	13	Hp	-1,13	0,78	4
995	7	Defb14	-1,15	1,08	3
996	2	Fam19a4	-1,17	0,51	4
997	15	Bmp2	-1,17	1,06	3
998	7	Dspp	-1,18	1,39	3
999	7	Spink2	-1,21	1,60	3
1000	2	Agrp	-1,22	0,57	4
1001	19	C8b	-1,26	0,94	4

1002	7	Defb3	-1,27	1,39	3
1003	7	Cst12	-1,27	1,23	3
1004	6	Klk1b16	-1,28	0,96	3
1005	6	Prl7a2	-1,28	0,96	3
1006	7	9230104L09Rik	-1,29	1,45	3
1007	6	Klk11	-1,30	1,32	3
1008	7	Insl3	-1,30	1,44	3
1009	2	Insl5	-1,32	0,89	4
1010	6	Igfbp4	-1,32	1,06	3
1011	22	Fgf5	-1,36	1,18	3
1012	12	Tnfsf12	-1,38	0,85	4
1013	6	Klk7	-1,38	1,12	3
1014	2	Ttr	-1,39	0,63	4
1015	12	1700016G05Rik	-1,40	0,66	4
1016	13	Hapln2	-1,41	0,76	4
1017	6	Fam20c	-1,45	1,24	3
1018	18	Pltp	-1,46	0,92	4
1019	19	Ntn3	-1,51	0,84	4
1020	13	Fam132b	-1,52	0,83	4
1021	23	Thbs2	-1,54	0,66	4
1022	6	Pdyn	-1,54	1,41	3
1023	13	Gm128	-1,56	0,97	4
1024	15	AU021092	-1,57	1,17	4
1025	15	B4galt1	-1,59	1,06	4
1026	13	Prss42	-1,65	0,68	4
1027	15	Tuft1	-1,70	0,97	4
1028	15	4921515J06Rik	-1,96	0,92	3
1029	11	EG654453	-2,07	0,13	6